Unsteady Axisymmetric Flow by the Method of Discrete Vortices

by

Bernardo de Bernardinis

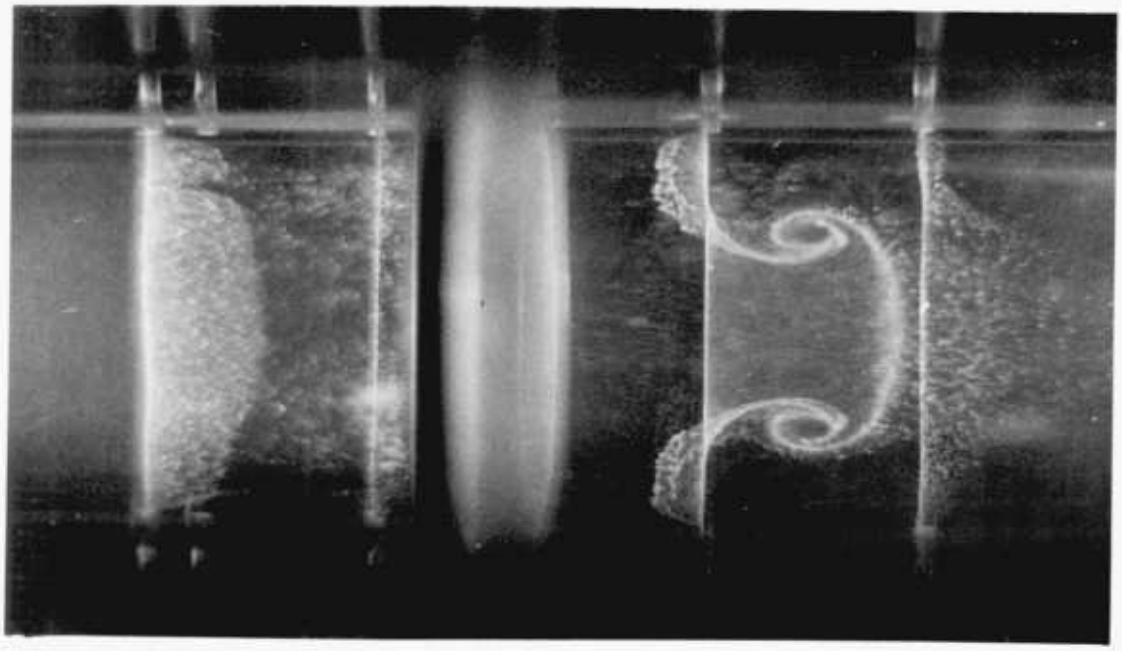

A thesis submitted to the University of London
for the degree of Doctor of Philosophy
in the Faculty of Engineering, 1980

Physiological Flow Studies Unit
Department of Aeronautics
Imperial College
London, SW7

ABSTRACT

The method of discrete vortices is extended to the calculation of unsteady, axisymmetric separated flows at high Reynolds number. Theoretically, the problem is divided into three parts: calculation of the potential flow using bound vortex rings to model the boundary surfaces; analysis of separation from a sharp edge; and the evolution of the resultant free shear layer modelled by a sequence of discrete vortex rings.

The calculation procedure is developed from the theoretical analysis. It is used to calculate both external and internal flows. The cases of impulsively started and oscillatory flow around a disc are investigated. Oscillatory and pulsatile flow through flat plate and stepped orifices in a pipe are also calculated. The calculated results are compared with experiments. The calculations predict very well the gross features of the flows such as the instantaneous pressure drop through an orifice or the unsteady drag on an impulsively started disc. The flow patterns and particularly the distribution of the primary vorticity are also described accurately.

ACKNOWLEDGEMENTS

I am grateful to many colleagues at Imperial College and the Faculty of Engineering of Genoa University who helped me in this project. I am particularly indebted to Dr. M. J. H. Graham and Dr. K. H. Parker for their guidance, encouragement, and constructive criticism leading up to this thesis. Thanks are due to Professor C. G. Caro, Director of the Physiological Flow Studies Unit, and to Professor E. Marchi, Director of the Hydraulic Institute of Genoa University, for allowing my visit to Imperial College and supporting me during this long period. I am also indebted to Professor D. W. Moore of the Mathematics Department at Imperial College for ideas and constructive discussions. I would like to thank Miss M. Evans for converting my handwriting into a neatly typed thesis and Mr. J. O'Leary who produced the photographs.

Lastly, I would like to thank all those who, understanding my Italian temperament, provided a friendly environment around me.

-oOo-

CONTENTS

-oOo-

1. INTRODUCTION

In the present work we are concerned with the calculation of axisymmetric, unsteady, separated flows either past sharp-edged bluff bodies or through sharp-edged orifices at moderately high Reynolds number.

When a viscous fluid is accelerated past a stationary object the motion which starts from rest is initially irrotational and separated. As the instantaneous Reynolds number increases the flow may separate forming a wake which is dominated by large, essentially inviscid, vortex patterns. The flow field can be divided into large regions of inviscid flow and small regions of viscous dominated flow. The problem in such a flow is to match an inner boundary-layer solution with an outer potential flow solution.

If sharp edges are present, where the separation is expected to occur, and the Reynolds number is moderate, but sufficiently high, the viscosity may increase the thickness of the boundary layers, slightly modifying the outer potential flow, but it has little or no effect on the separation and on the large vortex structure of the wake. This suggested to several authors that the flow past sharp-edged bodies may be calculated by combining well-known methods to calculate the external potential flow about arbitrary bodies and a discrete-vortex model to represent the shear layers shed from fixed separation points on the surface of the body. It is this method which will be developed, used and evaluated in this thesis.

A common reason for flow separation is the presence in the boundaries of regions of high curvature relative to the local boundary layer thickness. In these regions the flow is unable to negotiate the curve and the boundary layers on either side of the separation point flow outwards and coalesce. A free shear layer of thickness comparable to that of the boundary layers forms and, in the case of a flow starting from rest, assumes under the influence of its own velocity, the form of a spiral vortex which exerts a dominant influence on the flow around it. As the vortex originating at the sharp edge grows, the boundary layer on the unwetted surface experiences a deceleration due to a steep rise of the pressure. The boundary layer therefore separates and forms a secondary shear layer very near the edge, rotating in opposite sense to the primary vortex. This secondary separation becomes increasingly important with growing wedge internal angles (Rott, 1956). However, its scale remains small and its major effect seems to be a shift in the position of the primary vortex (Smith, 1966). Pullin & Perry (1980) conformed these results and also observed the existence, for large wedge angle, of a region near the wedge apex in which the streamlines form a closed loop on a scale comparable with the secondary vortex region. The same phenomenon was observed by Michael (1955) and more recently by Thompson (1975). This bubble lies entirely within the shear layer and seems to be a region of constant vorticity. However, the effects of viscosity seem to be confined to the boundary layers, and in the inner part of the spiral vortex and they are responsible for the free shear layers formation. Outside these regions

the flow field appears to depend little on the Reynolds number. This encourages the construction of inviscid flow models to describe the large-scale features of the separated flow and, indeed, several authors have observed that, for finite but sufficiently high Reynolds number, the potential flow theory works quite well provided that a correct distribution of vorticity is maintained.

We assume that, in the limit of infinite Reynolds number, a bound vortex sheet exists on the boundary and is shed at the separation point, fixed at the sharp edge, as a free vortex sheet which is convected with the local velocity. In this limit the entire flow is irrotational apart from the vortex sheets, and the problem becomes an inviscid one which can be analysed using potential flow theory. The effects of viscosity AT the separation point are replaced by the Kutta-Joukowski condition which uniquely determines the properties of the free vortex sheet. The problem, concerning the vortex sheet formation by flow separation and its interaction with bodies or boundaries may be formulated in three parts: (a) the potential flow solution (b) the inviscid flow separation (c) the evolution of free vortex sheets.

The vortex sheet generated either by an impulsively started flow or, more generally, by an accelerated flow, rolls up into A spiral and eventually a circular vortex may form. As the rolling-up process continues, the spiral tightens and the velocity which is initially a piecewise continuous function on a section through the spiral centre,

becomes smoothly continuous as a result of viscous effects. The vorticity does not concentrate at a point but moves in concentric circles producing vortices of finite size (Betz, 1932). Moore & Saffman (1973) have shown how the singular behaviour of the velocity field near the spiral centre is resolved by viscous action and how this is crucial for the axial flow in the case of laminar trailing vortices. According to their model, the vortex core forming at the edge may be divided into (a) a tightly wound spiral-like thin shear layer from the edge, (b) a region in which the effects of decreasing spacing between turns of the shear layers, due to the vortex sheet stretching and the layer thickening by viscous diffusion, forms an essentially inviscid rotational core and (c) a viscous subcore. The radius of the first and second region depends upon the internal angle of the wedge and the acceleration. If the flow is suddenly stopped and the vortex sheet is no longer generated at the edge, the radius of the first region remains fairly constant whereas the other two regions grow and eventually viscous effects dominate (Pullin, 1979). Then, the vortex sheet solution may be regarded as an outer inviscid flow which determines the structure of the inner inviscid rotational core and viscous subcore.

The features of the vortex sheet generated at the leading edge of a low aspect-ratio delta wing are in close analogy with the previously described rolling-up process. This suggested to Brown & Michael (1954) the useful approximation of replacing the whole vorticity region by a single concentrated vortex line. Under the condition of conical flow this can be analysed as a single 2-D vortex point

whose strength grows as we move downwards from the apex of the wing. By concentrating the original vortex spiral which does not sustain any force, into a single growing vortex a pressure jump is found on any line connecting the leading edge and the vortex. This is incompatible with the vorticity conservation law. Then, the vortex is subjected to a force which cancels the unbalance of force on the edge-vortex line, leaving only an unbalanced moment. Rott (1956), investigating the starting vortex produced by defraction of a weak shock wave around a sharp infinite edge, generalised Brown & Michael's model for wedge angles different from zero and for flow proportional to time to a general power law. Smith (1968) improved the treatment of the leading edge vortex sheet by adding to the single vortex model a finite part of the vortex sheet starting at the separation point. He found the position of the vortex and the shape of the sheet by applying the Kutta-Joukowski condition at the edge and by verifying the sum of the forces on the sheet and on the vortex were zero. The use of a single tip vortex bypasses the considerable difficulty of finding a proper representation of the spiral core structure (Moore, 1974).

The use of numerical techniques to study the motion of continuous vortex sheets represented by discrete arrays of point vortices is not new. Many authors have used it since it was proposed by Rosenhead (1931) to compute the effect of sinusoidal perturbation on the motion of the sheet. Westwater (1935) used a similar approach to study the rolling up of a vortex sheet behind an airfoil. Fink & Soh (1974)

Clements & Maull (1975) and more recently Saffman & Baker (1979) give extensive reviews of the subject. The velocity field induced by the vorticity distribution may be calculated in two different ways. The 'direct summation' method calculates the velocity by summing the velocity field of each discrete vortex which is given by the Biot-Savart integral. In this method the amount of computation grows as N^2, where N is the number of discrete vortices used. It has been extensively employed to study the evolution of vortex sheets and its advantages as well as its limitations are well known.

In the 'cloud-in-cell' method (Christiansen, 1973), the vorticity is redistributed onto the grid points of an Eulerian regular mesh. Then the Poisson's equation for the stream function Ψ is solved on such a mesh by a very fast method. By finite difference the velocity is found at the grid points from the known values of Ψ and then at each vortex point by interpolation in the cell. The advantage of this method is that the amount of computation is linear in N and far more vortices can be used to obtain a better resolution of vortex jumps. The disadvantages are that flow features of smaller scale than the grid cannot be accurately followed and in the case of vortex sheets disturbances of time scale that are grid dependent appear in the solution (Baker, 1979). Also, the method seems to be affected by an artificial viscosity inherent in the redistribution of the vorticity in the cell and the presence of boundaries is not easily included.

In both methods, once the velocity field is known, the

vortices are moved by a tracking process. The cloud-in-cell method can be very effective in representing interaction of vortices where the vortices are assumed to be N delta-functions whose sum replaces the piecewise continuous distribution of vorticity. No axisymmetric applications of the method exist. In this case it is difficult to find interpolations which conserve the vorticity invariants and an efficient fast method to solve the Poisson's equation with general boundary conditions. However, the fact that viscous effects can be properly included by adding a random walk to the point vortices natural convection (Chorin, 1973) only if the number of point vortices greatly exceeds the Reynold's number (Milinazzo & Saffman, 1977), encourages further applications of the method once its basic features are better understood. In one of the rare applications of the direct vortex point method to internal flows Evans & Bloor (1977) succeeded in representing the starting flow past a flat plate in a channel. They found a distinct and smooth vortex sheet whose growth compared well with experiments as well as the pressure distribution along the channel wall. In one of the few axisymmetric calculations Davies & Hardin (1973) used an direct discrete vortex method to calculate the initial behaviour of an impulsively started circular jet. Starting vortices are not the only large scale structure generated by flow separation. In the case of steady flow, vortex sheets have been observed to appear from the instability of the free shear layers in mixing layers (Browand & Weidman, 1976) in wakes (Bradbury, 1976) and in jets (Beavers & Wilson, 1970). The effect of Helmholtz instability on the shear layer is to produce concentrations

of vorticity at regular intervals which eventually creates vortices of finite size. These vortices start rotating about one another and then amalgamate into larger similar coherent structures which grow continuously by entrainement and eventually disappear in a turbulent mixing layer. This phenomenon, called pairing, was observed by Browand & Weidman (1976) and by Roshko (1976). The growth rate of the Helmholtz instability is proportional to the sheet strength divided by the wavelength of the disturbances. Moore (1976) gave a general analysis of the stability of an arbitrary vortex sheet confirming the previous results. He also showed that in vortex sheets with finite thickness the growth rate is reduced. This seems to confirm early calculations by Michalke(1964) which showed the existence of a wavelength of maximum amplification of disturbances However, he could not find clear details of the vorticity concentration. In contrast, Levy & Hockney's (1968) calculations of the stability and non-linear development of a low density electron beam in a strong magnetic field by the 'cloud-in-cell' method showed the formation of vortices which eventually coalesce into a single vortex whose amplitude was limited by non-linear effects. The system repeated periodically along the initial vortex sheet. The same result was obtained by Christiansen (1973). Moore & Saffman (1975) using the results of their analysis for the stability of vortices of elliptic shape in simple shear flows (1971), explored the conditions for the existence of linear arrays of vortices and of pairs of equal vortices rotating steadily about one another. The predictions are consistent with the observation.

Christiansen & Zabusky (1973) observed the fission of a vortex predicted by Moore & Saffman (1971). Acton (1976) using direct summation showed the formation of clumps from a sinusoidally perturbed thick vortex sheet and observed the pairing of the clumps. Abernathy & Kronauer (1962) tried to explain the essential features of the mechanism of formation of a Karman's vortex street behind a bluff body as the motion of a pair of vortex sheets symmetrically disturbed by a periodic perturbation. Gerrard (1967) calculated the magnitude and the frequency of the lift on a circular cylinder by representing the separated shear layers by arrays of point vortices which were assumed to appear regularly at predetermined positions downstream. The results agree well with the available experimental values

More recently Sarpkaya & Schaoff (1979) studied the wake behind an impulsively started circular cylinder. They calculated the separation points by a quasi-steady calculation of the boundary layer on the cylinder surface and the evolution of the shear layers by the direct summation method suggested by Fink and Soh (1974). Examples of calculations of wakes behind sharp edge bluff bodies by direct summation are Clements & Maull (1975) for flow behind a square-based body and Clements (1973), Sarpkaya (1975) and Kiya & Arie (1977) for a flat plate at incidence.

The vortex growth in jets from nozzle and square edge orifices have been studied extensively since the early work by Johansen (1929). If the Reynolds number, based on the velocity through the orifice and the orifice diameter, is sufficiently high, the jet boundary layer thickness is

small compared to the jet diameter. Then the Strouhal number of the vortices present in the shear layer is proportional to $\sqrt{Re}$. The Strouhal number, St, has been observed to be independent of Re for orifice diameter-to-thickness ratio greater than three and also for lower Re when the laminar boundary layer occupies the whole cross-section of the orifice. Beavers & Wilson (1970) showed that for $500 \leq Re \leq 3000$, St, is independent of Re for sharp-edged flat plate orifices. They observed irregularities on the jet surface for $Re \sim 500$. A small increase in Re resulted in an uninterrupted street of vortex rings uniformly spaced. As the rings moved down-stream, the flow pattern becomes irregular, the vortex rings interact and eventually the regular patterns break up. The length of the vortex growth region shortens as Re is increased and for $Re \sim 3000$ only the first vortex ring was observed. The Strouhal number was 0.63. Beavers & Wilson try to simulate the vortex growth by two parallel lines of 2-D vortex points whose motion was calculated by direct summation. Unlike previous calculations, no wavelength was imposed and the vortex street was only initially disturbed. The results of their computations show that a region of vortex growth can remain stationary in the flow. The existence of such a large axisymmetric eddy structure and its importance is also shown by the high sensitivity of the jet flow to harmonic forcing. Moore (1977) observed that for $S_t < 1$ there was a dramatic 'locking-on' of the large eddies to the exitation frequency. Acton (1980) attempted to calculate the features of the jet by an axisymmetric direct summation model. Reasonable

agreement was found between the model results and experiments as far as the large scale structures are concerned. She also found that in the Strouhal number range $.3 \leq St \leq 2$ a harmonic disturbance was able to excite the jet eddies at the forcing wavelengths. This effect was particularly distinct for $S_t = (.3 \div .5)$, consistent with the experimental observations.

Large scale structure can also be generated by oscillatory flow past bodies. This problem has received considerable attention in recent years because of its relevance to fluid-structure interactions. It has been recently shown (Bearman, Graham & Singh, 1978) that depending on the Keulegan-Carpenter number K, defined as the product of the free stream velocity peak amplitude and the period of oscillation divided by the body characteristic length, that at least two quite different flow regimes exist. For high K the flow past the body separates and the free shear layers form a vortex street which behaves as in the steady flow case. For low K the free shear layers roll up into starting vortices which, because of the shorter amplitude of the oscillations of the flow, are swept back past the body. They interact, coalesce and form larger flow structures which eventually disappear either by cancellation or by viscous decay. In their study of the energy losses of a wave-energy device, Knott & Mackley (1979) have also obtained flow visualisation of vortex rings formed by oscillatory flow in and out of open ended tubes. However, no specific vortex calculations have yet been carried out for this case.

Many turbulent flows are believed to be organised in coherent large scale structure in which viscosity is relatively unimportant. They can develop either into periodic flow patterns in which case a mean flow exists and the fluctuation about its value have a physical meaning or into an aperiodic one. In this case the large scale unsteady mean flow must be identified and the idea of numerical experiments representing turbulence in terms of discrete elements of vorticity may be useful. The concept of representing the large eddies as a collection of vortices certainly agrees with Townsend's idea that they are essentially inviscid. It also seems to be an application of Taylor's vorticity transfer theory which assumes that the vorticity remains constant in a turbulent mixing process. In this sense the idea is not new. Homogeneous turbulence was represented by Synge & Lin (1943) as a collection of Hill's vortices, Onsager (1949) as a random array of point vortices and Townsend (1951) as vortex sheets and tubes. More recently direct summation and cloud-in-cell methods with and without random path have been used to study a variety of problems by Chorin (1973), Christiansen & Zabusky (1973), Clements (1973), Acton (1976, 1980), Kiya & Arie (1977) and Ashurst (1977, 1978). However, the presence of unexplored features of the numerical methods, such as the smoothing of the small scales of motion in the direct summation method due to the small number of vortices used, or the presence of a cell induced artificial viscosity and a cell length scale in the cloud-in-cell method, suggests they may not be adequate to model the turbulent mixing process

and that these methods may be useful only to describe the large scale motions.

In this work we explore the theoretical basis of the extension of the direct summation model to axisymmetric flows. The much more complicated interaction between vortices and the existence of the self-induced velocity of a vortex sheet, among other particular features, make the problem non trivial. Very few other axisymmetric calculations have been published: Davies & Hardin (1973), Acton (1980) and Ashurst (1979). The latter predicted the flow in an axisymmetric piston cavity during a full cycle of a four-stroke engine and compared the results with some flow visualization experiments in water.

We have firstly applied the model to the unbounded starting and oscillatory flow around a disc. This is the axisymmetric analogue of the 2-D flow around a flat plate, a problem which has always received consideration because of its importance in describing the unsteady separated flows past bluff bodies. Recently, the oscillatory case has been the object of considerable attention because of its relevance to wave loading (Graham, 1980). Vibrating discs have also been used in modern mass transfer equipment where the mechanical agitation results in an increase in the dispersed phase and the formation of many small bubbles or drops in the fluid mixing. This leads in general to an improvement of the mass transfer rate. A knowledge of the power dissipation and the flow patterns is undispensible to estimate the mass transfer characteristics and to extend such contactors on the industrial

scale (Tojo et al., 1979).

The second application of the model is the oscillatory flow through a sharp edge orifice in a circular tube. This flow, being bounded, is fundamentally different from the external flows which have been studied using this model.

Research on unsteady flows through constricted tubes has been stimulated by the physiological importance of these flows. Caro, Fitzgerald & Schroter (1971) and Fry (1973) have suggested that hydrodynamic factors may influence the genesis and subsequent development of atherosclerosis. This is a disease involving the development of fatty deposits in the artery wall. In its advanced stage these deposits cause the formation of intravascular atherosclerotic plaques which develop and progressively occlude the artery and lead to serious circulatory disorders such as thrombus formation (Stein & Sabbah, 1974) and the reduction of coronary flow (Mates et al, 1978) with consequent angina pectoris. One of the most important features in the reduction in blood flow to the distal vascular beds supplied by an obstructed artery is the pressure drop across the stenosis (Young & Tsai, 1973) Using a very simple model and forgetting numerous important factors such as the collateral flow, we can say that in the absence of stenosis and at resting conditions, the mean flow rate Q through an artery and its regional bed is equal to the ratio of the pressure difference Δp between arterial and venous system and the peripheral resistance R. Under exercise conditions the peripheral

flow increases several times. For example, in the abdominal aorta of a large dog, the mean flow rate may range from 3.5 cm^3/sec to 40 cm^3/sec and in the carotid artery from 2 cm^3/sec to 16 cm^3/sec. Because Δp remains roughly constant the distal vascular bed must have the ability to change the peripheral resistance. There is, however, a minimum, R_m, below which no further adjustments are possible and the flow rate reaches its maximum value Q_m. If a stenosis develops in the artery such a maximum value is reduced by the pressure drop across the constriction, Δp_s, $Q_m = (\Delta p - \Delta p_s)/R_m$. Therefore, a stenosis which may have little or no effect on the blood flow under resting conditions may significantly effect the maximal flow that can be achieved and create a critical condition. The prediction of pressure drop across a stenosis has been the subject of several studies. Young & Tsai (1973) developed an equation for the unsteady pressure drop which used coefficients which were determinated from steady flow experiments. The predicted peak pressure drop was always found to be lower than that found experimentally. Clark (1976) introduced an apparent friction factor which took into account changes in momentum flux due to the development of the boundary layer. The prediction of both the pressure drop and the pressure recovery away from the constriction were in good agreement with steady and oscillatory flow measurements. Mates et al. (1978) found that flow separation occurs in relatively mild constrictions and suggest that an appreciable portion of the pressure drop is a result of energy dissipation in the recirculation regions. They also observed that for severe stenoses

the total pressure drop was primarily dependent on the minimum area and was relatively independent of the detailed geometry of the stenosis: a sharp-edge orifice and for a long, smooth stenosis behaved similarly. Because of this observation and because the problem of separation from a smooth surface is generally unsolved, even for the simple case of steady flow, we have restricted the present work to sharp edged constrictions where separation can be confidently assumed to occur and its position is fixed. Also, in the case of physiological flows, the study and better understanding of oscillatory flows is required and it is of relevance to the more complex pulsatile flows.

2. AXISYMMETRIC UNSTEADY POTENTIAL FLOW

2.1 Nature of the problem

The potential axisymmetric flow of an incompressible inviscid flow, in either an interior or exterior region, is described by Euler's equation and the continuity equation. In cylindrical co-ordinates (x, r, θ), the axisymmetric velocity is

$$\underline{V} = u(x,r,t)\,\hat{\underline{i}} + v(x,r,t)\,\hat{\underline{j}} \tag{1}$$

and considering only conservative body forces

$$\frac{D\underline{V}}{Dt} = -\frac{1}{\rho}\nabla p(x,r,t) \tag{2}$$

$$\nabla\cdot\underline{V} = \frac{\partial u}{\partial x} + \frac{1}{r}\frac{\partial(rv)}{\partial r} = 0 \tag{3}$$

with boundary conditions

$$\underline{V}\cdot\hat{\underline{n}}\Big|_S = \mathcal{F}(x,r,t) \tag{4}$$

where S is the boundary of the flow defined by the equation

$$F(x,r,t) = 0 \tag{5}$$

$\hat{\underline{n}}$ is the unit normal to S defined as positive on the side of the flow and $\mathcal{F}(x,r,t)$ is a function which is determined by the imposed boundary conditions. For stationary boundaries without sources or sinks, $\mathcal{F} = 0$.

The fluid density ρ is assumed to be constant. It is easily found by introducing the velocity potential $\phi(x,r,t)$ and the Stokes' stream function $\psi(x,r,t)$ defined so that

$$u(x,r,t) = \frac{\partial\phi}{\partial x} = \frac{1}{r}\frac{\partial\psi}{\partial r} \tag{6}$$

$$v(x,\sigma,t)=\frac{\partial\phi}{\partial\sigma}=-\frac{1}{\sigma}\frac{\partial\psi}{\partial x} \tag{7}$$

and applying equation (3), that both ϕ and ψ satisfy the Laplace's equation

$$\nabla^2\phi=\frac{\partial^2\phi}{\partial x^2}+\frac{\partial^2\phi}{\partial\sigma^2}+\frac{1}{\sigma}\frac{\partial\phi}{\partial\sigma}=\nabla^2\psi=\frac{\partial^2\psi}{\partial x^2}+\frac{\partial^2\psi}{\partial\sigma^2}+\frac{1}{\sigma}\frac{\partial\psi}{\partial\sigma}=0 \tag{8}$$

a, b

From equation (2) an equation for the pressure p is derived

$$p/\rho+\frac{1}{2}\underline{V}\cdot\underline{V}+\frac{\partial\phi}{\partial t}=\xi(t) \tag{9}$$

where $\xi(t)$ is an instantaneous constant throughout the flow and $\underline{V}$ is referred to the absolute frame of reference.

Since the problem is linear, the velocity can be expressed as

$$\underline{V}=\underline{V}_\infty+\underline{V}_b+\underline{V}_v \tag{10}$$

where $\underline{V}_\infty(t)$ is the velocity imposed at infinity, $\underline{V}_b(x,\sigma,t)$ is the irrotational disturbance velocity due to the presence of the boundaries, and $\underline{V}_v(x,\sigma,t)$ is the velocity due to the singularities in the flow field. If $\varphi(x,\sigma,t)$ is the potential of the disturbance velocity $\underline{V}_b$ then equation (8a) becomes

$$\nabla^2\varphi=0 \tag{11}$$

and the boundary condtion, equation (4), becomes

$$\nabla\varphi\cdot\hat{\underline{n}}\Big|_S=\frac{D\rho}{Dt}-\underline{V}_\infty\cdot\hat{\underline{n}}\Big|_S-\underline{V}_v\cdot\hat{\underline{n}}\Big|_S=\zeta(x,\sigma,t) \tag{12}$$

Lamb (1932) gives a careful account of methods for solving Laplace's equation in three dimensions with different kinds of boundary conditions. He shows how Spherical Zonal Harmonics or some of their limiting forms may be used to

solve the problem. However, it appears from his analysis that solutions can be found only when the geometry of the problem is simple. In general, we must solve it numerically.

If we extend the problem to the solution of the velocity field for a given distribution of vorticity, $\underline{\omega}$, where

$$\nabla \times \underline{V} = \underline{\omega} \tag{13}$$

when the solution at a general point $\underline{x}$ is given by (Batchelor, 1970)

$$\underline{V}(\underline{x}) = -\frac{1}{4\pi} \int \frac{\underline{S} \times \underline{\omega}}{|S|^3} d\vartheta \tag{14}$$

where the volume integral is extended to all the fluid field and $\underline{S} = \underline{x} - \underline{x}'$ is the distance between a point in the space and a point of the vorticity distribution. It is easily seen that the intergrand of this integral, called either Poisson's or Biot-Savart's integral, is singular for $|\underline{S}| \to 0$

When the vorticity is distributed discretely the velocity $\underline{V}$ may be regarded as the sum of the contribution from different volume elements $\delta\vartheta$

$$\underline{V} = -\sum \frac{(\underline{S} \times \underline{\omega})}{4\pi |\underline{S}|^3} \delta\vartheta \tag{15}$$

This suggests that the boundaries may be imagined as a surface distribution of vorticity, fixed in space and prescribed in order to verify the boundary conditions (12). The local properties of such a surface distribution may be characterised by the parameter $\underline{\gamma}(\underline{x})$ also called the strength of the distribution, defined as

$$\underline{\gamma}(\underline{x}) = \lim_{\varepsilon \to 0} \int_{-\varepsilon}^{\varepsilon} \underline{\omega} (d\underline{l} \cdot \hat{\underline{n}}) \tag{16}$$

Where the strength $\underline{\gamma}$ is constant, the component of the velocity $\underline{V}$ parallel to the surface and perpendicular to $\hat{\underline{n}}$ has a discontinuity of magnitude $|\underline{\gamma}|$

$$\underline{V}(x_0) = \frac{\underline{\gamma} \times \hat{\underline{n}}}{2} \tag{17}$$

This result may be shown to hold locally when the strength $|\underline{\gamma}|$ is not uniform but dependent on $\underline{x_0}$

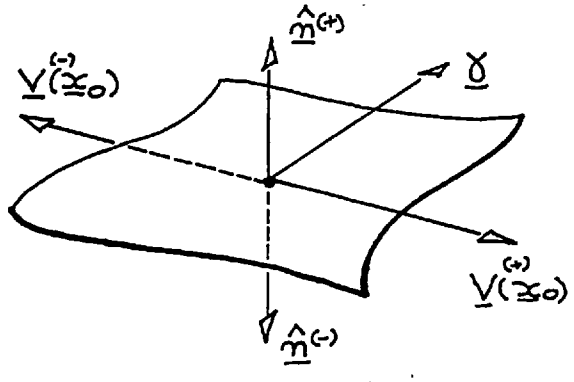

Fig. 2.1

2.2 Review of previous methods

The analysis in section (2.1) shows that a convenient way to solve the Laplace equation (11) may be to convert it into an integral equation by means of the Biot-Savart's law or in general by the Green's theorem. We assume that, at a fixed time t_0, the position and the strength γ of each free vortex sheet present in the flow field is known. The velocity $\underline{V}_v$ can be obtained by combining equation (14) and (15) and integrating over all the wake elements. The function $\zeta(x,\sigma,t)$ is then known and it remains to find the potential field that corresponds to that boundary condition. This is accomplished in the following manner. A continuous distribution of vortex rings is assumed to exist on the boundary. The boundary surface S is approximated by a large number of straight-line surface elements and on each element a check point is selected where the boundary condition equation (12) must be satisfied. The strength of the

distribution is adjusted in order to satisfy the prescribed boundary conditions. This leads, as described in the following section, to a Fredholm's equation of the first kind. The process of solution may be thought of as an operator taking the function $\mathcal{G}$ (or an equivalent one) in equation (12) and producing the velocity $\underline{V}_b$ or the potential φ. Such an operator is independent of time if the boundaries are fixed.

Hess & Smith (1966) developed a similar general and powerful method applying a distribution of sources on the boundaries. The problem is thus transformed to one of solving a Fredholm's integral equation of the second kind. This method was applied to a whole set of steady potential flow problems obtaining a good agreement with both theoretical and experimental results.

Giesing (1968) and more recently Basu and Hancock (1977) investigating the non-linear 2-D unsteady potential flow around an airfoil split the problem into the quasi-steady motion of the airfoil itself and the flow field due to its wake. They solved the first one by applying the source method, previously described, step by step in time and assuming the flow field due to the wake was known at each step by a process of tracking.

Chaplin (1964) investigated the axisymmetric steady flow through a shrouded impulse disc. He wanted to determine the position of the vortex sheet, assumed as a slipstream boundary, shed from the trailing edge of the shroud. Starting from an arbitrary configuration of the

flow field,by a step-by-step converging process, he reached the steady configuration. A distribution of vortex rings was used to simulate the entire boundary. Its strength was determined by applying, as usual, the boundary conditions which required a constant value of the Stokes' stream function ψ at the boundary. As in the present approach, this leads to a Fredholm's equation of the first kind.

2.3 Vortex ring of infinitesimally small core

In the following work the properties of an ideal vortex ring are frequently used. Lamb (1932) gives full account of them and in this section we present a concise review of his articles (Art 161-163) with some convenient and more explicit extensions.

Consider a vortex ring, in an unlimited fluid whose axis of symmetry is centred on the x-axis (see Fig. 2.2). The whole flow field is axisymmetric and there is no azimuthal motion. We describe (Batchelor, 1970) the velocity distribution in terms of the Stokes' stream function ψ The vector potential $\underline{e}$ is related to the velocity by

$$\underline{v} = \nabla \times \underline{e} \tag{18}$$

It has only one non-zero component which is parallel to the one non-zero component of the vorticity $\underline{\omega}$. In cylindrical co-ordinates

$$\psi = \psi(x,\sigma)\,;\ \underline{v} \equiv (u(x,\sigma);\ v(x,\sigma))\,;\ \underline{\omega} = \underline{\omega}(x,\sigma)\,;\ \underline{e} = \underline{e}(x,\sigma)$$

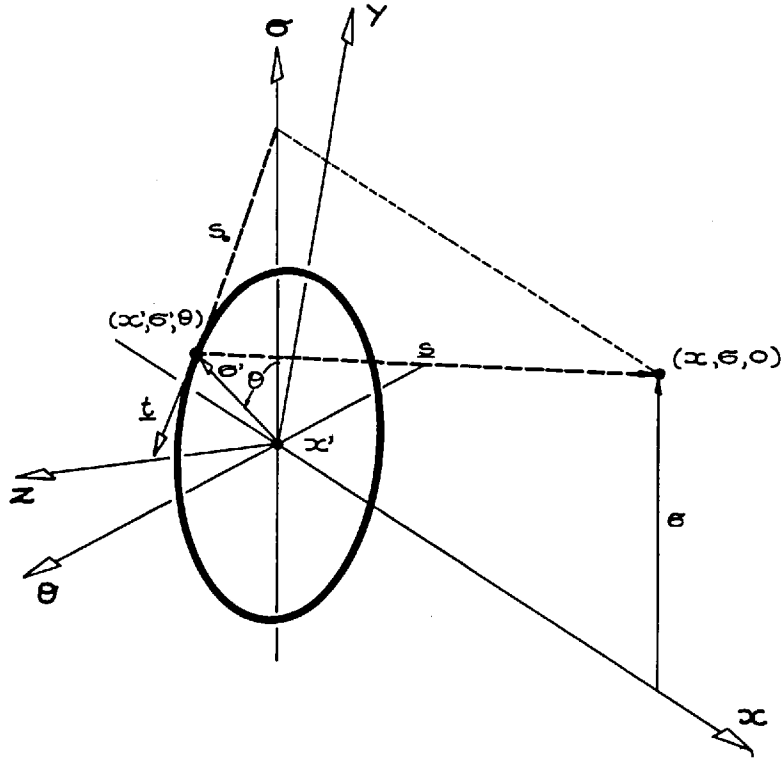

Fig. 2.2

Now explicitly

$$\underline{V} = \left\{ \frac{1}{\sigma}\frac{\partial}{\partial\sigma}(\sigma e_\theta) - \frac{1}{\sigma}\frac{\partial}{\partial\theta}(e_\theta) \right\}\hat{\underline{\imath}} + \left\{ \frac{1}{\sigma}\frac{\partial}{\partial\theta}(e_x) - \frac{\partial}{\partial x}(e_\theta) \right\}\hat{\underline{\jmath}} +$$

(i) (ii)

$$+ \left\{ \frac{\partial}{\partial x}(e_\sigma) - \frac{\partial}{\partial\sigma}(e_x) \right\}\hat{\underline{k}}$$

(iii)

where (i), (ii), and (iii) are zero because of the non-dependence on θ so assuming $e_\theta = e$

$$\underline{V} = \frac{1}{\sigma}\frac{\partial}{\partial\sigma}(\sigma e)\hat{\underline{\imath}} - \frac{\partial\sigma}{\partial x}\hat{\underline{\jmath}} \tag{19}$$

Using the stream function

$$\underline{V} = \frac{1}{\sigma}\left(-\frac{\partial\psi}{\partial x}\hat{\underline{\imath}} + \frac{\partial\psi}{\partial\sigma}\hat{\underline{\jmath}} \right) \tag{20}$$

we get

$$\psi = \sigma e \tag{21}$$

We assume that the cross-section of the vortex filament is small, constant and equal to dA

$$d\vartheta = dA\, ds$$

$$\underline{\omega}\, d\vartheta = (\omega\, dA\, ds)\hat{\underline{t}} = d\Gamma\, ds\, \hat{\underline{t}} \tag{22}$$

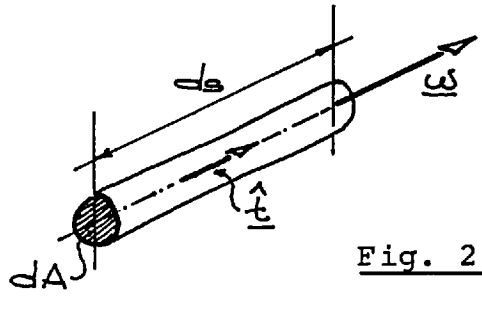

Fig. 2.3

where $\hat{\underline{t}}$ is the unit vector locally tangent to the vortex filament. So the vector potential $\underline{e}$ may be written

$$\underline{e}(x;x') = \frac{1}{4\pi}\int_{\vartheta}\frac{\omega'}{|\underline{s}|}d\vartheta' = \frac{d\Gamma}{4\pi}\int_{\mathcal{L}}\frac{\hat{t}\, ds}{|x-x'|} \tag{23}$$

Some other geometrical relations have to be worked out

to make the vector potential explicit in the case of a vortex ring (see Fig. 2.2)

$$|\underline{s}| = \left[(x-x')^2 + s_o^2\right]^{1/2} \; ; \; s_o^2 = \sigma^2+\sigma'^2-2\sigma\sigma'\cos\theta \qquad (24)\ a,\ b$$

$$d\ell\,\hat{\underline{t}} = \sigma'\left(-\sin\theta\, d\theta\,\hat{\underline{\sigma}} + \cos\theta\, d\theta\,\hat{\underline{\theta}}\right) \qquad (25)$$

By using equations (24) and (25) in equation (23) we have

$$\underline{e}(\underline{x};\underline{x}') = \frac{\sigma' d\Gamma}{4\pi}\left\{-\int_0^{2\pi}\frac{\sin\theta\,\hat{\underline{\sigma}}\,d\theta}{|\underline{s}|}_{(i)} + \int_0^{2\pi}\frac{\cos\theta\,\hat{\underline{\theta}}\,d\theta}{|\underline{s}|}\right\} \qquad (26)$$

The function $|\underline{s}|$ is an even function of θ and since $\sin\theta$ is an odd function of θ the integral (i) is zero. Then

$$\underline{e}(\underline{x};\underline{x}') = \left\{\frac{\sigma' d\Gamma}{4\pi}\int_0^{2\pi}\frac{\cos\theta}{s}\,d\theta\right\}\hat{\underline{\theta}} \qquad (27)$$

Note that nothing changes if we assume $\theta = \theta' - \theta$ and we use the periodicity of all the integrands.

If we make $dA \to 0$ by the assumption of an infinitesimally thin ring we will be able to consider $d\Gamma \to \Gamma'$ without any extra consideration. Then, from the relation (21)

$$\psi(x,\sigma;x',\sigma') = \sigma\sigma'\lambda\int_0^{2\pi}\frac{\cos\theta\,d\theta}{\left[(x-x')^2+\sigma'^2+\sigma^2-2\sigma\sigma'\cos\theta\right]^{1/2}} \qquad (28)$$

where $\lambda = \Gamma'/4\pi$. The velocity components can be easily derived by differentiating the relation (28).

$$u(x,\sigma;x',\sigma') = \frac{1}{\sigma}\frac{\partial\psi}{\partial\sigma} = 2\lambda\frac{\sigma'}{\sigma}\left\{\int_0^{\pi}\frac{\cos\theta}{s}_{(i)}\,d\theta + \right. \qquad (29)$$

$$\left. - \sigma\int_0^{\pi}\frac{(\sigma-\sigma'\cos\theta)\cos\theta}{s^3}_{(ii)}\,d\theta\right\}$$

$$v(x,\sigma;x',\sigma') = -\frac{1}{\sigma}\frac{\partial \psi}{\partial x} = \lambda\sigma' \left\{ \underbrace{\int_0^{2\pi} \frac{2(x-x')\cos\theta \, d\theta}{s^3}}_{(iii)} \right\} \quad (30)$$

The integrals (i), (ii) and (iii) are obtained in the Appendix and the final explicit relations for ψ, u and v are

$$\psi(x,\sigma;x',\sigma') = 2\lambda\sqrt{(\sigma+\sigma')^2+(x-x')^2}\left[\frac{\sigma^2+\sigma'^2+(x-x')^2}{(\sigma+\sigma')^2+(x-x')^2}\mathbb{K}(m) - \mathbb{E}(m)\right] \quad (31)$$

$$u(x,\sigma;x',\sigma') = \frac{2\lambda}{\sqrt{(\sigma+\sigma')^2+(x-x')^2}}\left[\mathbb{K}(m) - \frac{\sigma^2-\sigma'^2+(x-x')^2}{(\sigma-\sigma')^2+(x-x')^2}\mathbb{E}(m)\right] \quad (32)$$

$$v(x,\sigma;x',\sigma') = \frac{-2\lambda(x-x')}{\sigma\sqrt{(\sigma+\sigma')^2+(x-x')^2}}\left[\mathbb{K}(m) - \frac{\sigma^2+\sigma'^2+(x-x')^2}{(\sigma-\sigma')^2+(x-x')^2}\mathbb{E}(m)\right] \quad (33)$$

where $\mathbb{K}(m)$ and $\mathbb{E}(m)$ are the complete elliptic integrals of the first and second kind with the argument

$$m = \frac{4\sigma\sigma'}{(x-x')^2+(\sigma+\sigma')^2} \quad (34)$$

The behaviour of the flow field near the x-axis ($\sigma \to 0$) may be obtained by expanding equation (31), (32) and (33) in power of σ for σ small.

Define $\bar{x} = x - x'$ then

$$m = \frac{4\sigma\sigma'}{\bar{x}^2+\sigma'^2}\left(1 - \frac{2\sigma\sigma'}{\bar{x}^2+\sigma'^2}\right) + O(\sigma^3) \quad (35)$$

For $|m| \ll 1$

$$K(m) = \frac{\pi}{2}\left[1 + \frac{m}{4} + \frac{9}{64}m^2 + \cdots\right] + o(m^3)$$

$$E(m) = \frac{\pi}{2}\left[1 - \frac{m}{4} - \frac{3}{64}m^2 + \cdots\right] + o(m^3) \qquad (36)\ a,\ b$$

Using equations (35) and (36a, b) in equation (32) we have

$$u(x,\sigma;x',\sigma') = \left\{\frac{\pi\lambda}{\sigma^2}\sqrt{(\sigma+\sigma')^2+\bar{x}^2}\left[\left(1-\frac{\sigma^2}{\bar{x}^2+\sigma'^2}\right)(1-2\zeta)+\right.\right.$$
$$+\left.\frac{(3\sigma'^2-\bar{x}^2)\sigma^2}{\bar{x}^2+\sigma'^2}\left(1+\zeta+\frac{1}{4}\zeta^2\right)-\left(1-\zeta+\frac{5}{4}\zeta^2\right)\right]\Bigg\}+$$
$$+\left\{\frac{\pi\lambda(\bar{x}^2+\sigma'^2)}{\sigma^2\sqrt{(\sigma+\sigma')^2+\bar{x}^2}}\left[-\left(1+\zeta+\frac{1}{4}\zeta^2\right)+\right.\right. \qquad (37)$$
$$+\left.\left.(1+2\zeta+2\zeta^2)\left(1-\zeta+\frac{5}{4}\zeta^2\right)\right]\right\}+o(\zeta^3)=$$
$$= A + B + o(\zeta^3)$$

where $\zeta = \sigma\sigma'/(\bar{x}^2+\sigma'^2)$ Eventually we have

$$A = \frac{\pi\lambda\sigma'^2\left[(\sigma+\sigma')^2+\bar{x}^2\right]^{1/2}}{(\bar{x}^2+\sigma'^2)^2} \qquad (38)$$

$$B = \frac{\pi\lambda\sigma'^2}{(\bar{x}^2+\sigma'^2)\left[(\sigma+\sigma')^2+\bar{x}^2\right]^{1/2}} \qquad (39)$$

thus for $\sigma \ll 1$

$$u(x,\sigma;x',\sigma') \cong \pi\lambda\sigma'^2\,\frac{(1+2\sigma')\sigma+2\left[\sigma'^2+(x-x')^2\right]}{\left[(x-x')^2+\sigma'^2\right]\left[(\sigma+\sigma')^2+(x-x')^2\right]^{1/2}} \qquad (40)$$

on the x-axis we have

$$u(x,0;x',\sigma') = 2\lambda\sigma'^2\pi\left[(x-x')^2+\sigma'^2\right]^{-3/2} \qquad (41)$$

This can be easily obtained by substituting $K=E=\pi/2$ into equation (32). Then the velocity at the point on the axis in the plane of the ring is

$$u(0,0;x',\sigma') = 2\lambda\pi/\sigma' \qquad (42)$$

Note that the same result can be obtained by the following quite simple considerations

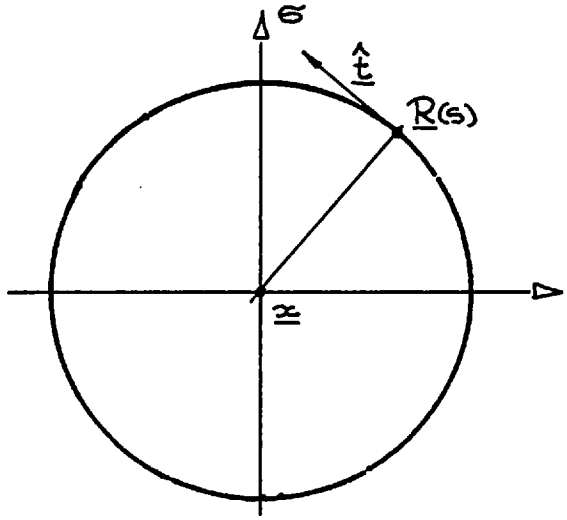

Fig. 2.4

$$R = |\underline{R}(x)-\underline{x}|$$

$$R\hat{\underline{t}} = -(\underline{x}-\underline{R}(s))\times\hat{\underline{t}}$$

using Biot-Savart integral (2.1.14)

$$\underline{V}(\underline{x}) = \lambda\int_{\odot}\frac{\hat{\underline{t}}\times[\underline{x}-\underline{R}(s)]\,ds}{|\underline{x}-\underline{R}(s)|}$$

hence $u(0,R)=\lambda 2\pi R/R^2 = 2\lambda\pi/R$ as before. Now we transform equation (33)

$$v(x,\sigma;x',\sigma') = -\frac{\pi\lambda\bar{x}^2}{\sigma\sqrt{(\sigma+\sigma')^2+\bar{x}^2}}\left[1+\xi+\frac{1}{4}\xi^2+\right.$$

$$\left.-(1+2\xi+4\xi^2)(1-\xi+\tfrac{5}{4}\xi^2)\right]+O(\xi^3) = \qquad (43)$$

$$= \frac{3\pi\lambda\sigma'^2\sigma(x-x')}{\left[(x-x')^2+\sigma'^2\right]\left[(\sigma+\sigma')^2+(x-x')^2\right]^{1/2}}$$

Thus

$$v(x,0;x',\sigma') = 0 \tag{44}$$

As expected the x-axis is a stream line. It is easy to obtain the behaviour of the stream function ψ when $\sigma \to 0$ by the previous method

$$\psi(x,\sigma;x',\sigma') \cong 2\lambda\sigma\sigma' \left[(\sigma+\sigma')^2 + (x-x')^2\right]^{-1/2} \tag{45}$$

hence $\psi(x,0;x',\sigma') = 0$

Note that a positive strength of the vortex ring gives a positive value of the velocity on the axis. Such a velocity goes to zero as $\bar{x} \to \infty$ and presents its maximum for $\bar{x}=0$ The velocity $v(0,\sigma;x',\sigma')$ starts from $\sigma = 0$ with zero value and increases to infinity as $\sigma \to \sigma'$ and then decreases to zero again as $\sigma \to \infty, x'=0$

For many purposes in the following work it is convenient to have series expansions of the velocity components near the vortex ring. Defining

$$\eta = \left[(\sigma-\sigma')^2 + (x-x')^2\right]^{1/2} / \sigma' \tag{46}$$

$$\theta = \tan^{-1}\left[(\sigma-\sigma')/(x-x')\right] \tag{47}$$

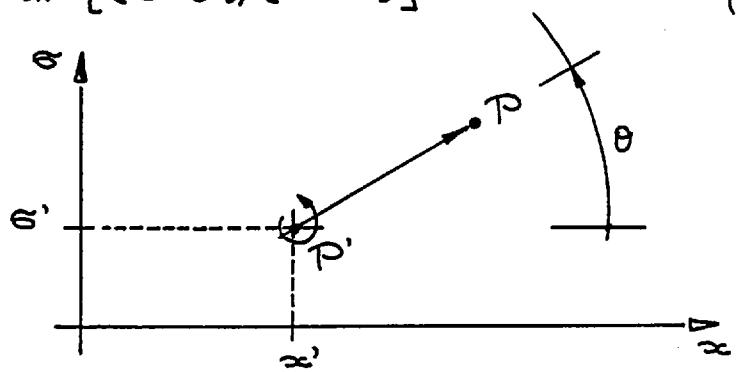

and, for convenience, $x'=0$

Fig. 2.5

we transform equations (32) and (33) into

$$u(\eta,\theta)=\frac{\lambda}{\sigma'(1+\eta\sin\theta+\eta^2/4)^{1/2}}\left[\mathbb{K}(m)-(1+2\sin\theta/\eta)\mathbb{E}(m)\right] \quad (48)$$

$$v(\eta,\theta)=\frac{-\lambda\eta\cos\theta}{\sigma(1+\eta\sin\theta+\eta^2/4)^{1/2}}\left[\mathbb{K}(m)-(1+2\sin\theta/\eta+2/\eta^2)\mathbb{E}(m)\right] \quad (49)$$

Then equations (48) and (49) can be properly expanded for $\eta\to 0$
So we have for $\eta<<1$

$$(1+\eta\sin\theta+\eta^2/4)^{-1/2}=1-\frac{1}{2}\left[(\eta+4\sin\theta)\frac{\eta}{4}\right]+\frac{3}{8}\left[(\eta+4\sin\theta)\frac{\eta}{4}\right]^2+$$
$$-\frac{5}{16}\left[(\eta+4\sin\theta)\frac{\eta}{4}\right]^3+\ldots=$$
$$=1-\frac{\sin\theta}{2}+\frac{1}{8}(3\sin^2\theta-1)\eta^2+\frac{\sin\theta}{16}(3-5\sin^2\theta)\eta^3+O(\eta^4) \quad (50)$$

$$m=\frac{(1+\eta\sin\theta)}{(1+\eta\sin\theta+\eta^2/4)}=1-\frac{\eta^2/4}{(1+\eta\sin\theta+\eta^2/4)}=1-m'$$

$$m'=\frac{\eta^2}{4}\left\{1-\left[(4\sin\theta+\eta)\frac{\eta}{4}\right]+\left[(4\sin\theta+\eta)\frac{\eta}{4}\right]^2-\left[(4\sin\theta+\eta)\frac{\eta}{4}\right]^3+\ldots\right\}= \quad (51)$$
$$=\frac{\eta^2}{4}\left\{1-\sin\theta\,\eta+\frac{1}{4}(4\sin^2\theta-1)\eta^2-\frac{\sin\theta}{2}(2\sin^2\theta-1)\eta^3+\right.$$
$$\left.+\frac{1}{16}(16\sin^4\theta-12\sin^2\theta+3\sin\theta)\eta^4+O(\eta^5)\right\}$$

$$\ln\frac{16}{m'}=\ln\frac{64}{\eta^2}+\left[\sin\theta\,\eta-\frac{1}{4}(2\sin^2\theta-1)\eta^2+\frac{1}{12}(4\sin^2\theta-3)\sin\theta\,\eta^3+\right. \quad (52)$$
$$\left.-\frac{1}{32}(8\sin^4\theta-8\sin^2\theta+1)\eta^4+O(\eta^5)\right.$$

An appropriate expansions of the elliptic functions for $m \to 1$ is

$$K(m) = \frac{1}{2}\ln\frac{16}{m'}\left\{1+\left(\frac{1}{2}\right)^2 m' + \left(\frac{1\cdot3}{2\cdot4}\right)m'^2 + \left(\frac{1\cdot3\cdot5}{2\cdot4\cdot6}\right)^2 m'^3 + O(m'^4)\right\} + \\ -\left\{\left(\frac{1}{2}\right)^2\frac{2}{1\cdot2}m' + \left(\frac{1\cdot3}{2\cdot4}\right)^2\left(\frac{2}{1\cdot2}+\frac{2}{3\cdot4}\right)m'^2 + \left(\frac{1\cdot3\cdot5}{2\cdot4\cdot6}\right)^2\left(\frac{2}{1\cdot2}+\frac{2}{3\cdot4}+\frac{2}{5\cdot6}\right)m'^3 + O(m'^4)\right\} \quad (53)$$

or explicitly

$$K(m) = \frac{1}{2}\ln\frac{16}{m'}\left\{1+\frac{1}{4}m' + \frac{9}{64}m'^2 + \frac{25}{256}m'^3 + O(m'^4)\right\} + \\ + \left\{\frac{1}{4}m' + \frac{21}{128}m'^2 + \frac{185}{1536}m'^3 + O(m'^4)\right\} \quad (54)$$

$$E(m) = \frac{1}{2}\ln\frac{16}{m'}\left\{\frac{1}{2}m' + \left(\frac{1}{2}\right)^2\frac{3}{4}m'^2 + \left(\frac{1\cdot3}{2\cdot4}\right)\frac{5}{6}m'^3 + O(m'^4)\right\} + 1 + \\ -\left\{\frac{1}{2}\left(\frac{1}{1\cdot2}\right)m' + \left(\frac{1}{2}\right)^2\frac{3}{4}\left(\frac{2}{1\cdot2}+\frac{2}{3\cdot4}\right)m'^2 + \left(\frac{1\cdot3}{2\cdot4}\right)^2\frac{5}{6}\left(\frac{2}{1\cdot2}+\frac{2}{3\cdot4}+\frac{2}{5\cdot6}\right)m'^3 + O(m'^4)\right\} \quad (55)$$

or explicitly

$$E(m) = \frac{1}{2}\ln\frac{16}{m'}\left\{\frac{1}{2}m' + \frac{3}{16}m'^2 + \frac{15}{128}m'^3 + O(m'^4)\right\} + 1 + \\ - \left\{\frac{1}{4}m' + \frac{7}{32}m'^2 + \frac{37}{256}m'^3 + O(m'^4)\right\} \quad (56)$$

we use

$$m'^2 = \frac{\eta^4}{16}\left[1 - 2\sin\theta\,\eta + \frac{1}{2}(6\sin^2\theta - 1)\eta^2 - \frac{\sin\theta}{2}(8\sin^2\theta - 3)\eta^3 + O(\eta^4)\right] \quad (57)$$

to get finally

$$K(m) = \left\{\ln 8 + \frac{1}{2}\sin\theta\,\eta + \frac{1}{16}(1 + \ln 8 - 4\sin^2\theta)\eta^2 + O(\eta^3)\right\} + \\ - \frac{1}{2}\ln\eta^2\left\{1 + \frac{1}{16}\eta^2 + O(\eta^3)\right\} \quad (58)$$

$$E(m) = \left\{1 + \frac{1}{16}(2\ln 8 - 1)\eta^2 + \frac{1}{8}(1 - \ln 8)\sin\theta\,\eta^3 + O(\eta^4)\right\} + \\ - \frac{1}{2}\ln\eta^2\left\{\frac{1}{8}\eta^2 - \frac{1}{8}\sin\theta\,\eta^3 + O(\eta^4)\right\} \tag{59}$$

The desired expansions can then be obtained as before. The results are

$$u(\eta,\theta) = \frac{\lambda}{\sigma'}\left\{\left[-\frac{2\sin\theta}{\eta} + (\sin^2\theta + \ln 8 - 1) + \frac{\sin\theta}{8}(11 - 8\ln 8 - \sin^2\theta)\eta + \right.\right. \\ \left. + \frac{1}{16}(4 - 3\ln 8 + 12\sin^2\theta\ln 8 - 25\sin^2\theta + 10\sin^4\theta)\eta^2 + O(\eta^3)\right] + \\ \left. - \frac{1}{2}\ln\eta^2\left\{1 - \frac{5}{4}\sin\theta\,\eta + \frac{3}{16}(4\sin^2\theta - 1)\eta^2 + O(\eta^3)\right\}\right. \tag{60}$$

and

$$v(\eta,\theta) = \frac{\lambda\cos\theta}{\sigma}\left\{\left[\frac{2}{\eta} + \sin\theta + \frac{1}{8}(5 - 6\ln 8 - 2\sin^2\theta)\eta + \right.\right. \\ + \frac{1}{16}(6\ln 8\sin\theta - 11\sin\theta + 2\sin^3\theta)\eta^2 + O(\eta^3)\left.\right] + \\ \left. + \frac{1}{16}\ln\eta^2\left[6\eta - 3\sin\theta\,\eta^2 + O(\eta^3)\right]\right\} \tag{61}$$

Finally, in order to complete this point, it should be noticed that the non-dimensional variables (η , θ) might be chosen in a different way. For example

$$\eta' = \left[(\sigma - \sigma')^2 + (x - x')^2\right]^{1/2}/\sigma \tag{62a}$$

$$\theta = \tan^{-1}\left[(\sigma' - \sigma)/(x' - x)\right] \tag{62b}$$

Under these conditions the equation (61) is invariant but equation (60) changes and the new relation is

$$u(\eta',\theta)=\frac{\lambda}{\sigma}\left\{\frac{1}{2}\ln\frac{64}{\eta'^2}\left[1-\frac{1}{4}\sin\theta\,\eta'+\frac{1}{16}(4\sin^2\theta-3)\eta'^2\right]+\right.$$
$$+\left[\frac{2\sin\theta}{\eta'}-\cos^2\theta-\frac{1}{8}(2\sin^2\theta-5)\sin\theta\,\eta'+\right. \qquad (63)$$
$$\left.\left.+\frac{1}{16}(2\sin^4\theta-9\sin^2\theta+4)\eta'^2\right\}+O(\eta'^3)\right.$$

It is convenient to transform equation (61) in a similar form and give the result for the stream function too. So we have

$$v(\eta',\theta)=\frac{\lambda\cos\theta}{\sigma'}\left\{\frac{1}{2}\ln\frac{64}{\eta'^2}\left[\frac{3}{4}\eta'-\frac{3}{8}\sin\theta\,\eta'^2\right]+\right.$$
$$-\left[\frac{2}{\eta'}+\sin\theta-\frac{1}{8}(2\sin^2\theta-5)\eta'+\right. \qquad (64)$$
$$\left.\left.+\frac{1}{16}(2\sin^2\theta-11)\sin\theta\,\eta'^2\right]\right\}+O(\eta'^3)$$

and

$$\psi(\eta',\theta)=2\sigma\lambda\left\{\frac{1}{2}\ln\frac{64}{\eta'^2}\left[1+\frac{1}{2}\sin\theta\,\eta'-\frac{1}{16}(2\sin^2\theta-3)\eta'^2+\right.\right.$$
$$\left.+\frac{\sin\theta}{32}(2\sin^2\theta-3)\eta'^3\right]-\left[2+\frac{1}{2}\sin\theta\,\eta'-\frac{1}{16}(4\sin^2\theta-1)\eta'^2+\right. \qquad (65)$$
$$\left.\left.+\frac{1}{48}(7\sin^2\theta-6)\sin\theta\,\eta'^3\right]\right\}+O(\eta'^4)$$

These expansions are the same as those obtained by Chaplin (1964).

2.4 Outline of the method used

As suggested in section (2.2), we approximate a boundary surface by a continuous distribution of vortex rings. The boundary condition (12) becomes

$$\frac{1}{4\pi}\int_S \gamma(x',\sigma',t)\left[\tilde{u}\,F_{,x} + \tilde{v}\,F_{,\sigma}\right]d\ell' = \mathcal{G}(x,\sigma,t) \tag{67}$$

where

$$\frac{\gamma}{4\pi}(\tilde{u},\tilde{v}) = \lambda(\tilde{u},\tilde{v}) = (u,v) \tag{68}$$

is the velocity at (x,σ) due to a unit vortex ring at (x',σ') The u and v velocity are given in equations (32) and (33).

Equation (67) is a Fredholm's equation of the first kind. An approximate solution can be obtained as follows. The boundary is approximated by conical segments. The integrand between successive midpoints of the segment is assumed to be constant and equal to its value at the junction. So the function $\gamma(s)$ is transformed into a finite set of values and the integral (67) may be evaluated. However, an extra contribution arises from the singular behaviour of the integrand and then from the principal value of the integral (67). This has to be analytically evaluated assuming a linear behaviour of $\gamma(s)$ on the singular element. Then, its contribution which as we see in the following increases logarithmically with the length of the singular segment, is expressed as a function of the discrete distribution of the strength γ. Thus the velocity induced at any point by each segment may be determined up to the unknown multiplicative constant γ. Equation (67) is then applied at each segment midpoint and a number of

linear equations equal to the number of unknown values is obtained.

2.5 Geometrical features of the surface elements

Let us define $N+1$ points of the boundary surface and join them by straight line segments.

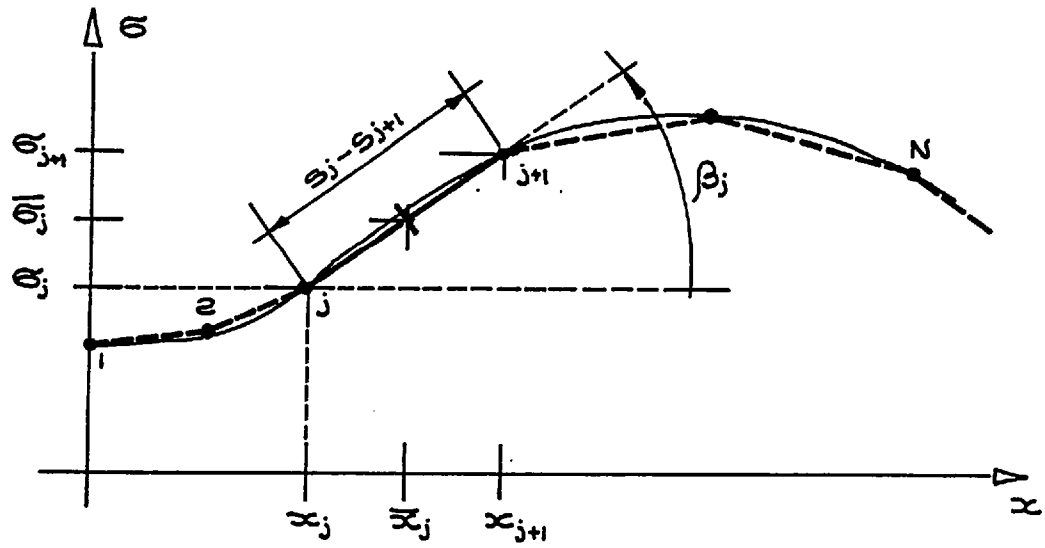

Fig. 2.6

On each element we can define some geometrical parameters. The total length s of the profile is measured starting from P_1 and the arc length associated with the joint P_{j+1} and denoted by s_{j+1} is

$$\begin{cases} s_{j+1} = s_j + \left[\Delta\sigma_j^2 + \Delta x_j^2\right]^{1/2} & j = 1,\dots,N+1 \\ s_1 = 0 \end{cases} \qquad (69\ a,\ b)$$

where $\Delta\sigma_j = \sigma_{j+1} - \sigma_j$ and $\Delta x = x_{j+1} - x_j$; then the slope angle functions are defined by

$$\begin{cases} \sin\beta_j = \Delta\sigma_j / \Delta s_j \\ \cos\beta_j = \Delta x_j / \Delta s_j \end{cases} \qquad j = 1,\dots,N \qquad (70\ a,\ b)$$

where $\Delta s_j = s_{j+1} - s_j$ The midpoint associated with P_j

$$\begin{cases} \bar{x}_i = \delta_{ij}(x_{j+1} + x_j)/2 \\ \bar{\sigma}_i = \delta_{ij}(\sigma_{j+1} + \sigma_j)/2 \end{cases} \qquad i,j = 1,\dots,N \qquad (71)\ a,\ b$$

WHERE δ_{ij} IS THE KRONACKER OPERATOR

The index i will be used in the following for the check-points and the index j for the joints.

When the geometry consists of more than two boundaries joined together a different ordering must be used as shown in Fig. (2.7). In this case the fluid is present on ~~either~~ both sides of the wall leaving the main boundary at the joint N_0 and ends at N_f . We call such a wall a "thin-wall". We redefine the boundary in such a way that the first part is for $j=1,2,\dots,N_f$ and the second for $j = N_0, N_f+1,\dots,N+1$ The major problem is that cross points like P_{N_0} are double stagnation points and are, therefore, sources of spurious solutions

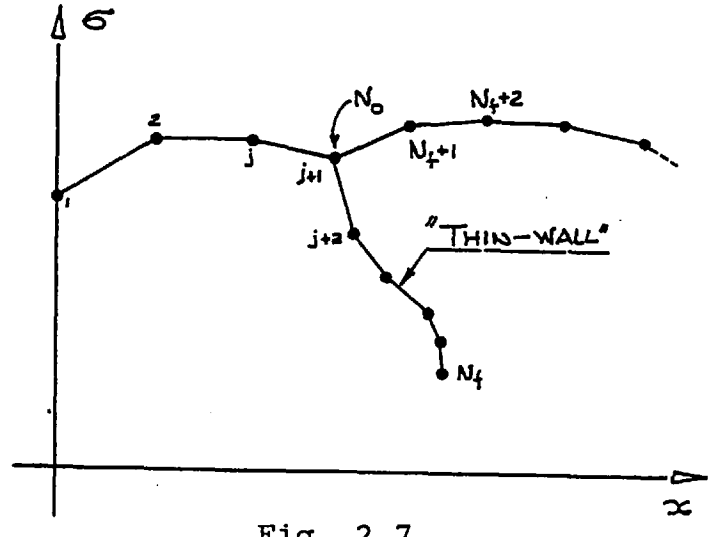

Fig. 2.7

of the type discussed by Craggs and Mangler (1971). This problem can be avoided by smoothing them out into less concave surfaces.

In the present investigation end points such as P_{N_f} are separation points, where vorticity is shed into the main stream and vorticity is formed. This is not the only

kind of sharp edge we are dealing with and more generally we treat cases of edges with non-zero internal angle δ as shown in Fig. (2.8).

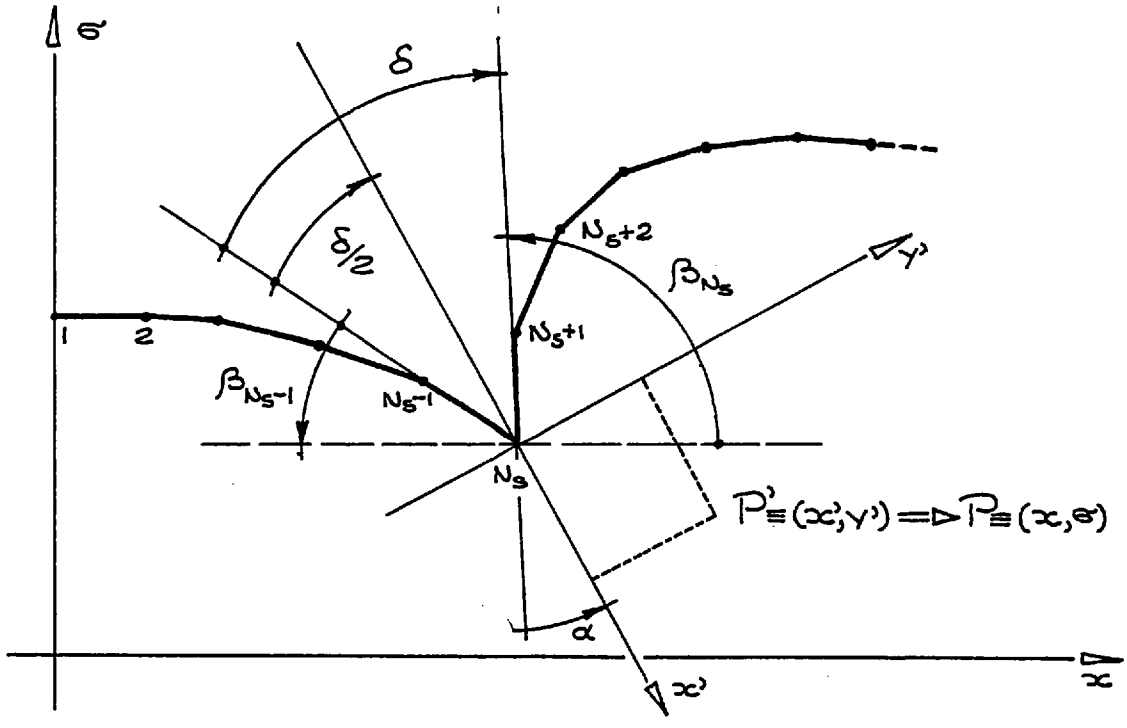

Fig. 2.8

It is convenient to solve the behaviour of the flow around the edge, identified by N_s joint number, in a local rotated (x',y') frame of reference. Then, the point P is identified by

$$\begin{cases} x = x_{N_S} + (x' \sin\alpha + y' \cos\alpha) \\ \sigma = \sigma_{N_S} - (x' \cos\alpha - y' \sin\alpha) \\ \alpha = \frac{\pi}{2} - (-\beta_{N_S-1} + \frac{\delta}{2}) \end{cases} \qquad (72)\ a,\ b$$

where δ is the sharp edge internal angle given by

$$\delta = \pi - (\beta_{N_S} - \beta_{N_S-1}) \qquad (73)$$

Also, we assume that $\Delta s_{N_S} = \Delta s_{N_S-1}$

The velocity $\underline{V}$ of the midpoint of an element in the local frame of reference $(\hat{\underline{n}}, \hat{\underline{t}})$ is given by

$$\underline{V}(\bar{x}_j, \bar{\sigma}_j) = -k\left[u \sin\beta_j - v\cos\beta_j\right]\hat{\underline{n}} + \left[u\cos\beta_j + v\sin\beta_j\right]\hat{\underline{t}} \qquad (74)$$

where $k=-1$ for internal flows and $k=1$ for external flows.

It should be emphasized that the surface elements essentially define integration increments and normal directions for the numerical solution of the equation (67). It is only at the check points that the velocity assumes the prescribed value and it is not zero at any other point, showing a singular behaviour at the joint points. The accuracy is prescribed by the number of elements and their distribution. From our experience and for the kinds of flow analysed a number of elements between 40 for the simplest case and 100, fixed by the computer size, gives a fair approximation of the potential flow (see Fig. 2.14, 2.15). A proper distribution of the elements is a critical problem. They should be concentrated where a rapid variation of the flow field is expected. So sharp edges or high-curvature regions need a greater concentration. As d, the distance along the boundary from the edge decreases, Δ, the size of the element should decrease. Using results from the next chapter, it can be seen that $\Delta \propto d^{1/\lambda}$ where $\lambda = 2 - \delta/\pi$. In general, the size of the elements has to change gradually without jumps.

2.6 Matrix of influence coefficients

A single isolated vortex ring is defined to exist at each j^{th} joint. Its strength Γ_j is given by the total circulation between the mid-points of two successive elements.

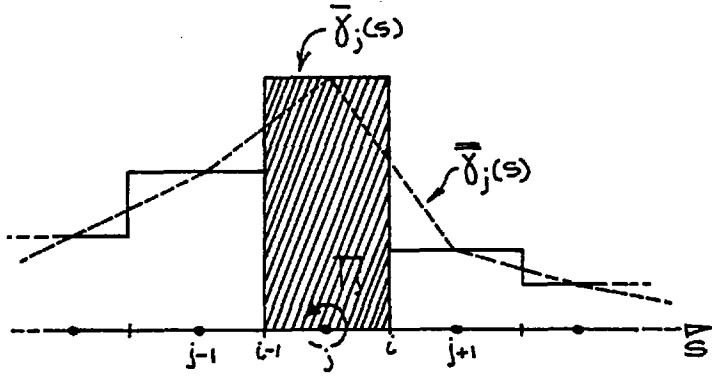

Fig. 2.9

This is

$$\Gamma_j = \frac{\bar{\gamma}_j(s)}{4\pi}\left(\frac{\Delta s_j + \Delta s_{j-1}}{2}\right) \tag{75}$$

Then the velocity components induced at the i^{th} mid-point P_i by a vortex ring of strength $1/4\pi$ at the j^{th} point P_j is given by the equation (68)

$$u(x_i,\sigma_i)=\lambda\,\tilde{u}(x_i,\sigma_i;x_j,\sigma_j)=\lambda\,\tilde{U}_{i,j} \tag{76}$$

$$v(x_i,\sigma_i)=\lambda\,\tilde{v}(x_i,\sigma_i;x_j,\sigma_j)=\lambda\,\tilde{V}_{i,j} \tag{77}$$

Part of the matrix can be now obtained by equations (67), (74), (76) and (77)

$$\sum_1^N{}_j\, k\left[\tilde{V}_{i,j}\cos\beta_i - \tilde{U}_{i,j}\sin\beta_i\right]\Gamma_j = \bar{G}_{1i} \qquad i=1,2,\ldots,N \tag{78}$$

or

$$\sum_1^N{}_j\, A^{(1)}_{i,j}\,\Gamma_j = \bar{G}_{1i} \qquad i=1,2,\ldots,N \tag{79}$$

When $i=j$ we must add the contributions of the principal value of integral (67) upon the two successive elements joined at P_j

Let us investigate generally the j^{th} element and assume

that the strength of the distribution is uniform and equal to $\bar{\bar{\gamma}}(s_i)$ The integral (67) can then be

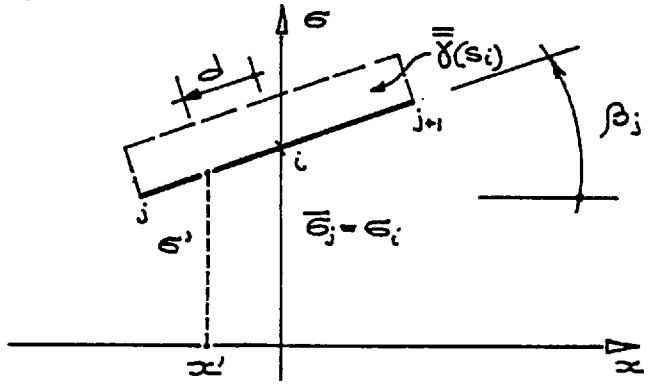

Fig. 2.10

transformed to

$$\frac{k\,\bar{\bar{\gamma}}(s_i)}{4\pi}\left\{\cos\beta_i \int_{s_j}^{s_{j+1}} v(x_i,\sigma_j;x',\sigma')\,ds - \sin\beta_i \int_{s_j}^{s_{j+1}} u(x_i,\sigma_j;x',\sigma')\,ds\right\} = \bar{\bar{C}}_{ij} \tag{80}$$

When $(x',\sigma') = (x_i,\sigma_i)$ the two integrals

$$U_i = \int_{s_j}^{s_{j+1}} u\,ds \qquad V_i = \int_{s_j}^{s_{j+1}} v\,ds \tag{81 a, b}$$

are improper. Equations (2.3.63) and (2.3.64) show that the singularity of the integrands is of order $o(\eta^{-1})$ where $\eta = d = [(x'-x_i)^2 + (\sigma'-\sigma_i)^2]^{1/2} / \sigma_i$ The way to overcome this difficulty is to substitute (63) and (64) into equation (81) and then integrate term by term. If the limits of integration are symmetric with respect to $\eta = 0$ all the contributions from odd powers of η are dropped. Then, if the point $P = (x,\sigma)$ and P_i are assumed to be the same point $\tilde{P} \equiv (0,\sigma_i)$ and θ is taken equal to β_i as shown in Fig. (2.10), explicitly we have

$$U_i = \frac{1}{\sigma_i}\int_{-\eta_0}^{\eta_0}\left\{\frac{1}{2}\ln\frac{64}{\eta^2}\left[1-\frac{\sin\beta_i}{4}\eta+\frac{(4\sin^2\beta_i-3)}{16}\eta^2\right]+\left[\frac{2\sin\beta_i}{\eta}-\cos^2\beta_i-\frac{\sin\beta_i(2\sin^2\beta_i-5)}{8}\eta+\frac{2\sin^4\beta_i-9\sin^2\beta_i+4}{16}\eta^2\right]\right\}d\eta \quad (82)$$

where $\eta_0 = [(x_j-x_i)^2+(\sigma_j-\sigma_i)^2]^{1/2}/\sigma_i$ and similarly for V_i. Solving the integrals we eventually obtain

$$U_i = \eta_0\left\{\left[1+\frac{1}{48}(4\sin^2\beta_i-3)\eta_0^2\right]\ln\frac{64}{\eta_0^2}+\left[2\sin^2\beta_i+\frac{1}{72}(9-23\sin^2\beta_i+6\sin^4\beta_i)\eta_0^2\right]+O(\eta_0^4)\right. \quad (83)$$

$$V_i = -\sin\beta_i\cos\beta_i\,\eta_0\left\{\frac{\eta_0^2}{8}\ln\frac{64}{\eta_0^2}+\left[2-\frac{\eta_0^2}{24}(9-2\sin^2\beta_i)\right]\right\}+O(\eta_0^4) \quad (84)$$

These expansions provide a good approximation for $\eta_0 \ll .1$

Substituting equations (83) and (84) into equation (80) we obtain the second part of the matrix

$$\bar{\bar{C}}_{1_i} = \sum_{1}^{N}{}_j\,\frac{\delta_{i,j}\,\bar{\bar{\gamma}}(s_j)}{4\pi}\,R\left[\cos\beta_j V_j - \sin\beta_j U_j\right] = \sum_{1}^{N}{}_j\,\frac{\bar{\bar{\gamma}}(s_j)}{4\pi}\,\delta_{i,j}\,f_j \quad (85)$$

Also, because of the linear dependence of $\bar{\bar{\gamma}}(s)$ on s

$$\frac{\bar{\bar{\gamma}}(s_i)}{4\pi} = \frac{\Gamma_{i-1}}{s_{i+1}-s_{i-1}} + \frac{\Gamma_i}{s_{i+2}-s_i} \quad (86)$$

then equation (85) can be organised as

$$\bar{\bar{C}}_{1_i} = \sum_{1}^{N}{}_j\,A^{(2)}_{i,j}\,\Gamma_{j-1} + A^{(3)}_{i,j}\,\Gamma_j \quad (87)$$

where

$$A^{(2)}_{i,j} = \frac{\delta_{i,j}\,f_j}{s_{i+1}-s_{i-1}} \qquad A^{(3)}_{i,j} = \frac{\delta_{i,j}\,f_j}{s_{i+2}-s_i} \quad (88\ a,\ b)$$

Then the matrix form of equation (67) is

$$\sum_{1}^{N}{}_{j}\left[A^{(1)}_{i,j}\Gamma_j + A^{(2)}_{i,j}\Gamma_{j-1} + A^{(3)}_{i,j}\Gamma_j\right] = \mathcal{C}_i \qquad i=1,2,\ldots,N \tag{89}$$

or

$$\mathbb{A}\,\Gamma = \mathcal{C} \tag{90}$$

which has the solution

$$\Gamma = \mathbb{A}^{-1}\,\mathcal{C} \tag{91}$$

Note that if the boundaries are fixed in time $\mathbb{A}$ and hence $\mathbb{A}^{-1}$ depends only upon the geometry of the problem, then it can be stored and used every time step. Once we know the value of $\mathcal{C}_i$ at each mid-point, we obtain Γ_j by a simple matrix multiplication.

The tangential velocity $\underline{V}_t = \underline{V}\cdot\hat{\underline{t}}$ at the boundary can be obtained by the same method. Using equations (74), (76) and (77), we have

$$V_{t_i} = \sum_{1}^{N}{}_{j}\left[V_{i,j}\sin\beta_i + U_{i,j}\cos\beta_i\right]\Gamma_j \qquad i=1,2,\ldots,N \tag{92}$$

Then the principal value contribution can be obtained by equations (83), (84).

$$V^{(1)}_{t_i} = \sum_{1}^{N}{}_{j}\frac{\delta_{i,j}\,\bar{\bar{\gamma}}(s_j)}{4\pi}\left[V_j\sin\beta_j + U_j\cos\beta_j\right] = \tag{93}$$

$$= \sum_{1}^{N}{}_{j}\frac{\bar{\bar{\gamma}}(s_j)}{4\pi}\delta_{i,j}\bar{f}_j$$

The analysis in section (2.1) shows that we must add to the tangential velocity a contribution due to the local surface distribution of vorticity.

$$V^{(3)}_{t_i} = \bar{\bar{\gamma}}(s_i)/2 \tag{94}$$

Then, if the equation (86) is substituted into equations (83) and (84) and combined with equation (82)

$$V_{t_i} = \sum_{1}^{N}{}_j \left\{ \left(V_{i,j} \sin\beta_i + U_{i,j} \cos\beta_i \right) T_j + \right.$$
$$\left. + \delta_{i,j} \left(\frac{T_{j-1}}{s_{j+1} - s_{j-1}} + \frac{T_j}{s_{j+2} - s_j} \right) \left(\bar{f}_j + 2\pi \right) \right\} + \tag{95}$$
$$+ \left(\underline{V}_\infty \cdot \hat{\underline{t}} \right)_i + \left(\underline{V}_v \cdot \hat{\underline{t}} \right)_i \qquad i = 1, 2, \ldots, N$$

In matrix notation and using equation (91)

$$\mathbb{V}_t = \mathbb{B}\mathbb{A}^{-1}\mathbb{G} + \mathbb{V}_{\infty t} + \mathbb{V}_{vt} \tag{96}$$

Again the matrix $\mathbb{B}\mathbb{A}^{-1}$ depends only upon the geometry of the boundary.

If a thin wall, sharp edge is present on the boundary, we must take care of the occurrence of a singularity of order $O(d^{-1/2})$. We assume that on the element $(N_f, N_f{-}1)$ the strength of the vorticity distribution is

$$\bar{\bar{\gamma}}(s) = \left(\sqrt{\frac{\Delta}{d}} - \frac{d}{\Delta} \right) \bar{\gamma}_{N_f} + \frac{d}{\Delta} \bar{\gamma}_{N_f - 1} \tag{97}$$

$$4\pi T_N = \int_0^{\Delta} \left(\sqrt{\frac{\Delta}{d'}} - \frac{d'}{\Delta} \right) \bar{\gamma}_{N_f} \, d(d') = \frac{3}{2} \Delta s_{N_f - 1} \bar{\gamma}_{N_f} \tag{98}$$

Fig. 2.11

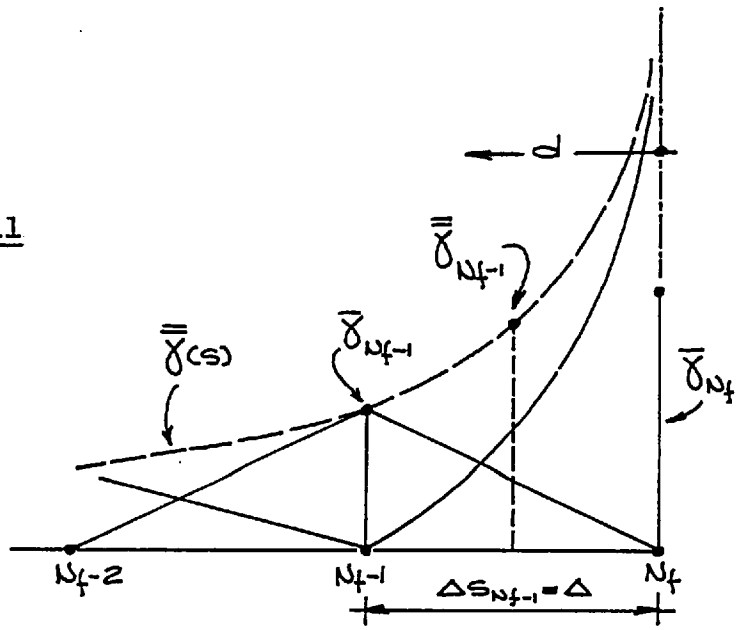

$$\bar{\gamma}_{N_f} = 4\pi \frac{2\Gamma_{N_f}}{3\Delta s_{N_f-1}}$$

$$\bar{\gamma}_{N_f-1} = 4\pi \frac{2\Gamma_{N_f-1}}{\Delta s_{N_f-2}} \qquad (99)\ a, b$$

Then applying equation (97)

$$\frac{\bar{\bar{\gamma}}_{N_f-1}}{4\pi} = \frac{\Gamma_{N_f-1}}{\Delta s_{N_f-2}} + .61 \frac{\Gamma_{N_f}}{\Delta s_{N_f-1}} \qquad (100)$$

This must be used instead of equation (86). This highly simplified way of representing the singularity of the edge is valid only if a proper distribution of elements near the edge is used as discussed in section (2.3)

Chaplin (1964) suggested that the normal velocity check-point should be taken at P_{N_f} and assumed it to be an interior point of the boundary. This leads to a more accurate evaluation of the singularity which is also fairly independent of the distribution of the elements near the edge. In this case the evaluation of equation (67) at the edge is different. Equation (79) applies only for $i = 1, 2, \ldots, N_f-1, N_f+1, \ldots, N$ and the contributions of the N_f^{th} vortex ring is dropped. Then the principal value contribution is added.

Assuming $\bar{\bar{\gamma}}(s)$ as given in equation (97), the integrals (81a, b) become

$$(U_{N_f}, V_{N_f}) = \int_{S_{N_f}}^{S_{N_f-1}} \bar{\bar{\gamma}}(s)(u,v)\,ds \qquad (101)$$

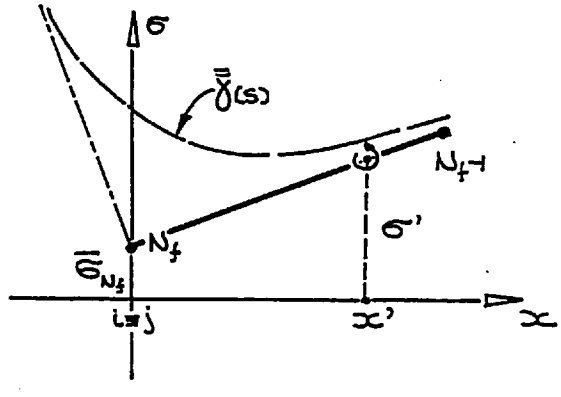

Fig. 2.12

Again, this is improper and can be evaluated by means of equations (63) and (64). However, in this case the limits of integration are not symmetric with respect to $\eta = 0$ and we have contributions from all of the powers of η. All terms are readily evaluated except for the one accounting for the edge singular behaviour

$$\sqrt{\eta_0} \int_0^{\eta_0} \frac{d\eta}{\eta\sqrt{\eta}} \tag{102}$$

This has been evaluated by Chaplin (1964) as

$$\lim_{\varepsilon \to 0} \int_0^{\eta_0} \frac{\sqrt{\eta_0}\, d\eta}{(\eta - \varepsilon)\sqrt{\eta}} = -2 \tag{103}$$

The results are

$$U_{N_f} = U^{(1)}_{N_f} \bar{\gamma}_{N_f} + U^{(2)}_{N_f} \bar{\gamma}_{N_f - 1} \tag{104}$$

where, with $\alpha = \beta_{N_f - 1}$

$$U^{(1)}_{N_f} = \left\{ \left[1 - \frac{\sin\alpha}{18} \eta_0 \right] \frac{3}{8} \eta_0 \ln \frac{64}{\eta_0^2} + \right.$$
$$\left. - \left[3\sin\alpha - \frac{3}{8}(1 + \sin^2\alpha)\eta_0 + \frac{\sin\alpha}{48}(2\sin^2\alpha - 3)\eta_0 \right] \right\} + O(\eta_0^3) \tag{105}$$

$$U^{(2)}_{N_f} = \left\{ -\frac{\sin\alpha}{48} \eta_0^2 \ln \frac{64}{\eta_0^2} + \right.$$
$$\left. + \left[\sin\alpha + \frac{1}{2}(1 + \sin^2\alpha)\eta_0 - \frac{\sin\alpha}{72}\left(6\sin^2\alpha - 13\right)\eta_0^2 \right] \right\} + O(\eta_0^3) \tag{106}$$

and

$$V_{N_f} = V^{(1)}_{N_f} + V^{(2)}_{N_f} \tag{107}$$

where

$$V_{N_f} = \left\{ \frac{\cos\alpha}{16} \eta_0^2 \ln \frac{64}{\eta_0^2} + \right.$$
$$\left. + \left[3 - \frac{3}{4}\sin\alpha\, \eta_0 - \frac{1}{48}\left(2\sin^2\alpha - 1\right)\eta_0^2 \right] \right\} + O(\eta_0^3) \tag{108}$$

$$V_{N_t}^{(2)} = \left\{ \frac{\cos\alpha}{16}\eta_0^2 \ln\frac{64}{\eta_0^2} + - \left[1 + \frac{\sin\alpha}{4}\eta_0 - \frac{1}{48}(2\sin^2\alpha - 3)\eta_0^2 \right] \right\} + O(\eta_0^3) \tag{109}$$

Equations (104) and (107) are then used in equation (93) and we proceed as before.

Care must be taken in applying this representation of the edge singularity. It can lead, depending on the geometry of the problem, to an ill-conditioned system of equations. This is a pathological feature of Fredholm's equation of the first kind whose discretization never leads to a diagonally dominated system of equations. However, the first way to represent the edge singularity always leads to a solution even if the solution is not always good and it depends on the distribution of elements.

We assume that if an element starts (or ends) on the x-axis, its end point is a check point. Also, the strength $\bar{\bar{\gamma}}(s)$ goes linearly to zero at such a point

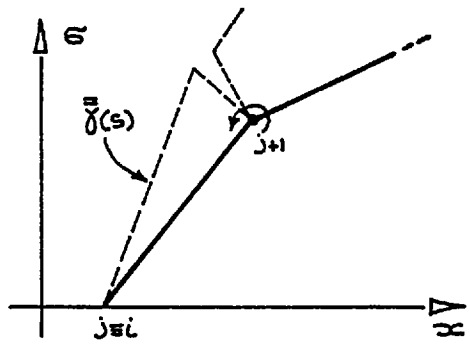

Fig. 2.13

2.7 Some calculated examples

In this section we apply the previous section's method to some examples of potential flows round axisymmetric bodies for which exact analytic solutions are known. A uniform stream is assumed to exist at infinity, then the surface velocity distribution is calculated.

Fig. (2.14) shows the results for a sphere of unit

radius and for an oblate spheroid of thickness ratio 8 and unit minor axis. They are compared with results obtained analytically and by applying Hess & Smith as described in section (2.2). The body surface has been described by 60 elements and the agreement is good.

In Fig. (2.14) a calculation, obtained without including the contribution from equation (93), is also shown. This shows that the contribution of the integral principal value is not of primary importance when the number of elements present is large. Indeed, if we assume $\bar{\eta} = MAX\{\eta_0^{(i)}; i=1,\dots,N\}$ where $\eta_0^{(i)}$ has been defined in section 2.6, we can see from equation (83) and (84) that such a contribution if of order $O(\bar{\eta}\ln\bar{\eta})$ as $\bar{\eta} \to 0$. Given a fixed length of boundary $\bar{\eta}$ decreases as the number of elements used increases.

The case of a disc as the extreme members of the oblate spheroids family $(e=1)$ is a good example of what we have called a thin-wall' boundary. The radial velocity at the surface of the disc is

$$\frac{V_t}{V_\infty} = \pm \frac{2U\sigma}{\pi R}\left[1-\left(\frac{\sigma}{R}\right)^2\right]^{-1/2} \qquad (110)$$

where the "+" sign refers to the wetted surface. Assuming $R=1$ the velocity has a singularity at the edge of $O[(1-\sigma)^{-1/2}]$ as $\sigma \to 1$ and this must be solved as shown in section (2.6). As before results are presented in Fig. (2.15) for the vortex method with and without the integral principal value contributuion. The disc was simulated by 36 similar elements. The agreement with the

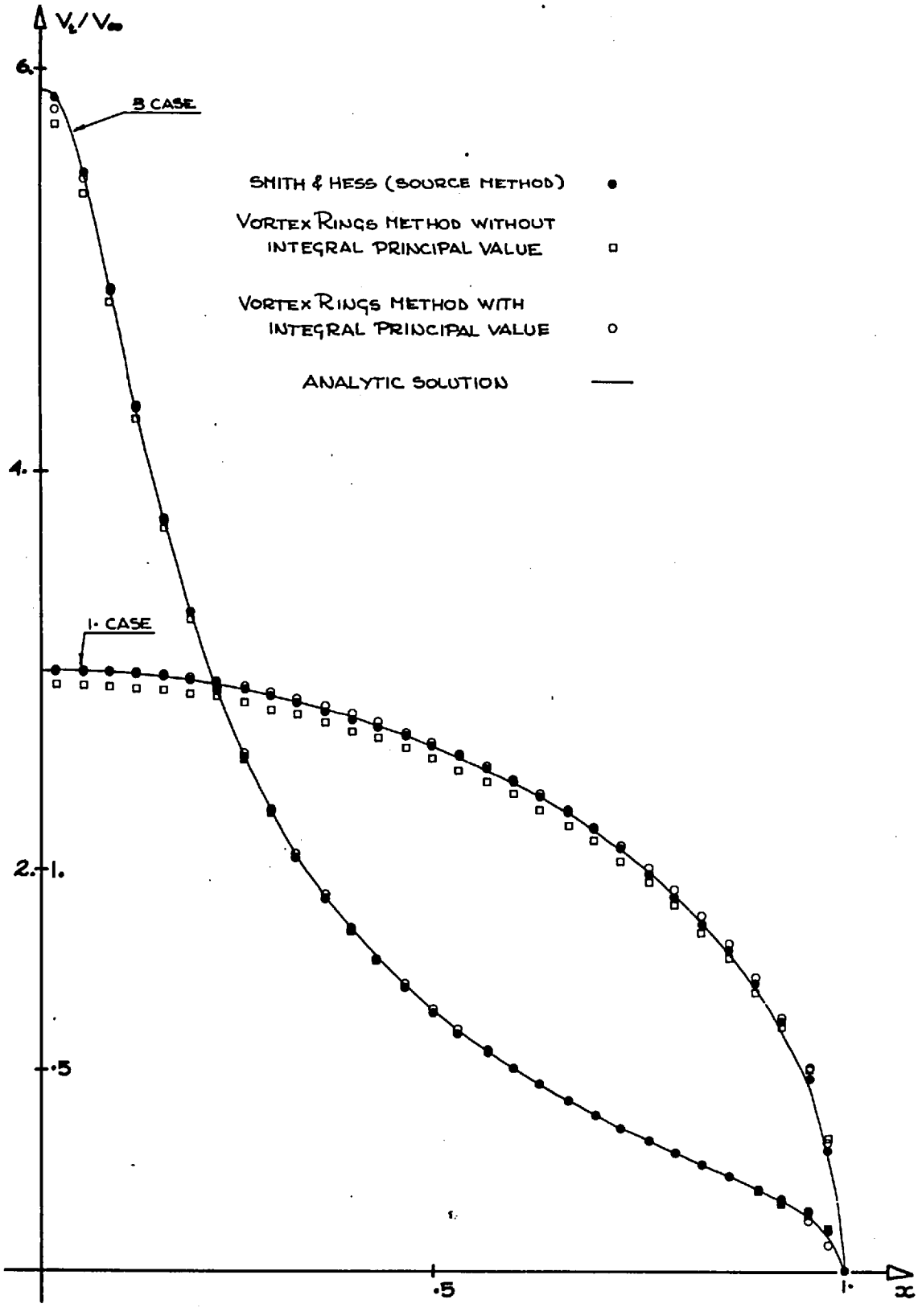
V_t/V_∞
6.
4.
2.
1.
.5
5 CASE
1· CASE
SMITH & HESS (SOURCE METHOD)
VORTEX RINGS METHOD WITHOUT INTEGRAL PRINCIPAL VALUE
VORTEX RINGS METHOD WITH INTEGRAL PRINCIPAL VALUE
ANALYTIC SOLUTION
.5
1·
x

Fig. 2.14

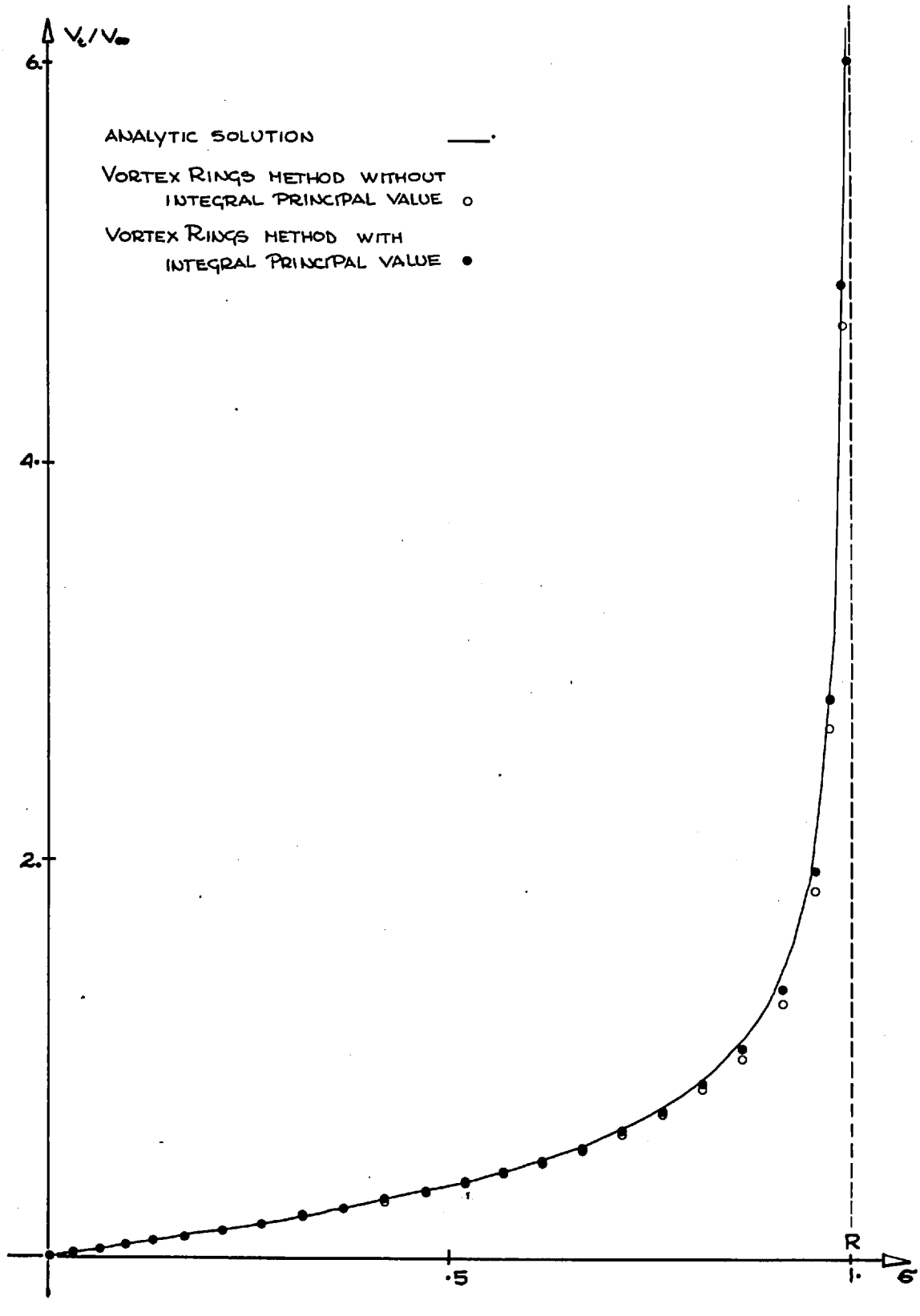
V_t/V_∞
6.
4.
2.
ANALYTIC SOLUTION
VORTEX RINGS METHOD WITHOUT INTEGRAL PRINCIPAL VALUE o
VORTEX RINGS METHOD WITH INTEGRAL PRINCIPAL VALUE •
.5
1.
R
6

Fig. 2.15

analytic solution is quite good in spite of the presence of the singularity. As before the contribution of equation (93) does not make much differences. However, the singular behaviour near the edge is better calculated by the full vortex rings method.

In conclusion the method presented in the previous sections for calculating axisymmetric potential flows appears fully satisfactory for our purposes, particularly because of its ability to represent sharp edge singularities and 'thin-walls' and also it is the most convenient because of its simplicity.

3. SEPARATED AXISYMMETRIC FLOW

3.1 Introduction

The presence in the boundaries of a geometrical singularity or a region of high curvature relative to the local boundary layer thickness is a common reason for flow separation and for the formation of a free shear layer of thickness comparable to that of the boundary layer. Although the viscosity of the fluid is essential for this formation process we expect that it has little or no effect on the evolution of the shear layer, mainly acting through the Kutta-Joukowski condition which removes the singular behaviour of the velocity at the edge. So, assuming that a consistent limit for the kinematic viscosity $\nu \to 0$ exists, a bound vortex sheet is present on the boundary and is shed at the separation point as a free vortex sheet which is convected away with the local velocity. The properties

of the free vortex sheet at the edge are uniquely described by the Kutta-Jcukowski condition which requires the velocity to be finite at the edge.

The vortex sheet extending downstream generally rolls up into a continuously tightening spiral that asymptotically becomes a circular vortex whose core vorticity distribution is singular but integrable (Saffman & Baker, 1979). This process can be highly modified by the presence of boundaries and vortices produced by rolling up of previously generated vortex sheets and its computation still remains a challenging problem.

3.2 Separation from a sharp edge

Prandtl (Smith, 1966) originally discovered the appropriate similarity løw for two dimensional (planar) starting flow around a wedge. Anton (1939) attempted a solution for the flat plate and he found that the total vorticity was proportional to $t^{1/3}$ and a characteristic length had to be constructed with $t^{2/3}$. In order to find the constants he approximated the inner part of the vortex sheet by a Kaden's spiral

$$r \propto (t/\theta)^{2/3} \qquad (1)$$

where r is the radius vector and θ is the turn angle, and joined it to the edge by an outer loop. The two parts were matched to have a common tangent and continuity of vorticity. For the shedding, the inner core was approximated by a single concentrated vortex point, and the Kutta condition was applied. The vortex sheet was convected by

the flow and the matching repeated by an iterative procedure.

Wedermayer (1961) and Blenderman (1969) generalised these results. Rott (1956) investigating the vortex generation due to a weak shock diffraction near on infinite edge, obtained a Brown & Michael's (1954) single-vortex solution for non-zero wedge angles and he also derived the asymptotic form for the rolled up spiral.

Moore & Saffmann (1973) found the leading order asymptotic shape of the spiral of the vortex sheet shed from a tip of a wedge of internal angle δ accelerating with velocity proportional to t^p. The shape of the spiral and the circulation around a circle of radius r are (Saffmann & Baker, 1979)

$$r \sim C(t/2\pi\theta)^m \tag{2}$$

$$\Gamma \sim C^{1/m} r^{2-1/m} \tag{3}$$

where

$$m = \lambda(1+p)/(2\lambda-1) \tag{4}$$

and $\lambda = 2-\delta/\pi$ as before and C is a dimensional constant determined by matching the outer flow.

Pullin (1978) by a highly stable calculation found that the sheet rolls up into a fairly circular spiral only for $\delta = 0$. However, for $\delta \neq 0$, elliptical distortion appears and becomes very pronounced as $\delta \to \pi$ and does not appear to decrease substantially over the inner part of the spiral.

Moore (1974) also found such an elliptical distortion in calculating the classical Kaden's problem of the evolution of an elliptically loaded vortex sheet.

In the case of axisymmetric flow the similarity law holds and also eqn. (1) seems to be valid at least for the case of zero wedge angle. Saffman made use of it to calculate the behaviour of a vortex ring produced by ejecting fluid through a circular nozzle. He noticed that for a short ejection time the characteristic length of the shedding is small compared to that of the singularity and the axisymmetric vortex sheet behaves like a 2-D one shed from a semi-infinite wedge (Saffman, 1978). He found reasonable agreement with experimental results by Guhler & Sellet (1979), Krutzsch (1939), Liess & Didden (1976), Maxworthy (1977) and Sellet & Widmayer (1974). However, Didden (1979) did not find such a similarity law and proposed that the horizontal displacement of the forming vortex ring should be proportional to $t^{3/2}$.

We assume that the vortex shedding in our axisymmetric problem is governed by the attached flow near the singularity in the boundary and the region of influence is small compared to the radius of the singularity so that we can take the shedding to be locally 2-D. We split the axisymmetric vortex sheet in two parts: a small bit, which is the object of this section, close to the edge and the remaining part, discussed in the following section, whose induced velocity field is assumed to be known and well behaved near the edge.

Graham (1977) has discussed 2-D vortex shedding from an infinite sharp edge in detail and this section follows his results closely.

The attached flow past an edge of internal angle δ can be described by the complex velocity

$$v(z) = v_x + i v_y = \frac{2U}{\lambda} z^{(2-\lambda)/\lambda} + i \frac{V}{\lambda} z^{(1-\lambda)/\lambda} \qquad (5)$$

where U and V are real constants describing the symmetrical and asymmetrical (relative to the median plane of the wedge) parts of the flow and $z = x + iy$ The part of the flow due to the asymmetric velocity V is singular at the edge and gives rise to the flow sparation.

Giesing (1969) has derived a relationship between V and the properties of the shed vortex sheet. He noticed that when the flow is unsteady proper dynamical and kinematic conditions have to be applied in order to apply the Kutta - Joukowski condition and to describe the vortex shedding. He assumes that the element of vortex sheet shed in a small time interval δt is straight, of length δs and uniform strength γ . On this the velocity field $v(z)$ is imposed (Fig. 3.1).

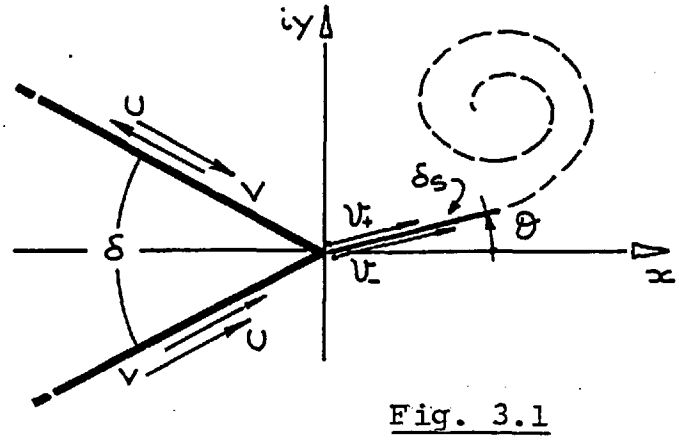

Fig. 3.1

Using (2.1.17) the modulus of the total velocity on the upper and lower surface of the sheet are

$$v_\pm^2 = \left(v_x \pm \frac{\gamma}{2}\cos\theta\right)^2 + \left(v_y \pm \frac{\gamma}{2}\sin\theta\right)^2 \qquad (6)$$

So, by applying Bernoulli's equation (2.1.9) we calculate the pressure drop across the sheet.

$$\Delta p = p_+ - p_- = \rho \frac{\partial}{\partial t}(\phi_- - \phi_+) + \rho(v_+ \cos\theta + v_y \sin\theta)\gamma \qquad (7)$$

Remembering that the total circulation of the vortex sheet is

$$\Gamma = \int_0^S \gamma \, ds = \oint_{\text{VORTEX SHEET}} v_\pm \, ds = \phi_- - \phi_+ = \Delta\phi \qquad (8)$$

where S is the total length of the vortex sheet and defining

$$Q_c = (v_x \cos\theta + v_y \sin\theta) \qquad (9)$$

The dynamical condition $\Delta p = 0$, which says that the vortex sheet has to be convected with the local velocity, becomes

$$Q_c \gamma = \frac{d\Gamma}{dt} \qquad (10)$$

If we apply the Kutta condition in the real plane, $v|_{x=y=0} = 0$ because $1 \le \lambda \le 2$, the convective velocity $Q_c \to 0$ as we move close to the edge. Therefore, because $d\Gamma/dt$ is finite, a singular behaviour occurs at the edge due to an infinite vorticity strength γ. We assume $Q_c \neq 0$ and transform the edge into a plane surface by the transformation $z = \zeta^\lambda$ An image system has to be introduced in the transformed plane to account for the presence of the wall.

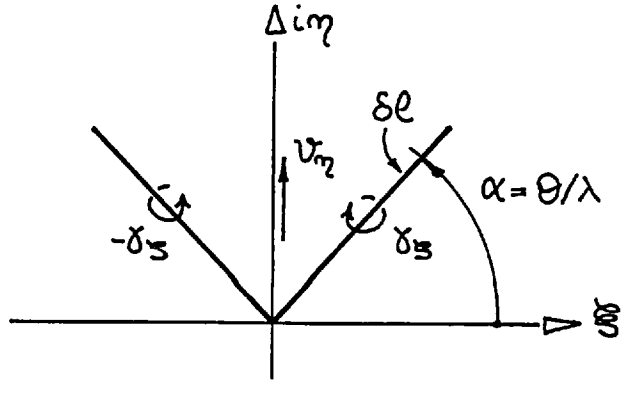

Fig. 3.2

Then the velocity v_η induced by the wall is

$$v_\eta = \int_0^{\delta\rho} \frac{d v_s}{d\rho'} \gamma_s \, d\rho' = \int_0^{\delta\rho'} \frac{\gamma\lambda \rho^{\lambda-1}}{2\pi} \left(\frac{e^{i\alpha}}{\rho + i\eta e^{i\alpha}} + \frac{e^{-i\alpha}}{\rho + i\eta e^{-i\alpha}} \right) d\rho =$$

$$= C_\Gamma \, Re \left\{ e^{i\alpha} \int_0^{\delta\rho} \frac{\rho^{\lambda-1}}{\rho + i\eta e^{i\alpha}} \, d\rho \right\} \tag{11}$$

where

$$C_\Gamma = -\frac{\lambda}{\pi Q_c} \frac{d\Gamma}{dt} \tag{12}$$

The integral can be evaluated in closed form only for particular values of λ and Geising considered the special case $\delta = \pi/2$ ($\lambda = 1.5$). So, after solving the integral and taking the limit for η small, the wall velocity is

$$\begin{cases} v_\eta = C_\Gamma \left[2\sqrt{\delta\rho} \cos\alpha - \pi |\eta|^{1/2} \cos(3\alpha/2 + b\pi) \right] \\ b = \begin{cases} 1/4 & \eta > 0 \\ 3/4 & \eta < 0 \end{cases} \end{cases} \tag{13 a, b, c}$$

For $\eta = 0$

$$v_\eta = 2 C_\Gamma \sqrt{d\rho} \cos\alpha \tag{14}$$

which must cancel the asymmetric velocity at the edge in the real plane. Therefore, applying eqns. (5), (12), (14) to the general case and transforming back, the Kutta-Joukowski condition is

$$V = \frac{\gamma\lambda \sin(\pi/\lambda)}{\pi(\lambda - 1)} (\delta s)^{(\lambda-1)/\lambda} \tag{15}$$

The second term of eqn. (13a) gives us additional information in the physical plane. Transforming it back and evaluating it on the wall near the edge gives

$$v^{(\pm)}_{WALL} - v_\eta \left|\frac{dS}{dz}\right|_{\xi=0} = -\gamma \cos(\theta + b\pi) \tag{16}$$

The difference of the velocity above and below the edge δv must be exactly the vorticity strength γ

$$\delta v = \gamma = \gamma\left[\cos(\theta + \pi/4) - \cos(\theta + 3\pi/4)\right]$$

Solving for α gives $\alpha = -\pi/4$ or in general

$$\theta = -\frac{\delta}{2}\frac{\gamma}{|\gamma|} \tag{17}$$

which says that the vortex sheet leaves the wetted surface tangentially.

The convective velocity off the edge is then given by the symmetric attached flow and the contribution of the vortex sheet itself in the limit of zero vortex sheet length

$$Q_c = \lim_{\delta s \to 0}\left[(v_w^+ + v_w^-)/2 + v_\infty|_{WALL}\right] \tag{18}$$

hence

$$Q_c = \frac{\gamma}{2} + \begin{cases} 0 & \delta > 0 \\ Q_u & \delta = 0 \end{cases} \tag{19 a, b}$$

It is not immediately clear how the extra contribution to the convective velocity Q_u appears when $\lambda \to 2$ and no stagnation point needs to exist on the unwetted side of the edge. Graham (1977) noticed that a small distance r off the edge U must always control the convection velocity $Q_c(r)$. Then when r is arbitrarily small he has shown that

$$Q_c(r) = \gamma/2 + (U - \gamma/2)\, r^{(2-\lambda)/\lambda} + O(2-\lambda) \tag{20}$$

However, experimental (Fage & Johansen, 1927) and computed (Graham, 1977) results indicated that the velocity on the unwetted side of a flat plate is generally small. That is,

U is only slightly greater than $\gamma/2$ and consequently it can be assumed empirically but not with certainty for axisymmetric flow that

$$Q_c - \gamma/2 = (v_w^+ + v_w^-)/2 \tag{21}$$

Then, for a small but finite time δt

$$\frac{\delta s}{\delta t} = \frac{\gamma}{2} \tag{22}$$

The total circulation $\delta\Gamma$ of the element shed in time δt is by equation (10) and (22)

$$\delta\Gamma = 2\,\delta s^2/\delta t \tag{23}$$

Combining equations (15) and (22) it follows that

$$\delta s = C\,L_v \tag{24}$$

where C depends only upon the wedge angle δ

$$C = \left[\frac{\pi(\lambda-1)}{2\lambda \sin(\pi/\lambda)}\right]^{\lambda/(2\lambda-1)} \tag{25}$$

and L_v is a characteristic length associated with the asymmetric part of the attached flow past the edge

$$L_v = (\nu\,\delta t)^{\lambda/(2\lambda-1)} \tag{26}$$

When the fluid has just been set into motion, the vortex sheet appears at the edge and starts rolling up at its free end into a tight spiral. It behaves like a two-dimensional vortex sheet. This can be represented by a single point vortex collocated at the centre of the growing spiral z_o joined to the edge at z_e by a cut representing the sheet.

This simplified model, first suggested by Brown & Michael (1954), has been extensively discussed by Graham (1977). Using the previously described transformation $Z = \zeta^{\lambda}$ the Kutta-Joukowski condition in the transformed plane becomes

$$V = \frac{\Gamma}{2\pi} \frac{Z_o^{1/\lambda} + \bar{Z}_o^{1/\lambda}}{Z_o^{1/\lambda} \bar{Z}_o^{1/\lambda}} \tag{27}$$

In the present case where the whole vortex sheet is represented by a single point vortex of strength γ the dynamical condition $\Delta p = 0$ can be conveniently substituted by the simpler condition of zero total force on the vortex plus cut

$$\underline{F} = \int_{CUT} \Delta p \, d\underline{s} = 0 \tag{28}$$

Combining equations (7), (8) and (28) and considering for simplicity the y component of the total force

$$F_y = \int_{CUT} \Delta p \, dx = \rho \frac{\partial}{\partial t} \int_{CUT} (\phi_+ - \phi_-) dx + \rho \int_{CUT} v_x \gamma \, ds = 0 \tag{29}$$

A more general result can be obtained if the cut is generally assumed to be a vortex sheet of length $\delta s = s_o - s_e$ of strength $\gamma(s)$

$$\underbrace{\int_{s_e}^{s_o} \left[-\int_{s_o}^{s} \gamma \, ds \right] dx}_{(i)} + \underbrace{\int_{s_e}^{s_o} v_x \gamma \, ds}_{(ii)} = 0 \tag{30}$$

Solving the integral (i) by parts

$$\int_{s_e}^{s_o} \left[\int_{s_o}^{s} \gamma \, ds \right] dx = \left[x \int_{s_o}^{s} \gamma \, ds \right]_{s_e}^{s_o} - \int_{s_e}^{s_o} x \gamma \, ds$$

$$= x_e \Gamma - \int_{s_e}^{s_o} x \gamma \, ds \tag{31}$$

Let $Z = (X \; Y)$ be the centroid of vorticity of the sheet

$$\Gamma X = \int_{s_o}^{s_e} x\gamma\, ds \tag{32}$$

Expanding $v_x = v_{x_o} + v_{x_1} x + \cdots$ the integral can be solved

$$\int_{s_e}^{s_o} \gamma v_x ds = v_{x_o}\Gamma + v_{x_1}\int_{s_e}^{s_o} x\gamma\, ds + \cdots = v_{x_o}\Gamma + v_{x_1} X\Gamma =$$

$$= (v_{x_o} + v_{x_1} X)\Gamma + \cdots = \bar{v}_x \Gamma \tag{33}$$

where $\bar{v}_x$ is the mean velocity in the x direction experienced by the whole sheet. Therefore the condition $F_y = 0$ shows

$$\frac{\partial}{\partial t}\left[\Gamma(X - x_e)\right] + \bar{v}_x \Gamma = 0 \tag{34}$$

A similar relation can then be obtained from the condition $F_x = 0$ or in general

$$\frac{\partial}{\partial t}\left[(Z - z_e)\Gamma\right] + \Gamma \left.\frac{\partial \bar{w}}{\partial z}\right|_{z=Z} = 0 \tag{35}$$

where $\partial w/\partial z = v_x - i v_y$ This results assumes that the sheet is approximately aligned with the free stream direction which is only a reasonable approximation for the starting sheet.

In the case of Brown & Michael's model the centroid of vorticity is at the point vortex position, then equation (35) becomes

$$\frac{\partial}{\partial t}\left[(z_o - z_e)\Gamma_o\right] + \Gamma_o \left[\frac{\partial \bar{w}}{\partial z}\right]_{z=z_o} = 0 \tag{36}$$

Graham applied the equation (36) with $z_e=0$ and calculated the position z_o and the strength of the growing vortex for an attached flow with $U=0$, $V=Vt^b$

$$z_o = K^{\lambda/(2\lambda-1)} L_v e^{i\theta} \tag{37}$$

$$\Gamma_o = \frac{2\pi K^{1/(2\lambda-1)} L_v^2}{\sqrt{\lambda}\,\delta t} \tag{38}$$

where

$$K = \frac{\sqrt{4-\lambda}\,(\lambda-1)(2\lambda-1)}{2\lambda^2(3b\lambda+\lambda+1)} \tag{39}$$

and

$$\theta = -\lambda \cos^{-1}(\sqrt{\lambda}/2) \tag{40}$$

Finally, we can obtain an estimate of the inner core size c_o assuming a Kaden's type spiral and applying equations (2), (3) and (4)

$$c_o = \mathcal{C}_c L_v \tag{41}$$

where

$$\mathcal{C}_c = \left[\frac{1.9\, K^{1/(2\lambda-1)}}{\sqrt{\lambda}}\right]^{\lambda} \tag{42}$$

3.3 Vortex ring formation

Recently Saffman (1978) discussed the process of ring formation at sharp-edged tube and orifice openings utilising a two-dimensional similarity theory. Pullin (1979) extended his model to properly account for the axisymmetric geometry.

Vortex rings are commonly produced by ejecting fluid through an opening of diameter D by means of an impulsively

started piston of diameter Dp. The flow separates at the sharp edge and when the piston is stopped the vortex sheet breaks away from the orifice edge to form a vortex ring which is convected downstream by its self-induced velocity. We ignore vorticity of opposite sign generated by the stopping of the piston. The piston moves through a short distance

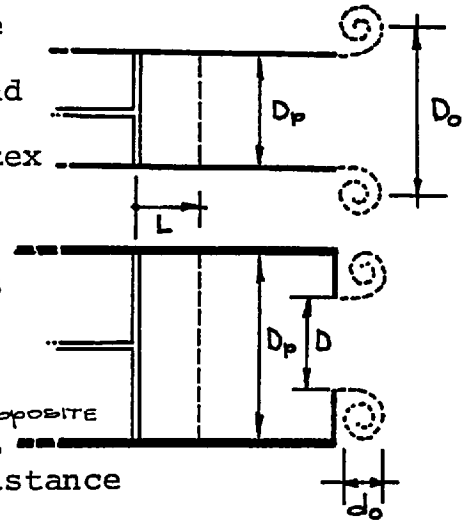

Fig. 3.3

$$L = \int_0^T V(t)\,dt \tag{43}$$

where

$$V(t) = V_0 t^b$$

The velocity potential of an attached flow around a sharp edge is given in polar co-ordinates (ρ,θ)

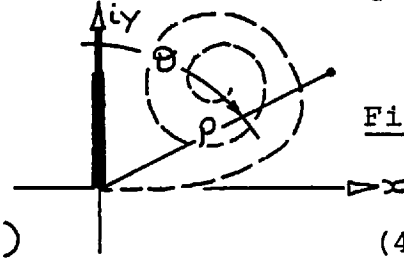

Fig. 3.4

$$\phi = -\alpha t^b \rho^{1/2} \cos(\theta/2) \tag{44}$$

where $\rho^2 = x^2 + y^2$ and α is determined by matching to the flow far from the edge

$$\alpha = C_\alpha V_0 D^{1/2} \tag{45}$$

For flow through a circular orifice in an infinite plane the normal velocity at the orifice is given by Lamb (1932, p.144)

$$V_x\big|_{\theta=\pi} = \frac{Q}{\pi D^{3/2} r^{1/2}} \tag{46}$$

where Q is the flux through the hole

$$Q = V(t)\pi D_p^2/4 \tag{47}$$

By comparing this with $\frac{1}{r}\frac{\partial\phi}{\partial\theta}\Big|_{\theta=\pi}$, an estimate of α can be obtained

$$\alpha = \frac{2Q}{\pi D^{3/2}} \tag{48}$$

and then

$$C_\alpha = .5(D_p/D)^2 \tag{49}$$

Pullin (1979) gives the approximate solution for the tube case Dp=D

$$C_\alpha = (2\pi)^{-1/2} \tag{50}$$

Then for small times, the vortex sheet depends on α and t only. When $b=0$ its centre (x_0, y_0), the circulation $\Gamma_0(\rho)$ about a small circle centred on the vortex of the spiral, and the total circulation Γ_0 shed from the edge are given by

$$x_0 = C_1(\alpha T)^{2/3} \qquad y_0 = C_2(\alpha T)^{2/3} \tag{51 a,b}$$

$$\Gamma_0(\rho) = C_3 \alpha \rho^{1/2} \qquad \Gamma_0 = C_4 \alpha^{4/3} T^{1/3} \tag{51 c,d}$$

An estimate of the constants can be obtained from Pullin's (1978) calculations as

$$C_1' = .34 \quad C_2' = .08 \quad C_3' = 4.08 \quad C_4' = 2.4 \tag{52 a,b,c,d}$$

Saffman (1978) matched the edge solution with the flow through a two-dimensional channel of width D then

$$C_\alpha = (\pi)^{-1/2} \tag{53}$$

He obtained an estimate for the constant from Anton (1939)

and Wedermayer's (1961) calculations

$$\mathbb{C}_1^2 = \cdot 3 \quad \mathbb{C}_2^2 = \cdot 09 \quad \mathbb{C}_3^2 = 3\cdot 3 \quad \mathbb{C}_4^2 = 2\cdot 5 \tag{54}$$

Combining equations (51c) and (51d), we have an estimate for the core size

$$c_o = (\mathbb{C}_4/\mathbb{C}_3)(\alpha T)^{2/3} = \mathbb{C}_5(\alpha T)^{2/3} \tag{55}$$

The constant $\mathbb{C}_5$ can be evaluated $\mathbb{C}_5^1 = \cdot 35$ and $\mathbb{C}_5^2 = \cdot 57$ (56 a,b)

Pullin (1979) gives two more general relations for total circulation and the core size

$$\Gamma_o = 2\cdot 4 \frac{\alpha^{4/3} T^{\frac{4}{3}(1+b)-1}}{(1-b)^{1/3}} = \mathbb{C}_4^3(b)\alpha^{4/3} T^{\frac{4}{3}(1+b)-1} \tag{57}$$

$$c_o = \cdot 33 \frac{\alpha^{2/3} T^{\frac{2}{3}(1+b)}}{(1+b)^{2/3}} = \mathbb{C}_5^3(b)\alpha^{2/3} T^{\frac{2}{3}(1+b)} \tag{58}$$

In the same condition , $\lambda = 2$, equations (38) and (41) give slightly different results

$$\Gamma_o = 2\cdot 49 \frac{\alpha^{4/3} T^{\frac{4}{3}(1+b)-1}}{(2b+1)^{1/3}} = \mathbb{C}_4^4(b)\alpha^{4/3} T^{\frac{4}{3}(1+b)-1} \tag{59}$$

$$c_o = \cdot 57 \frac{\alpha^{2/3} T^{\frac{2}{3}(1+b)}}{(2b+1)^{2/3}} = \mathbb{C}_5^4(b)\alpha^{2/3} T^{\frac{2}{3}(1+b)} \tag{60}$$

With $b=0$ the constant $\mathbb{C}_4^3(0)$ and $\mathbb{C}_5^3(0)$ are very close to the estimates (52), whereas the constants $\mathbb{C}_4^4(0)$ and $\mathbb{C}_5^4(0)$ get values close to Saffman's prediction. This shows that the predictions of Brown & Michael's simpler single vortex model are comparable to those of more sophisticated approaches.

3.4 Vortex sheet evolution

Numerical representations of a continuous vortex sheet has been offered since 1932 when Rosenhead investigated the Helmholtz instability of a two-dimensional vortex sheet by an equivalent distribution of discrete vortices. Substantial reviews of the subject has been published by Clements & Maull (1975), Fink & Soh (1974) and recently by Saffman & Baker (1979).

The point vortex approximation can be interpreted as a trapezoidal quadrature scheme for the principal value integral of the non-linear integro-differential equation governing the vortex sheet motion, in which the vortices are markers for the position of the interval. Many calculations using different forms of discretization have been attempted but, in spite of its simplicity, the method was found to lead to a chaotic vortex motion.

Moore (1971) found a pathological behaviour in the response of a vortex sheet to small disturbances. Because the growth rate was found to be inversely proportional to the wave length of sinusoidal disturbances and because the discretization imposed a lower bound to such wavelength, he concluded that using more vortices could make the situation worse, not better. He (Moore & Griffith-Jones, 1974) also found that if stretching was present the method was more stable and in particular if the stretching was proportional to t^{-1} disturbances were damped.
But still within the rolling-up process, the vortices near the centre of the spiral rather than smoothly following

the expected path tended to orbit about themselves and this orbiting movement could propagate along the sheet.

Clements & Maull (1973) delayed such a disruption by using a time step comparable with the orbital period of neighbouring vortices. Moore (1974) succeeded in following the evolution of the vortex sheet also by a careful choice of the time steps but mainly by using a tip vortex that could grow by amalgamation. Maskew (1977) showed that the core of the spiral cannot in any way be represented accurately with a finite number of vortices.

Fink & Soh (1974) claimed that the point vortex representation of a 2-D vortex sheet produces a logarithmic error in the self-induced velocity field,unless the point vortex remains in the centre of the interval which it represents. Sarpkaya (1975) claims that this error is relatively unimportant compared to other errors inherent in the method.

Baker (1977) extended Fink & Soh's work by taking account of the sheet curvature and applied it to the evolution of a circular non-uniform vortex sheet without singular behaviour. He found that by increasing the number of vortices unrealistic features appeared in the solution.

Gerrard (1967), Clements (1973),Sarpkaya (1975), Kiya & Arie (1977), Evans & Bloor (1977) and Graham (1980) have applied discrete vortices models to problems involving periodic vortex shedding and even if these calculations produced clouds of vortices or ill-behaved

vortex sheets useful results could be obtained as well as reliable information about the evolution of the vorticity field. These results were frequently obtained by employing some empirical methods or, less artifically, by providing a fine balance between using a large number of vortices to represent the fine scale and a crude integration scheme to suppress the chaotic motion.

In spite of the many disadvantages the point vortex representation is still a powerful tool. It is the simplest form of discretization and therefore it minimises the computing time. The continuity of the pressure-field across the vortex sheet is easily satisfied by convecting the vortices in a Lagrangian fashion. Also, giving a good approximation of the velocity field far from each element, it describes the general behaviours of the velocity field.

Thus, we look at the representation of an axisymmetric vortex sheet by a discrete distribution of elementary vortex rings. Each vortex has an infinitesimally small core with fixed circulation $\Gamma_m = \bar{\gamma}(t)\,\delta s(t)$ and its position is taken to be at the centre of the discretisation interval of length $\delta s = 2s_0$. A basic difference between the behaviour of the 2-D and the axisymmetric vortex sheet is an additional contribution to the self-induced velocity arising from the circular symmetry. This can be interpreted as a net contribution to the quadrature scheme for the principal value integral

$$\underline{u}(\underline{x},\bar{\sigma}) = \frac{1}{4\pi} \int_{\infty}^{\infty} \underline{G}_1(x,\sigma;x',\sigma')\,\gamma(s')\,ds' \qquad (61)$$

where $G_1 = [u(x,\sigma;x',\sigma');v(x,\sigma;x',\sigma')]$ is given by equations (2.3.32) (2.3.33). We have shown in section (2.3) that if $\eta = [(\bar{x}-x')^2+(\bar{y}-y')^2]^{1/2}/\bar{\sigma}$ the Green's function $|G_1|$ is of order $O(\eta^{-1})$ as $\eta \to 0$. Then the net self-induced velocity contribution is given by

$$\underline{u}^*(\bar{x},\bar{\sigma}) = \int_{-s_0}^{s_0} \gamma(\sigma')\, G_1\, d\sigma' = \underline{u}(\bar{x},\bar{\sigma}) - \int_{-\infty}^{s_0} \gamma(s')\, G_1\, ds' - \int_{s_0}^{\infty} \gamma(s')\, G_1\, ds' \tag{62}$$

The LHS integral has been already evaluated in section (2.6) and the results are presented in equations (2.6.83) (2.6.84) At the leading order

$$U^*(\eta_0,\alpha) = \frac{\bar{\gamma}}{4\pi}\eta_0\left[\ln\frac{64}{\eta_0^2} + 2\sin^2\alpha\right] + O(\eta_0^2) \tag{63}$$

$$V^*(\eta_0,\alpha) = -\frac{\bar{\gamma}}{4\pi} 2\sin\alpha\cos\alpha\,\eta_0 + O(\eta_0) \tag{64}$$

We note that if a vortex sheet of defined strength $\gamma(s)$ is represented by a sequence of conical elements of locally uniform strength, the self-induced velocity of each element decreases as $\eta_0 \ln \eta_0$ as the number of elements is increased, thus decreasing η_0

In the point vortex method each element of vortex sheet is approximated by a vortex ring of infinitesimally small core. Theoretically, the self-induced velocity of an Helmholtz vortex ring

$$U^* = \frac{\Gamma_m}{4\pi\bar{\sigma}}\left(\ln\frac{8\bar{\sigma}}{c_0} - .25\right) \tag{65}$$

increases weakly to infinity as its core radius c_0 decreases to zero. However, these vortex rings are being

used to represent small elements of vortex sheet whose self-induced velocity decreases to zero as the element length goes to zero. Also, if an element of fixed total circulation Γ_m is stretched in time so that its length increases, the vortex strength $\bar{\gamma}(t)$ decreases as $\Gamma_m/\delta s(t)$ and the self-induced velocity increases only logarithmally. In practice, there is a small self-induced velocity for a finite length element which we neglect. It is best to consider the vortex ring distribution as a representation of a continuous vorticity distribution.

In our case the vortex sheet is shed from a sharp edge so that the strength and the initial position of the vortex ring is determined by the shedding previously discussed. Using equation (23), the strength of the m^{th} vortex $\Gamma_m = \gamma_m \delta s_m$ shed in the time δt_m can be written

$$\Gamma_m = 2\delta s_m^2 / \delta t_m \tag{66}$$

where δs_m is given by equation (24). The initial position is taken as the mid-point of the element of vortex sheet shed during the interval δt_m. This leads to a small violation of the Kutta condition and the vortex should be placed at a distance r_m from the edge along the line element

$$r_m = (1 - 1/\lambda)^{\lambda} \delta s_m \tag{67}$$

Graham (1977) pointed out that despite this small error this proeedure allows a better description of the convections of the element off the edge.

A strong condition on the length of the shed element δs_m and hence on the time step δt_m is provided if we

required that the self-induced velocity of the element be small compared to the characteristic convective velocity $U^* = L_v/\delta t_m$ of the edge. Using equations (63) and (64), for $\alpha = \pi/2$ we obtain

$$\frac{U^* \delta t}{L_v} = \frac{C^2 L_v}{4\pi \bar{\sigma}} \left[\ln \frac{256 \bar{\sigma}^2}{C^2 L_v^2} + 2 \right] \tag{68}$$

This requires that $L_v/\bar{\sigma} \ln(L_v/\bar{\sigma})$ be small whereas the assumption that the shedding is 2-D requires only that $L_v/\bar{\sigma}$ be small.

Similarly, when the first vortex is shed by using equations (65), (41), (42), (37) and (38), we obtain

$$\frac{U^* \delta t}{L_v} = \frac{K^{1/(2\lambda-1)} L_v}{2\sqrt{\lambda}\,\bar{\sigma}} \left[\ln \frac{8\bar{\sigma}}{C_c L_v} - .25 \right] \tag{69}$$

Where, in this case $\bar{\sigma} = \sigma_{EDGE} + \sigma_0$ using equation (37), when $\bar{\sigma} \sim O(1)$ and $V \sim O(1)$ and assuming a non-dimensional time step $\delta t/T$ where T is a characteristic time scale, the two equations give:

δ \ $\delta t/T$	.01	.05	.10
0	.04	.10	.13
$\pi/2$	.02	.05	.08
0	.07	.11	.15
$\pi/2$	.03	.10	.15

3.5 Amalgamation process

Moore (1974) has pointed out that the representation of the inner part of the core by a single vortex reduces numerical disturbances in the calculation of the rolling up process. Also, several others (see, for example, Clements, 1973: Sarpkaya, 1975: and Graham, 1977) have suggested that the amalgmation of vortices into a single vortex point is not a source of large errors in calculations involving periodic vortex shedding and it allows a sensible reduction in the number of vortices present in the calculation and therefore saves computing time.

This is a sensible procedure in 2-D flow. The core is assumed to be joined to the outer part of the vortex sheet by a cut through which vorticity is fed into the core according to some criterion. Then, the growing core must follow a Brown & Michael's type of equation; for example, equation (36) where $z_e(t)$ is at the outer end of the cut. If two vortices amalgamate, the strength and position of the resultant vortex can be determined by conservation of the total circulation and total impulse. An amalgamation process can be also applied to a cluster of vortices.

In the case of axisymmetric flow, however, such a representation of the rolling up process may not be appropriate, unless a proper calculation of the self-induced velocity of the resultant vortex ring can be obtained. This is a very difficult problem and instead we assume that the core of the resultant vortex is circular, and that its

radius is equal to the distance between the centre of the vortex and the outer vortex of the sheet. Also, the vorticity is assumed to be uniformly distributed in the core and the vortex ring volume is conserved. The position and the strength of amalgamating vortex rings is given in Lamb (1932) p.239.

The amalgamation process is only applied when the rolling up process is a dominant feature of the flow and the spiral is not affected by the presence of boundaries (Pullin, 1978) or by any other distribution of vorticity with flows. The errors involved in this process are not easily evaluated and this raises doubts about its validity.

The validity of the amalgamation process becomes even more doubtful when it is applied to clusters of vortices. For axisymmetric flows, the self-induced velocity depends strongly on the shape of the cluster and the distribution of vorticity in it. Therefore, general amalgamation should be used only when isolated and concentrated clusters are present and only when far field interactions are important.

4. UNSTEADY VORTEX SHEDDING FROM A CIRCULAR DISC

4.1 Starting flow

The method developed in the previous chapters is used in this section to calculate the external flow around a plane disc of radius R* which starts moving normal to itself with constant speed $\hat{U}^*$. The introduction of the following substitutions enables the problem to be non-dimensionalised

$$(x,\sigma)=(x^*,\sigma^*)/R^*;\ \tau=\hat{U}^*t^*/R^*;\ \Gamma=\Gamma^*/\hat{U}^*R^* \qquad (1)_{a,b,c}$$

where the '*' denotes dimensional quantities.

It is most convenient to calculate the motion of the fluid relative to the disc by assuming that the fluid is set in motion impulsively from rest and then calculating the potential flow as discussed in Chapter 2. The disc is simulated by a distribution of 40 annular elements consistent with the discussion in sections (2.5) and (2.7). Once the velocity field is known, the asymmetric edge velocity V can be evaluated. In general, this is expressed in terms of the tangential velocities Q_w and Q_u at the midpoints of the conical segments on the wetted and unwetted side of the edge

$$V=\frac{\lambda\,\Delta_e^{(\lambda-1)/\lambda}}{2^{(\lambda-1)/\lambda}}\left(\frac{Q_w+Q_u}{2}\right)=C_eQ_e \qquad (2)$$

where Δ_e is the length of the elements either side of the edge, assumed to be the same and Q_w and Q_u, measured in the direction of the positive arc length s, are calculated by means of equation (2.6.95).

For the special case, $\delta=0$, each annular element represents either the wetted or the unwetted side of the disc. It contributes twice to the arc lengths and the positive direction is assumed, as in section (2.5), to be clockwise (anti-clockwise) round the edge in the case of external (internal) flows. Therefore, for the problem under investigation, the velocity Q_e is given by the first term of equation (2.6.95) without any contribution of $\underline{V}_v$ and $\underline{V}_\infty$. Then the first vortex is shed using equations (3.2.26), (3.2.37) and (3.2.38) and the potential flow is calculated again.

In general, once the strength of the bound vortices and hence the tangential velocity has been calculated, equation (2.1.9) can be used to calculate the pressure distribution acting on the disc surface. The velocity potential $\phi(s,\tau)$ is defined as

$$\phi(s,\tau) = \phi(0,\tau) + \int_0^s V_t(s',\tau)\, ds' \qquad (3)$$

where the integral is evaluated on the instantaneous streamline $\mathcal{S}_1$ (see Fig. (4.1.)) Combining equations (3) and (3.2.8) we have that for $s \geq s_2$

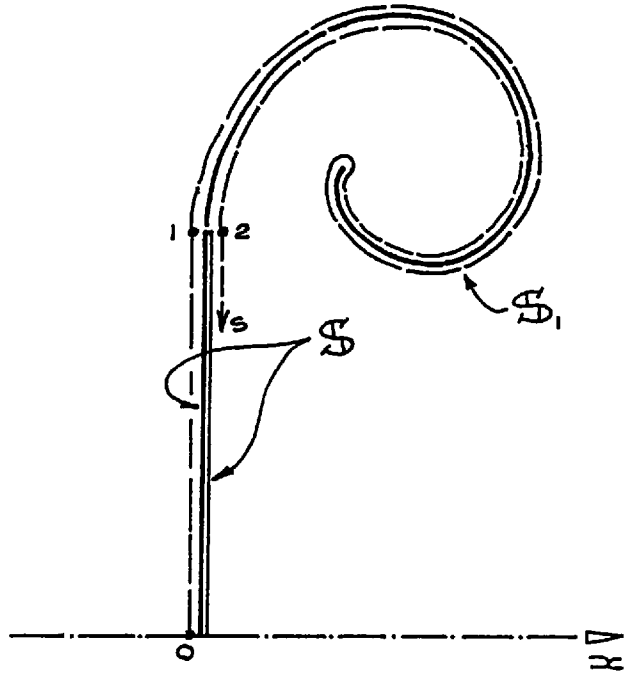

Fig. 4.1

$$\phi(s,\tau) = \phi(0;\tau) + \int_{s_2}^{s} V_t(s',\tau) + \Gamma(\tau) \tag{4}$$

$$\Delta\phi(\tau) = \phi(s_2,\tau) - \phi(s_1,\tau) = \Gamma(\tau) \tag{5}$$

where $\Gamma(\tau)$ is the total circulation of the vortex sheet. The arc length s is now assumed to be taken along the disc surface $\mathcal{S}$ $(s_1 = s_2)$

The integral in equations (3) and (4) is evaluated by the single trapezoidal rule using the values of the tangential velocity at the midpoint of the annular elements.

$$I_k = \int_{s_{k_1}}^{s_{k_2}} V_t\, ds = \sum_{k_1}^{k_2-1} k\left[\frac{(V_t)_{i+1} + (V_t)_i}{2}\right]\frac{(s_{i+2} - s_i)}{2} \tag{6}$$

where

$$\begin{cases} i = k & 1 \le k \le N \\ i = 2N - k + 1 & N+1 \le k \le 2N \end{cases} \tag{7 a,b}$$

$$(V_t)_1 = 0 \tag{8}$$

Also $$\Delta\phi = \phi(s_{N+1}) - \phi(s_N) = \Gamma + \Delta\phi_e \tag{9}$$

where $$\Delta\phi_e = \int_{\bar{s}_N}^{s_N} V_t\, ds' + \int_{s_N}^{\bar{s}_{N+1}} V_t\, ds' \tag{10}$$

and

$$\bar{s}_i = (s_{i+1} + s_i)/2 \qquad \Delta_e = \bar{s}_{N+1} - \bar{s}_N \tag{11 a, b}$$

The velocity distribution near the edge shows

a very low velocity on the separated side and a rapid rise towards $Q_w \to \gamma$ on the wetted side. This makes it difficult to estimate $\Delta\phi_e$. However, in general, we can assume that such a feature is due to the just shed vortex which induces an asymmetric tangential velocity round the edge

$$Q(r) \sim \frac{\Gamma_m}{\pi\sqrt{r}}\left[\frac{1}{\sqrt{s_m}} - \frac{1}{2^{3/2}\sqrt{s_m + r}}\right] \tag{12}$$

where r is the distance from the edge along the thin-wall. Then, equation (10) can be transformed so that

$$\Delta\phi_e = \Delta\phi_e^{(1)} + \Delta\phi_e^{(2)} = \left[\tilde{V}_t(\bar{s}_N, \tau) + \tilde{V}_t(\bar{s}_{N+1}, \tau)\right]\Delta_e + 2\int_0^{\Delta_e} Q(r)\,dr \tag{13}$$

where $\tilde{V}_t$ is the tangential velocity evaluated without the contribution of the m^{th} free vortex. Using equation (12), we have

$$\Delta\phi_e^{(2)} = \frac{2\Gamma_m}{\pi}\left[\sqrt{2\tilde{\Delta}} - .5\,\ln\left(\sqrt{\tilde{\Delta}+1} + \sqrt{\tilde{\Delta}}\right)\right] \tag{14}$$

where $\tilde{\Delta} = \Delta_e / s_m$. However, numerical calculations have shown that if $\tilde{\Delta} \ll 1$ equation (13) can be approximated by

$$\Delta\phi_e = \left[V_t(\bar{s}_N, \tau) + V_t(\bar{s}_{N+1}, \tau)\right] \tag{15}$$

where the tangential velocity is assumed to be constant on the two sides of the edge element.

Once the pressure distribution is known, the pressure coefficient

$$C_p(s,\tau) = 2\left[p^*(s,\tau) - p^*(\infty,\tau)\right]/\rho\hat{U}^{*2} \tag{16}$$

and the unsteady drag coefficient

$$C_D(\tau) = \frac{1}{\pi}\int_S C_p(s,\tau)\,ds \tag{17}$$

can be calculated.

The subsequent position of the first vortex or, in general, of each free vortex is calculated from the total velocity (U_m, V_m) induced by all other vortex elements and computed by equations (2.3.32) and (2.3.33). The new position is given approximately by

$$(x_m, \sigma_m)^{(k+1)} = (x_m, \sigma_m)^{(k)} + (U_m, V_m)^{(k)} \delta\tau + O(\delta\tau^2) \tag{18}$$

where "k+1" indicates the solution at the time $(\tau + \delta\tau)$. This is a coarse intergration scheme and an improvement was tried by using

$$(x_m, \sigma_m)^{(k+1)} = (x_m, \sigma_m)^{(k)} + .5\left[3(U_m, V_m)^{(k)} - (U_m, V_m)^{(k-1)}\right]\delta\tau + O(\delta\tau^3) \tag{19}$$

However, the calculations did not show any sensible difference between equations (18) and (19) for a large set of different $\delta\tau$ and therefore the order of the error introduced by equation (18) was assumed to be consistent with the order of approximation given by the general method under investigation.

At the new time step the potential flow and the asymmetric edge velocity V are calculated again and a new vortex is shed into the free vortex sheet, using equations (3.2.24), (3.2.26) and (3.4.66). Then, the process is continued as described before and it is repeated at the next time step. The vortex release and integration time steps are assumed to be the same.

The calculated initial shear layer behind the disc, at $\tau = 1.$, is shown in Fig. (4.2). The calculation

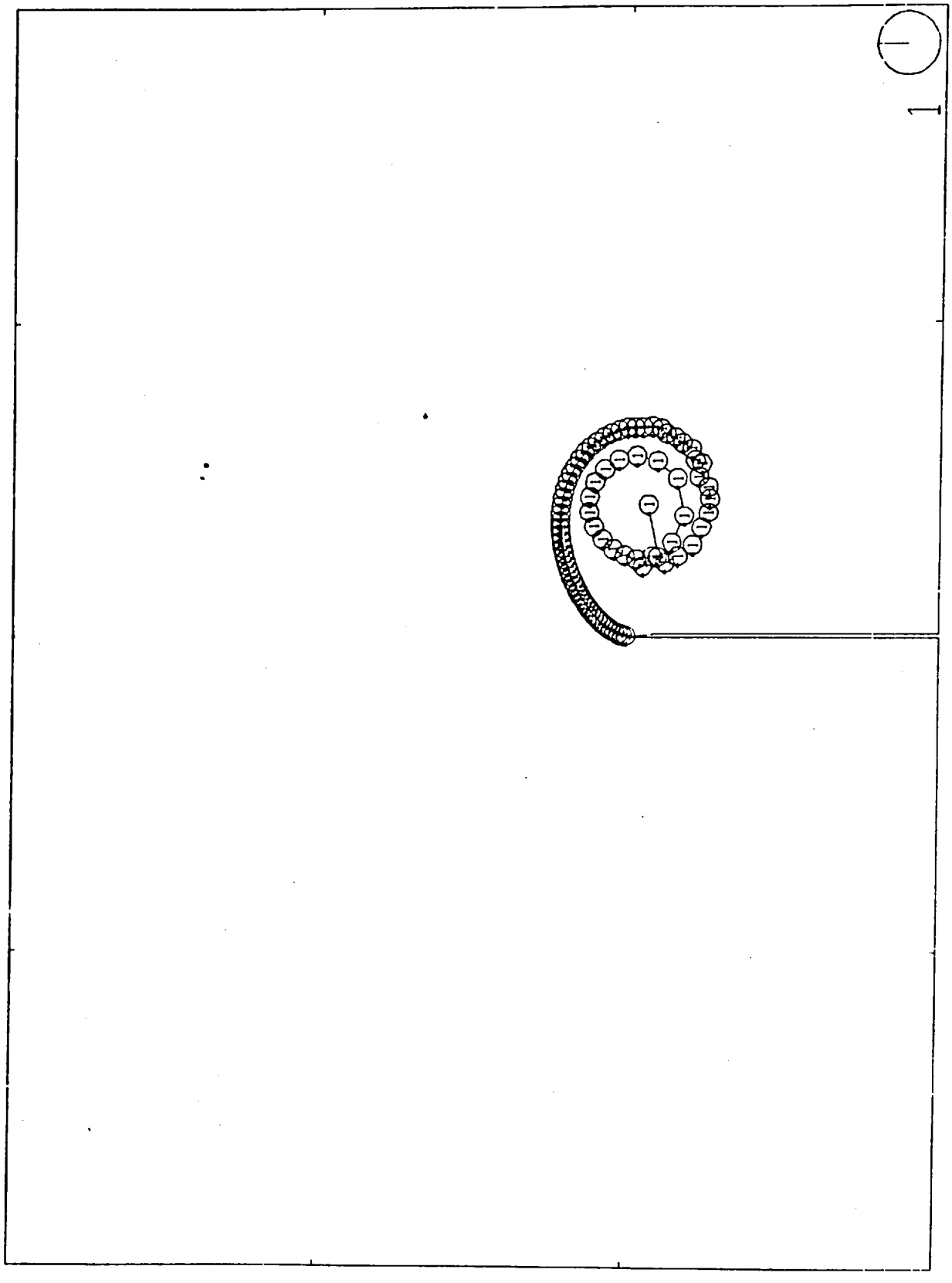

Fig. 4.2

was made with $\delta\tau=.01$ and a vortex was wound into the core every five time steps. The shed vortex sheet rolls up into a spiral which shows a smooth behaviour as well as the growth of a few kinks of the type discussed by Moore (1974). These disturbances are due to the unrealistically fast growth of the core which forces the innermost turns of the spiral to be too close. Then, an orbitting process is obtained if the angle θ between the three innermost vortices is examined at each time step and a vortex is absorbed into the core when θ exceeds $2\pi/M$ where M is minimum number of vortices on each turn (Moore, 1974).

A series of numerical calculations were made with different time steps $\delta\tau$ to find an optimal value. As $\delta\tau$ decreases the number of free vortices increases giving a better approximation for the free shear layer and for the convection process. However, the total computing time increases as the square of the total number of vortices. The results are shown in the upper half of Fig. (4.3).

The lower half of Fig. (4.3) shows the results for a single flat plate started impulsively from rest obtained by Kamemoto & Bearman (1978). In their calculations, they have employed a discrete vortex method to simulate the evolution of the shear layer and the method of "fixed points", as introduced by Kiya and Arie (1977), to calculate the vortex shedding process. In this method, the nascent vortices are introduced at two fixed points near the edges in the plane of the flat plate every two integration time steps and their strength is determined from the Kutta

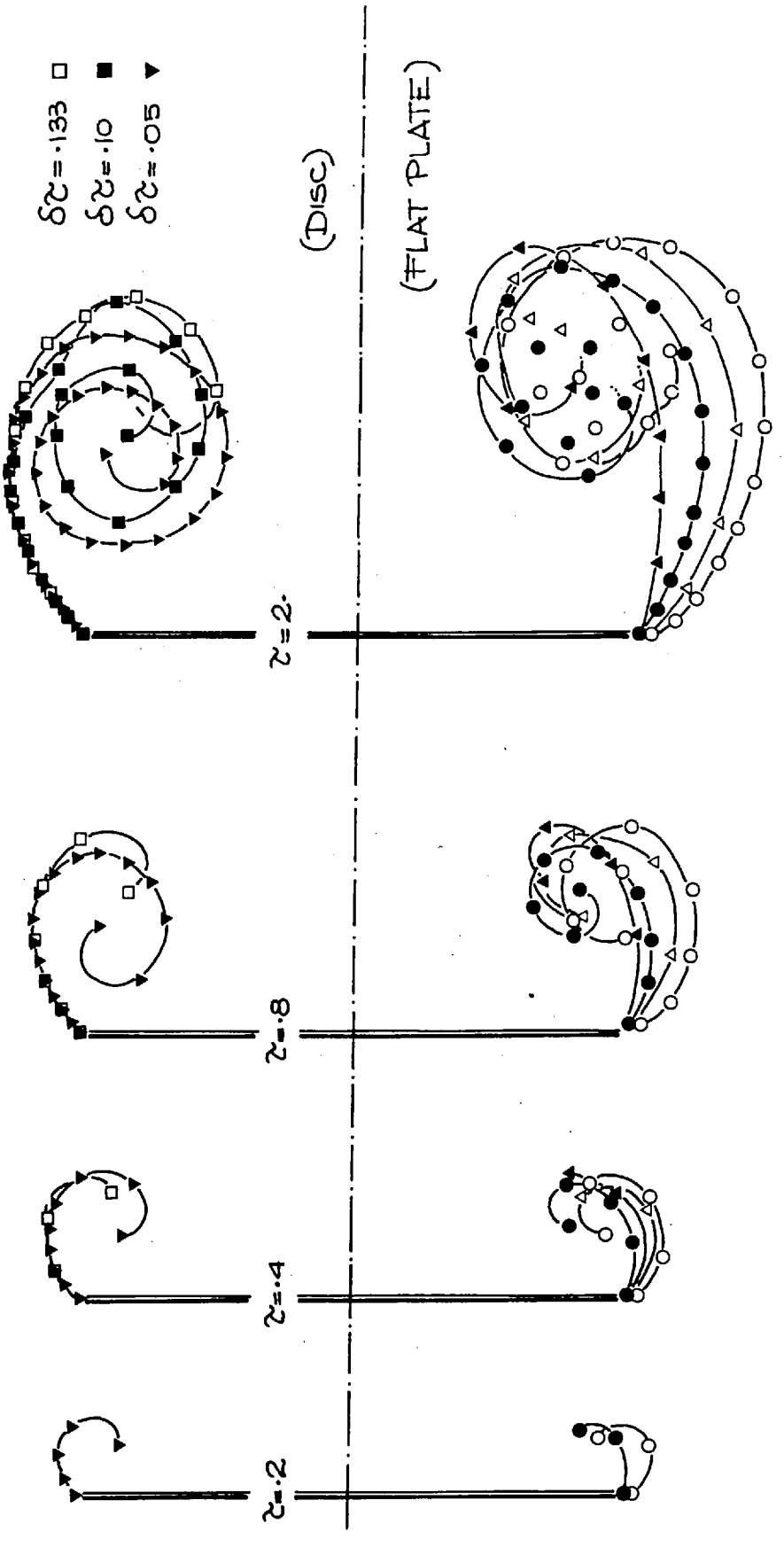

Fig. 4.3

condition. However, the method is strongly dependent on the integration time step $\delta\tau$ as shown by the analysis in section (3.2). Kiya and Arie carried out several calculations with $\delta\tau = .08$ and for several distances δs and in view of the reasonable results for the Strouhal number and the nature of the vortex formation, they recommend

$$.005 \leq \delta s \leq .0125$$

Kamemoto & Bearman investigated the relation between the distance and the time interval by transforming the flat plate into a circle and applying the method in the transformed plane. They concluded that the non-dimensional number $\delta s'/\delta\tau$ where $\delta s'$ is the transformed distance is an important parameter and that there exists a lower limit to the acceptable value of the parameter. Their results for the cases presented in Fig. (4.3) are

$\delta\tau$	δs	$\delta s'/\delta\tau$	Symbols
.2	.05	.93	Δ
.1	.05	1.86	O
.2	.01	.38	▲
.1	.01	.76	●

As expected the agreement between the 2-D and the axisymmetric case is very good for a short time ($\tau < .5$) After this time the self-induced velocity becomes important and keeps the developing circular vortex filament closer

to the unwetted wall. The axisymmetric case also shows a marked insensitivity to the choice of the time step when $\delta\tau < \cdot 1$. On the contrary, the 'fixed points' method gives quite different results for different values of the parameters. There are different shapes of the free shear layer, and even if the vortex clusters are similar it seems quite difficult to decide the right set of parameters. Fig.(4.4) shows the initial growth of the total strength of the axisymmetric vortex sheet compared with the curve obtained for the 2-D flat plate by Kamemoto & Bearman (1978), Fink & Soh (1974) and Graham (1977). It is interesting to observe again that for $\tau < \cdot 5 \div 1 \cdot$ the axisymmetric and the 2-D curves presents an high similarity, but in general the disc produces a weaker wake.

For a longer time disturbances grow and a chaotic cluster of vortices replaces the inner spiral. Only the free shear layer close to the edge presents a smooth behaviour. Fig. (4.5) shows the flow patterns for $\tau = 10 \cdot$ The 2-D starts developing an asymmetric wake whereas by our method the disc is forced to keep its axisymmetric behaviour. This is quite wrong (Goldstein, 1965). A stationary separated region behind the disc where the viscosity dissipates the vorticity produced at the sharp edge was observed to exist only for $Re < 100 \div 195$, where $Re = 2R^* \hat{U}^* / \nu$ and ν is the kinematic viscosity. This region of permanent circulation behaves more like an Hill's vortex than a circular vortex ring and, indeed, as the Reynolds number is increased, the vortex grows becoming unstable, discharging fluid downstream at regular

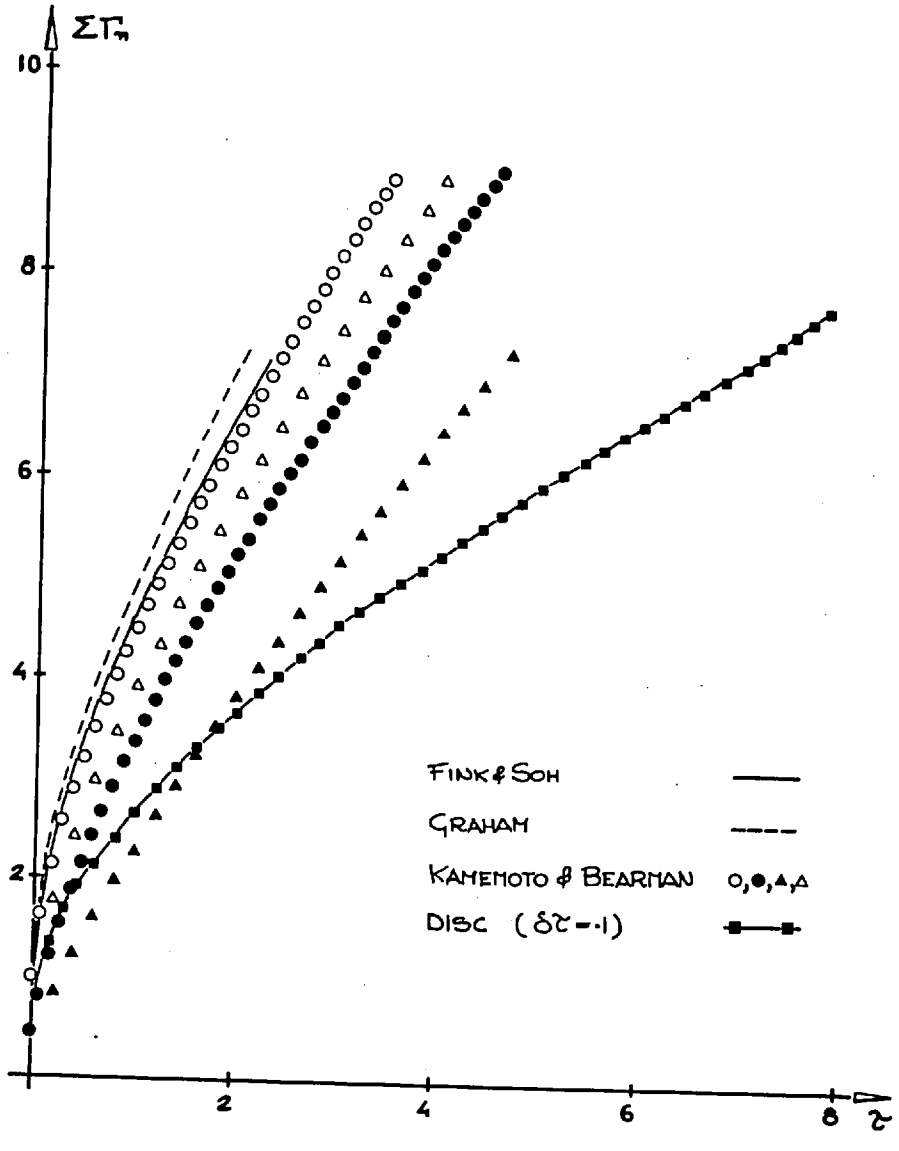
ΣΓm
10
8
6
4
2
2
4
6
8
τ
FINK & SOH
GRAHAM
KANEMOTO & BEARMAN o,●,▲,△
DISC (δτ=·1)

Fig. 4.4

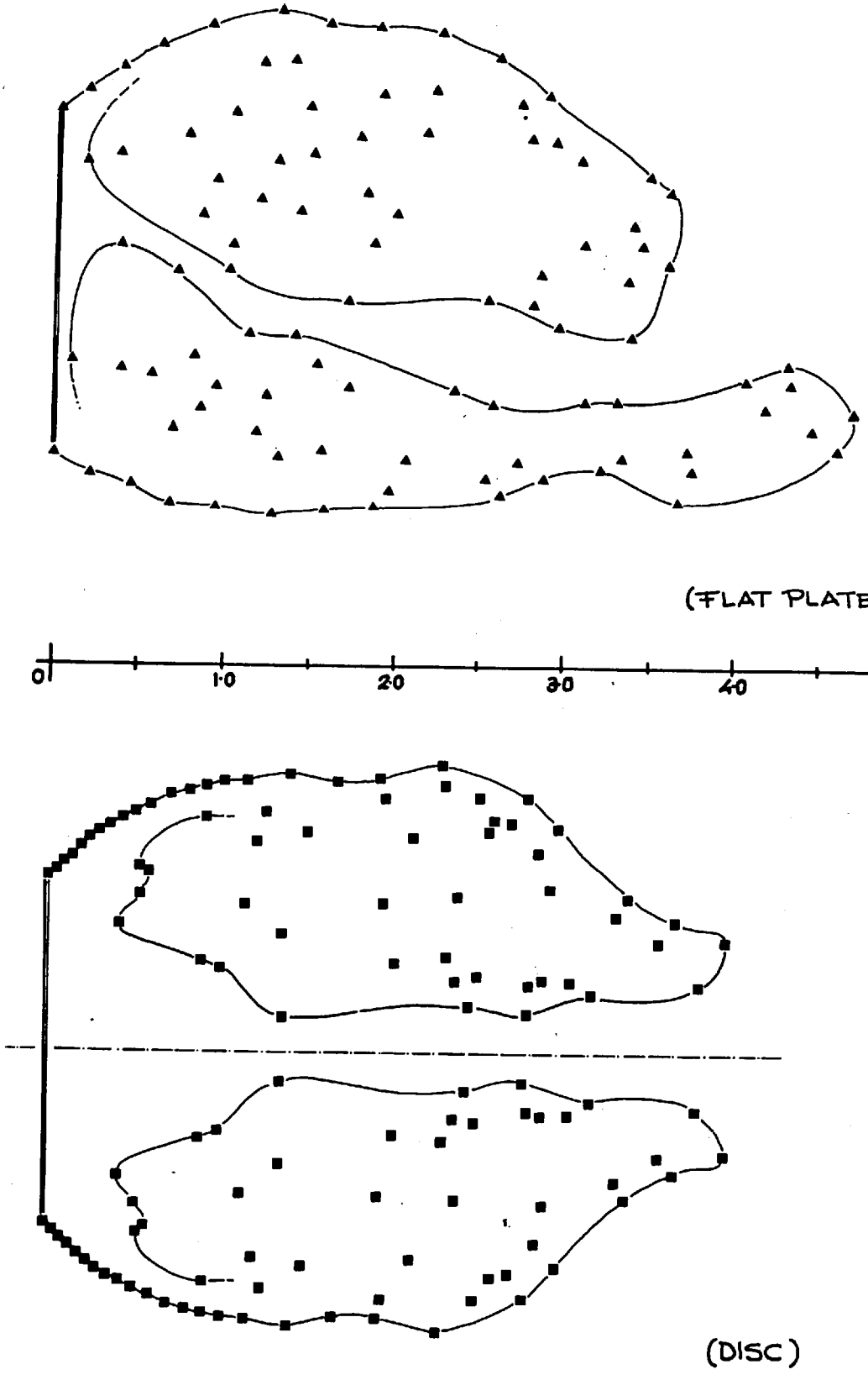

Fig. 4.5

intervals in time. This unstable process presents similarities with the Hill's vortex instability analysed by Moffatt & Moore (1978). At a higher Reynold's number, the wake behind the disc presents an axisymmetric vortex sheet on which a 3-D disturbance grows and makes part of the vortex sheet break away. This starts the formation of 3-D vortex loops which are the main feature of the far wake. Then, if the Reynolds number is increased again, the vortex loops on the vortex sheet, existing only for a very short distance downstream, break very rapidly and eventually turbulence appears.

In spite of the unrealistic behaviour of the numerical simulation, the instantaneous drag coefficient $C_D(\tau)$ shown in Fig. (4.6), tends to the experimental value, $C_D^{(e)} = 1.1$ as the non-dimensional time increases. This may be due to a good representation of the velocity field near the walls and of the vortex shedding rate. Fig. (4.6) also shows the 2-D curves calculated by Kamemoto & Bearman (1978) and Fink & Soh (1974), for comparison.

Bearman & Fackrell (1975) calculated the incompressible potential flow external to a steadily moving disc and its wake by using a generalised Parkinson & Jandali's (1970) source method. This suggested that the position of the shear layer, replaced by a free streamline may be found by adding a source system on the unwetted side of the body which satisfies the boundary conditions and by specifying the base pressure in the separated region. They represented the disc surface by a distribution of vortex rings and superimposed a ring source. Then, they found

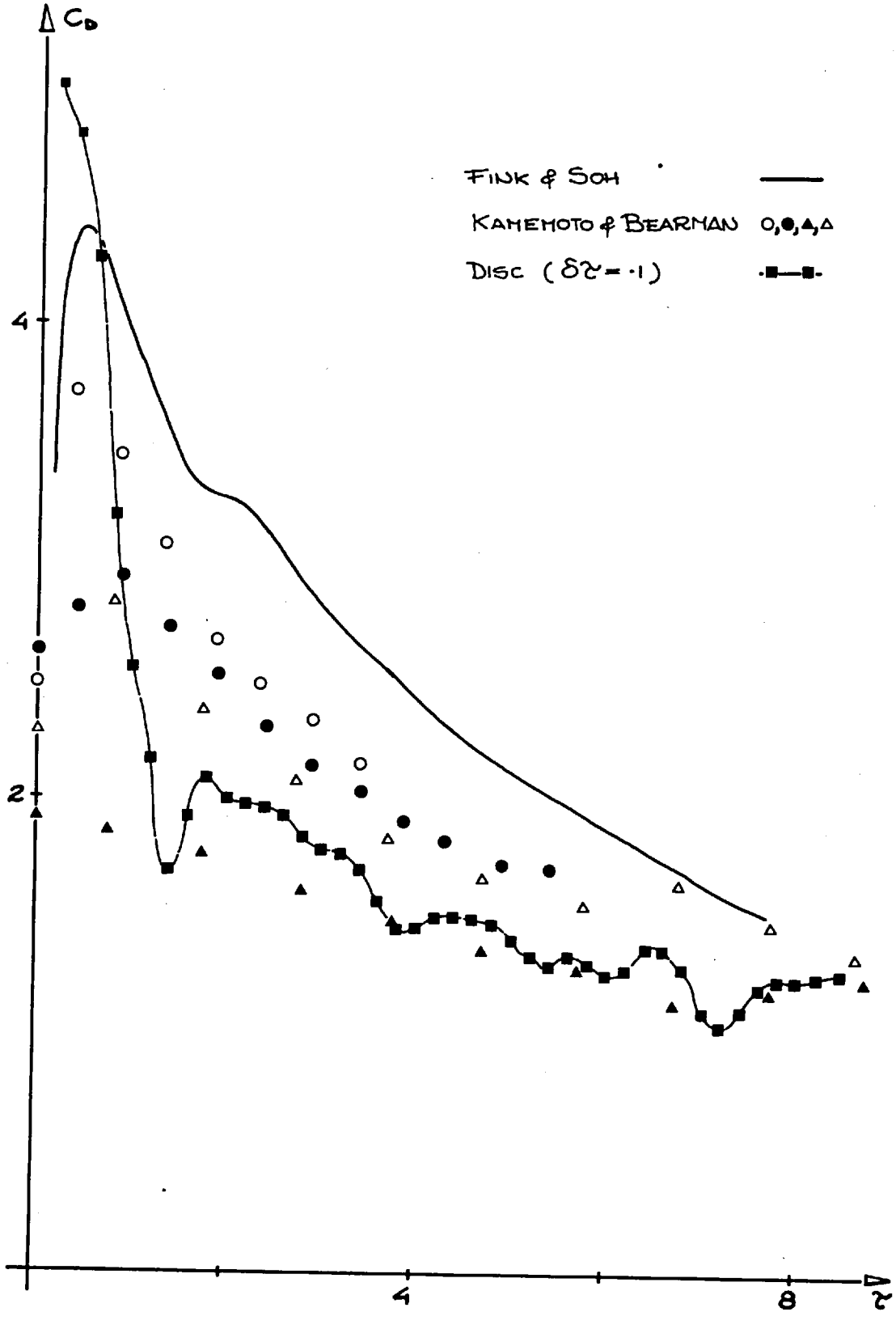
C_D
FINK & SOH
KAMEMOTO & BEARMAN O,●,▲,△
DISC ($\delta\gamma = \cdot 1$)
4
2
4
8
γ

Fig. 4.6

the distribution of vorticity, the source position and strength consistent with the boundary condition of zero normal velocity on the disc surface and a given base pressure C_{pb} . The method calculates the flow external to the free streamline on the wetted surface but does not model the mean flow in the wake. Fig. (4.7) shows the pressure distribution on the disc wetted surface calculated by the present method for $\gamma = 9.0, 10.0$, and by Bearman & Fackrell source method. They are almost identical and both agree well with the experimental value of Fail, Lawford and Eyre (1957).

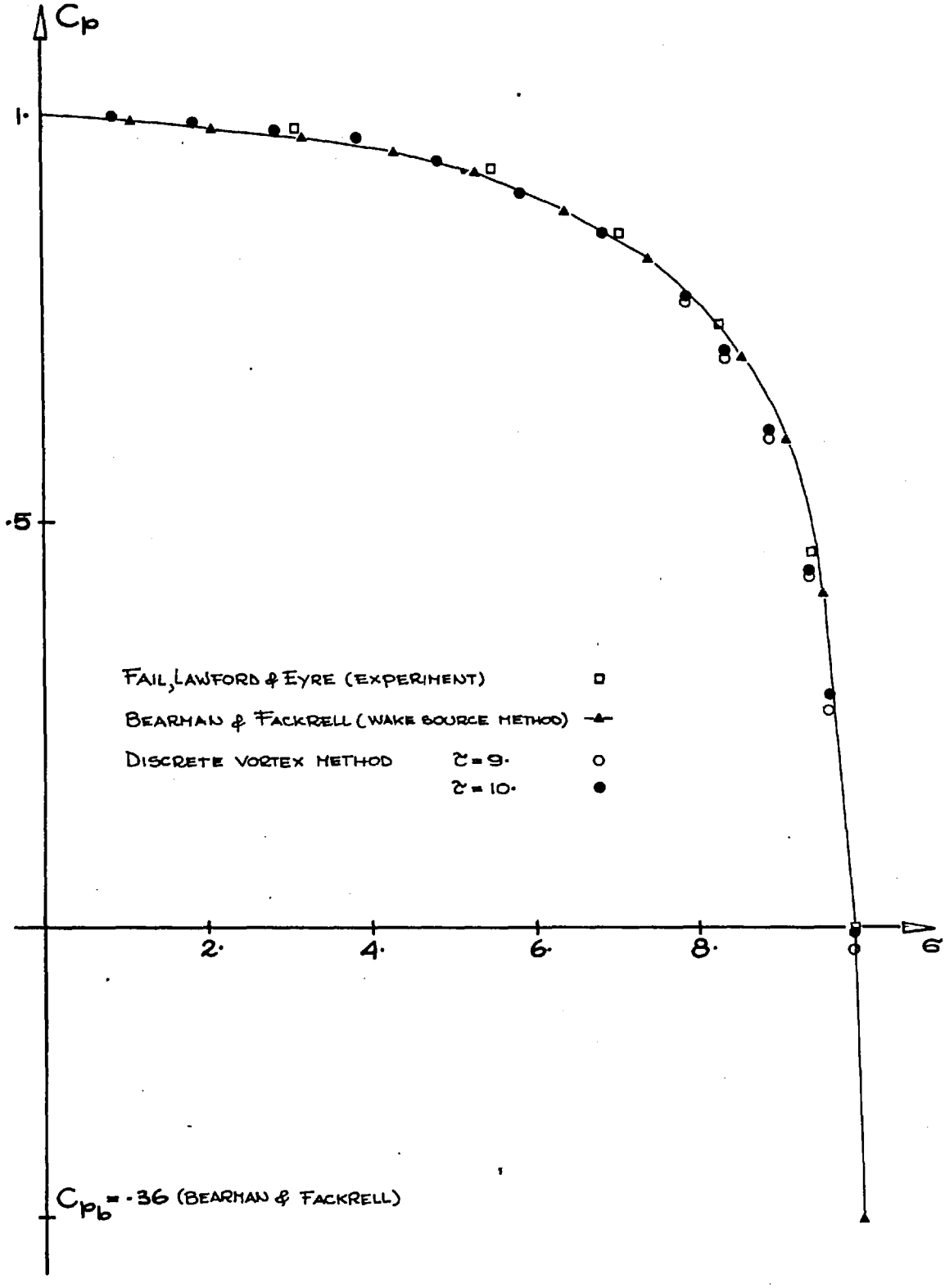
Cp
1·
·5
2·
4·
6·
8·
10·
12·
FAIL, LAWFORD & EYRE (EXPERIMENT)
BEARMAN & FACKRELL (WAKE SOURCE METHOD)
DISCRETE VORTEX METHOD
ζ = 9·
ζ = 10·
Cpb = -36 (BEARMAN & FACKRELL)

Fig. 4.7

4.2 Oscillating disc flow

In this section the fluid is assumed to start oscillating normal to the disc plane with speed $\frac{U^*}{\hat{U}^*} = \sin 2\pi\tau$ where $\tau = t^*/T^*$ is the time non-dimensionalized by the period of oscillation T^* and $K = \hat{U}^* T^*/R^*$ is the Keulegan-Carpenter number upon which the inviscid problem depends. However, the real problem will be characterized by an additional dimensionless group, either the Reynolds number $R_e = 2R^*\hat{U}^*/\nu$ or the frequency parameter $\alpha = R^*[2\pi/\nu T^*]^{1/2}$. However, Keulegan & Carpenter (1958) studying the oscillatory flow round flat plates and circular cylinders, showed that the force F in the flow direction was in the form of Morison's equation

$$F = \rho R^* C_D U^* |U^*| + \pi \rho R^{*2} C_M \dot{U}^* \qquad (20)$$

In the case of sharp-edged body, the drag and the inertia coefficients C_D and C_M were functions of K without any significant effect of the Reynolds number.

Experiments by Maull & Milliner (1978) and Bearman, Graham and Singh (1978) on various cylindrical bodies, have shown that two quite different flow regions exist. If we define K_c to be a critical value depending on the shape of the body, for $K > K_c$ the flow past the body separates forming a limited wake. The length of this wake and resemblance of the flow to the corresponding steady free stream case grows with increasing K. When $K < K_c$, vortices shed at the separation point, are swept back past the body because of the shorter amplitude of the flow oscillations and they are forced to interact with successive vortices

of opposite sign to form regular flow patterns.

When $K > K_c$ equation (20) with a suitable choice of the coefficients offers accurate predictions of the in-line force. However, the predictions are not so good for $K < K_c$. Graham (1980), following Maull & Milliner's suggestion (1978), calculated the force from the complex potential due to distributed point vortices through Blasius's theorem. He conveniently assumed that the force arose from two contributions, one associated with the inertial force occuring for the attached flow around the body and the other from the distribution of shed vortices. Thus,

$$F = \pi \rho C_{MO} R^{*2} \dot{U}^* + F_V \tag{21}$$

where C_{MO} is the value of the inertia coefficient for the attached flow and F_V is the vortex force component. The unsteady axial force acting on the disc is

$$F(\tau) = \int_S p^*(s,\tau)\, ds \tag{22}$$

then equation (21) can be generalised to the disc case as

$$F(\tau) = \frac{4}{3}\pi \rho \dot{U}^* R^{*3} C_{MO} + \frac{1}{2}\pi \rho \hat{U}^{*2} R^{*2} C_{FV}(\tau) \tag{23}$$

where C_{FV} is the vortex force coefficient, non-dimensionalized by the disc area and the inertial coefficient C_{MO} on a sphere of equal radius can be calculated remembering that the disc energy is

$$T_E = \frac{4}{3}\rho R^{*3} U^{*2} \tag{24}$$

and the inertial force acting on the disc is

$$F = \frac{1}{U^*}\frac{dT_E}{dt^*} \tag{25}$$

Then, using equations (25), (24), and the first inertial term of equation (23), we have

$$C_{HO} = 2/\pi \tag{26}$$

A large number of preliminary calculations were carried out with the same K to determine the dependence of the calculated force upon the time step $\delta\tau$. It was found that $\delta\tau \leq .05$ produced satisfactory results and, in general, the features of the force F are quite independent of $\delta\tau$. Fig. (4.8) shows the calculated $C_{FV}(\tau)$ with K = 3.5 and for $\delta\tau$ = .05, .04, .03, .05.

Fig. (4.9) shows a plot calculated for the first 1½ cycles starting from rest, for different values of K. The amplitude decreases with increasing K and the zero crossing points are remarkably constant up to a value of K about 3. The peak amplitudes after an initial transition in the first half of the cycle, remain fairly constant.

Equation (23) can be written in the form of Morison's eqn.

$$F(\tau) = \frac{4}{3}\pi\rho R^{*3} C_M \dot{U}^* + \frac{\pi}{2}\rho R^{*2} C_D U^*|U^*| \tag{27}$$

by taking the appropriate Fourier integral over one cycle of the flow. Then substituting for $U^* = \hat{U}^* \sin\theta$ where $\theta = 2\pi\frac{t^*}{T^*}$

$$F = \frac{8\pi^2}{3T^*}\hat{U}^*\rho R^{*3} C_M \cos\theta + \frac{\pi \hat{U}^{*2}}{2}\rho R^{*2} C_D \sin\theta|\sin\theta| \tag{28}$$

Multiplying equation (28) by $\frac{\cos\theta}{T^*}$ and integrating between zero and T^* and noting that

$$\frac{1}{T}\int_0^T \sin\theta|\sin\theta|\cos\theta\, dt = 0 \tag{29}$$

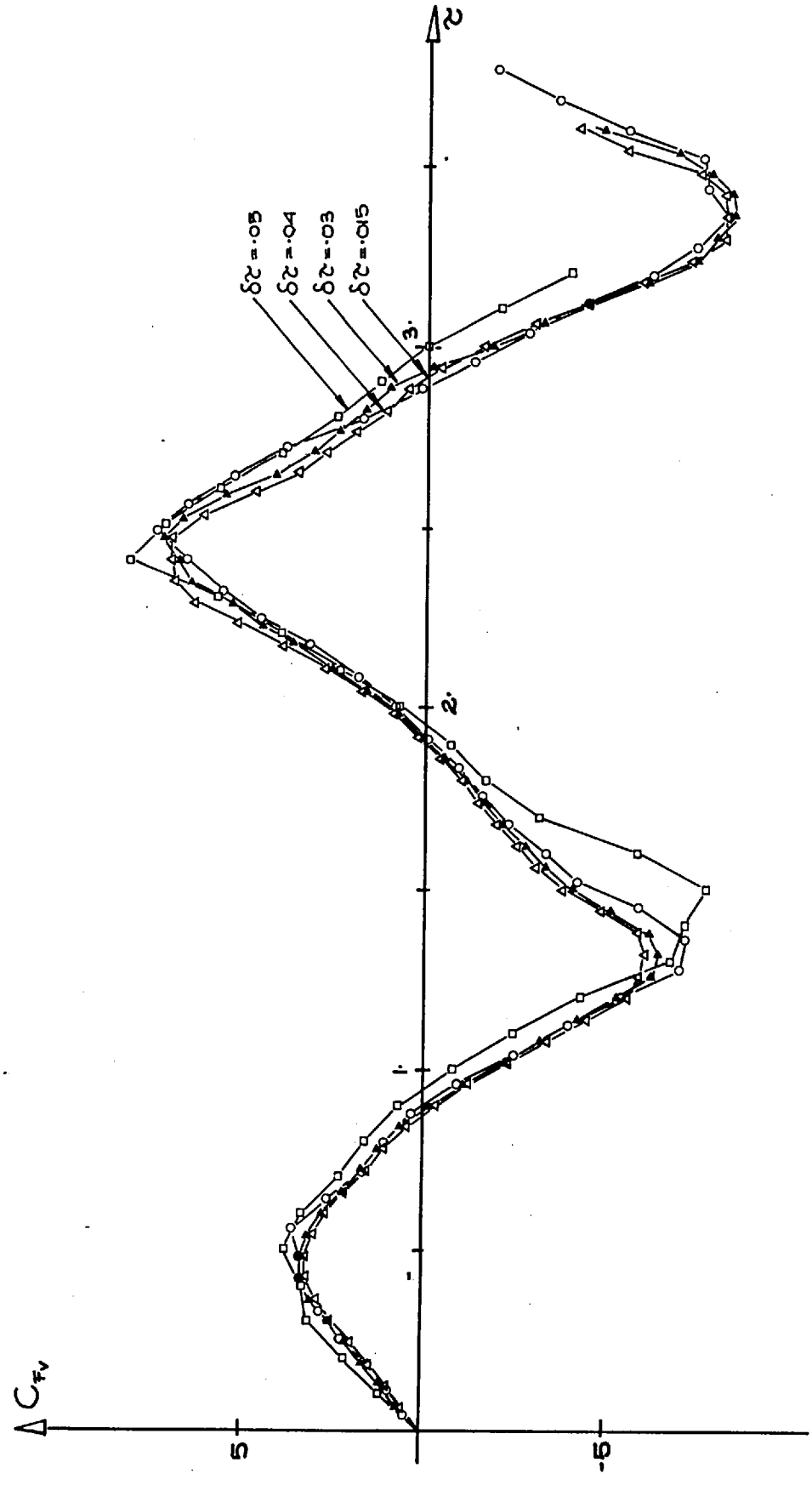
α
$\delta\alpha$=.05
$\delta\alpha$=.04
$\delta\alpha$=.03
$\delta\alpha$=.015
3.
2.
1.
C_{Fv}
5
-5

Fig. 4.8

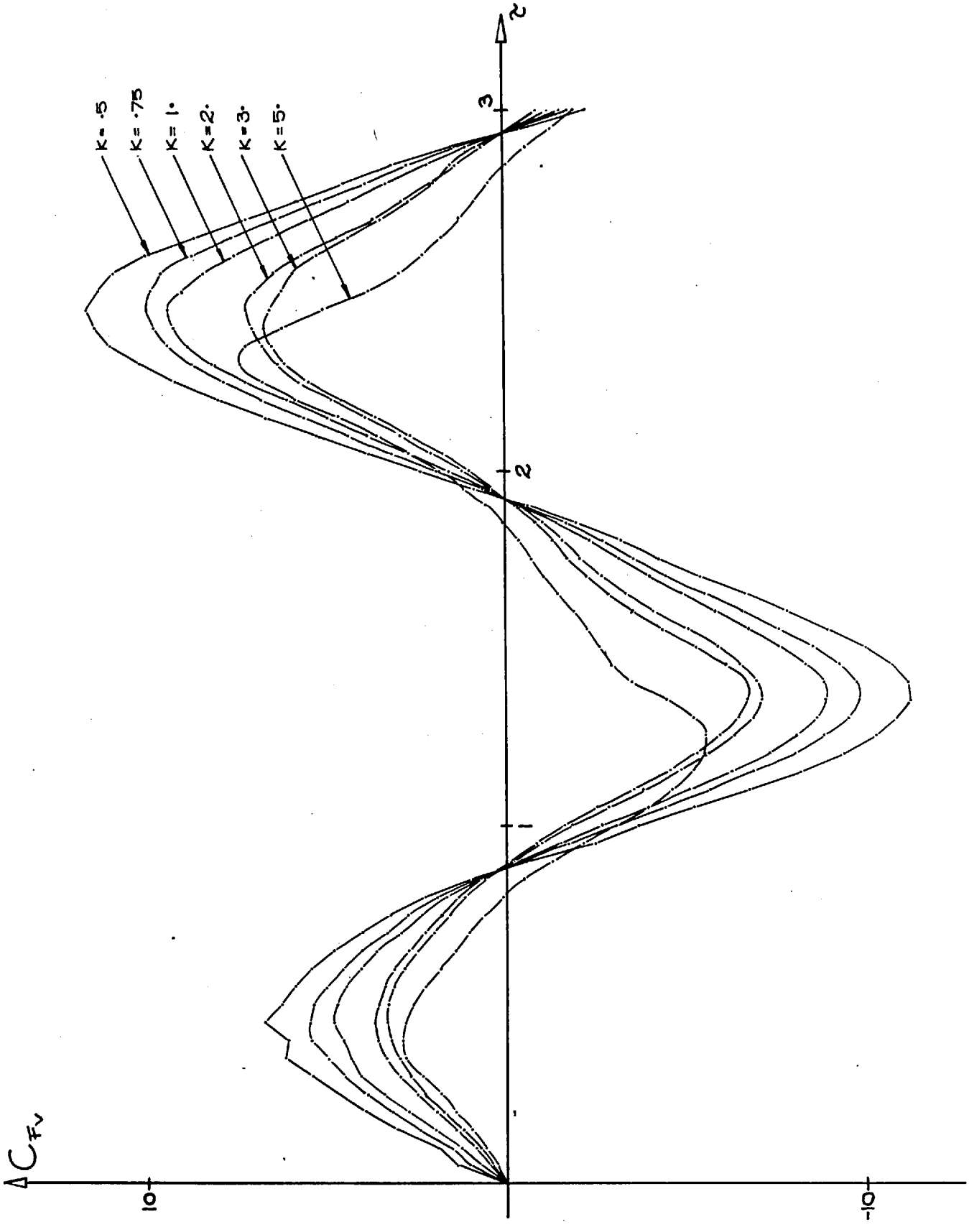

Fig. 4.9

and

$$\frac{1}{T}\int_0^T \cos^2\theta\, dt = \frac{1}{2} \tag{30}$$

we have

$$\frac{1}{T}\int_0^T F(t)\, dt = \frac{4\pi^2}{3T^*}\hat{U}^*\rho R^{*3} C_M \tag{31}$$

Then, using equation (23)

$$C_M = C_{M_0} + \frac{3K}{8\pi}\int_0^1 C_{F_V}(\tau)\cos 2\pi\tau\, d\tau \tag{32}$$

Similarly, multiplying equation (28) by $\sin\theta/T$ integrating and noticing that

$$\frac{1}{T}\int_0^T \sin^2\theta\,|\sin\theta|\, dt = \frac{4}{3\pi} \tag{33}$$

we have

$$C_D = \frac{3\pi}{4}\int_0^1 C_{F_V}(\tau)\sin 2\pi\tau\, d\tau \tag{34}$$

For small values of K, the vortex shedding close to the disc should be similar to that for a single plane edge. For this case Graham (1980) has shown that

$$C_D - A K^{(3-2\lambda)/(2\lambda-1)} \tag{35}$$

and

$$C_M = C_{M_0} + B K^{2/(2\lambda-1)} \tag{36}$$

where A and B are fixed coefficients given by the Fourier integrals. Fig. (4.10) shows the calculated values of C_D and $(C_M - C_{M_0})K^{-1}$ compared with the values for a single edge with $\lambda = 2$. The disc results show the $K^{-1/3}$

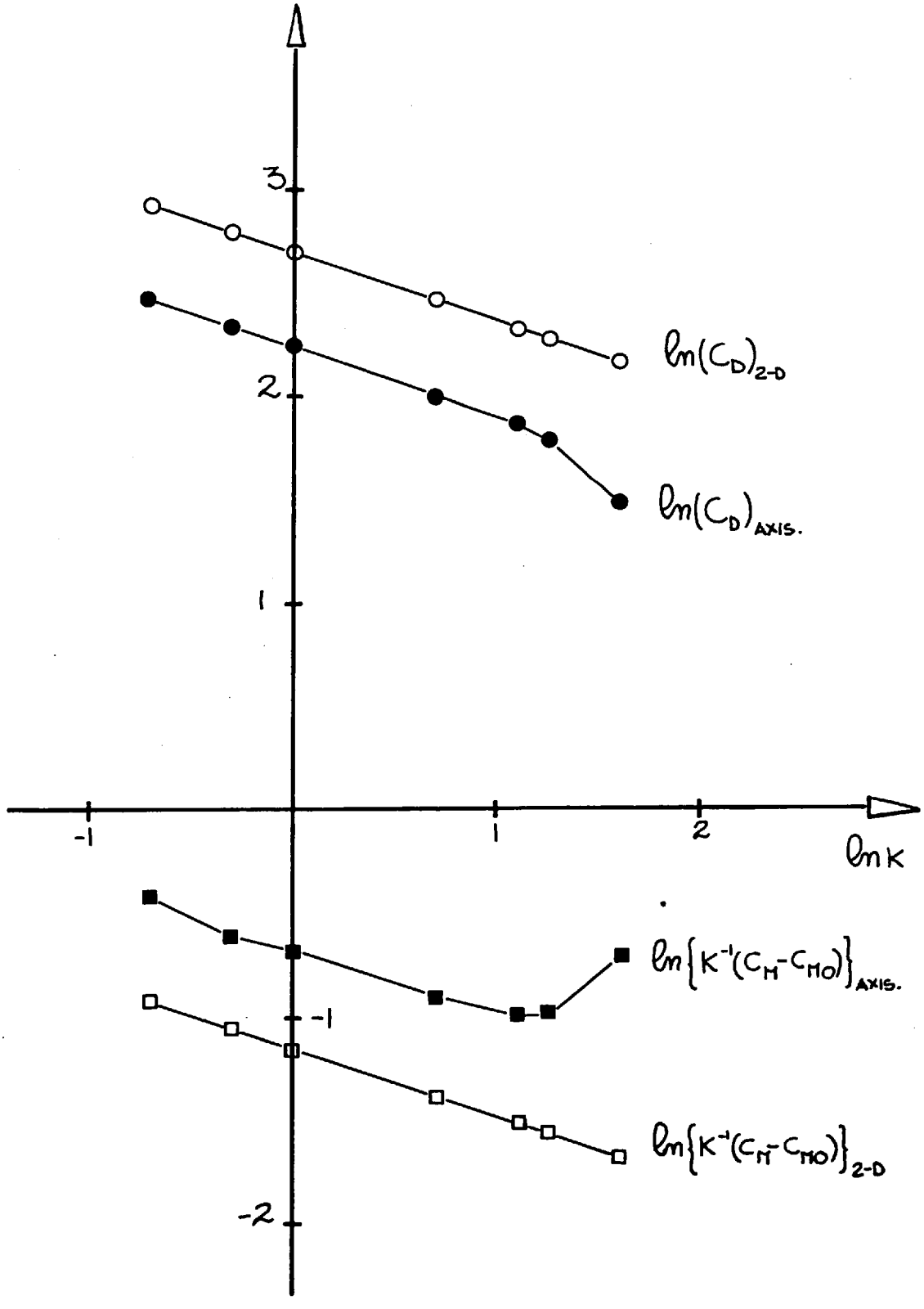

Fig. 4.10

behaviour predicted up to a value of K of about 3 above which they diverge rapidly.

The only data available on the force acting on an oscillating disc are those obtained by Tojo et al (1979) for a vibrating disc column. This consists of a vertical cylinder divided in four horizontal cells by circular flat plate orifices. In each cell, whose height is comparable to the cylinder diameter $2R_c$ is a disc of radius $R_D = .78 \sim .58$ which is oscillated to produce agitation in the column. They represented the total force by Morison's equation (27). They found values for C_M and C_D considerably higher than in the case of an isolated oscillating disc and strongly influenced by the presence of the walls. Remarkably, they observed that both the coefficients were almost independent of the Reynolds number Re, ranging from 10^2 to 10^5 and expressed such a dependence as

$$C_M = 55.3 (R_D/R_c)^{2.5} R_e^{-.061} \qquad (28)$$

$$C_D = 141 (R_D/R_c)^{2.9} R_e^{.04} \qquad (29)$$

They did not present any analysis of the dependence of the coefficients on the Keulegan-Carpenter number K which ranges between .9 and 3.5. Such a dependence cannot be recovered from the presented results.

The flow patterns for the disc also show remarkable similarity with the 2-D flow. Preliminary calculations with $\delta\tau = .05$ and amalgamation (M=3) showed that after a few cycles an asymmetric wake was formed behind the disc due to a pairing process between vortices of opposite

strength. Fig. (4.11) shows the distribution of the centres of the primary vorticity of opposite sign after four cycles. An experiment was performed to check these calculations. A disc of 4 cm radius and 0.16 cm thick was fixed at the end of a long rod about 0.3 cm radius and oscillated sinusoidally in the centre of a circular tank, 50 cm diameter by 80 cm. The tank was filled with a saline solution in which neutrally buoyant polystyrene beads were suspended. The beads were illuminated by two collimated slit lamps (about 3 mm wide) which illuminated a plane containing the axis of symmetry normal to the camera. Particle tracks were obtained by taking photographs of relatively long exposure (1/25 s.) The experimental and calculated results for $K = 3.5$ are compared in Fig. (4.12). The line joining two vortex rings indicates that the distance between the two sequential vortices has remained less than four times the characteristic shedding length. This is a good indication that that part of the vortex sheet retained an identifiable structure.

In comparing calculations and experiments, it must be remembered that the experimental photographs show particle tracks while the theoretical results show the instantaneous distribution of vorticity, so that they cannot be compared directly (Clements, 1973). However, the point vortices also serve as fluid markers and the experimental results give a qualitative indication of the location of the primary vorticity. In this qualitative sense, the results agree quite well.

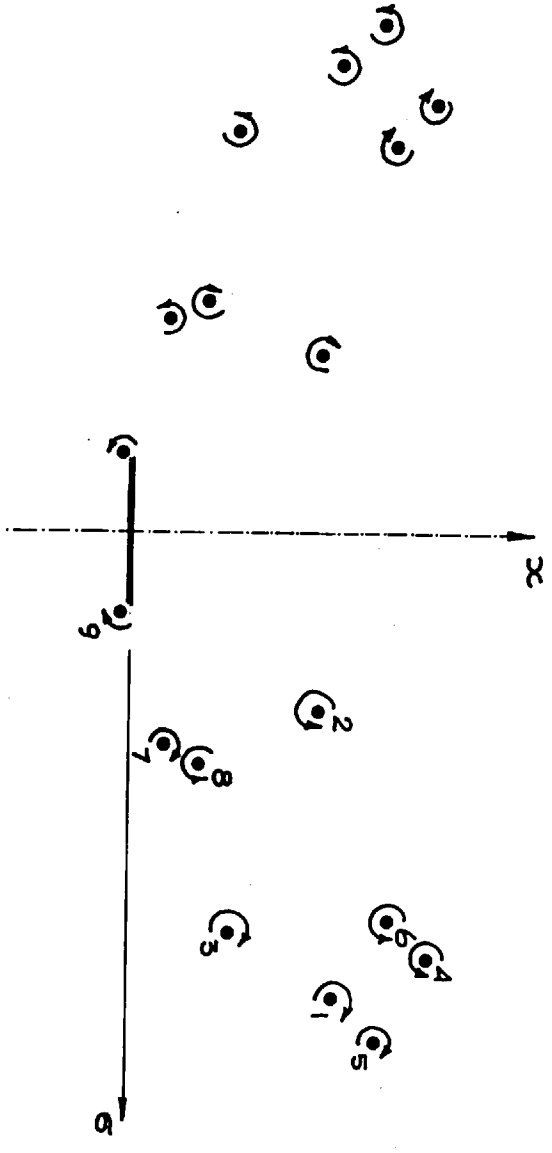

Fig. 4.11

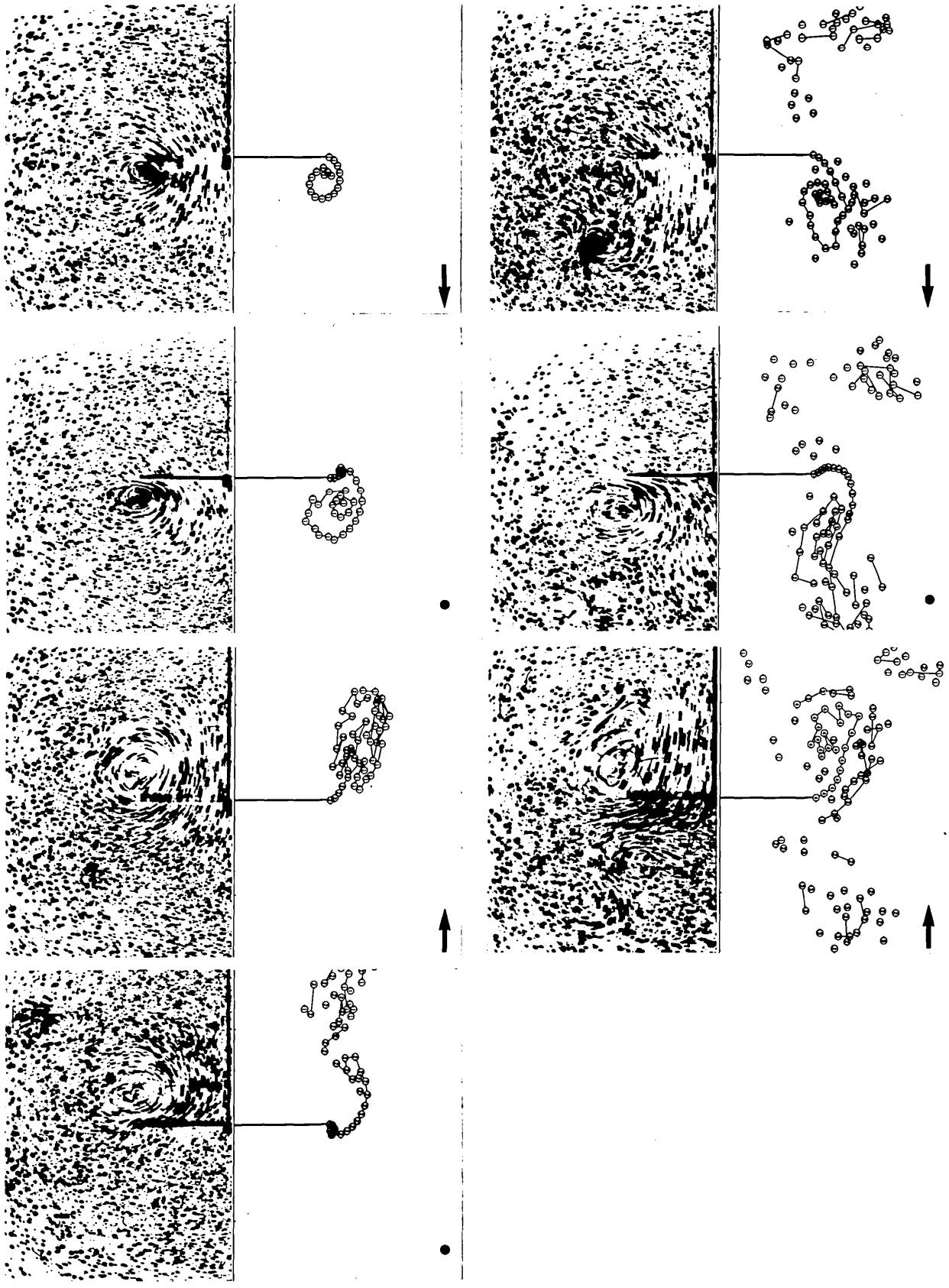

Fig. 4.12

The vorticity shed during the first half cycle tends to roll up into a single vortex ring. As the free stream slows down, the flow at the edge of the disc reverses and a second vortex sheet of opposite sign starts and continues to be shed during the second half of the cycle. Meanwhile, the first vortex is convected around the disc by both its self-induced velocity and by the reversed free stream. This vortex interacts with part of the second vortex sheet to form a vortex pair which moves away from the disc. The residual of the second vortex sheet is not as strong nor as organised as the first vortex and so when the flow again reverses at the start of the second cycle it does not interact very strongly with the third vortex. This third vortex sheet develops into an organised vortex ring very much like the first one and the process is repeated in succeeding cycles.

The predicted formation of vortex pairs and their unidirectional convection away from the disc, were observed in the experiments. The asymmetric wake whose direction depended only on the starting direction of the flow was certainly established and seemed to be quite stable. The flow was observed to be axisymmetric to a distance of about one diameter from the disc. Because of diffusion and possibly instabilities of the vortices, it was difficult to follow their motion at greater distances. Also, because the tank was relatively small, a secondary motion was rapidly established which also obscured the long-term motion.

The pattern of the flow is closer to that observed for a single, 2-D edge (Graham, 1980), then that of double

edged body. In the latter case, the vorticity from one edge tends to migrate around the body to join with the vortex of the same sign growing on the opposite edge. This process appears to revolve around the body with the vortex pairs convecting away from the edges at an angle of about 45^{o}. Because of the axisymmetry of the disc flow, this cannot happen.

Results of calculations for K = .5, 1, 2, 3, 5 are shown in Figs. (4.13), (4.14), (4.15), (4.16), (4.17), where the time is shown by the small clock in the lower right corner of each frame. At the end of each velocity cycle the pointer is at the 12 o'clock position. For K = 0.5, the displacement of particles in the undisturbed flow is small compared to the scale of the body and the flow behaves truly like a 2-D one. However, for K = 5 the large scale rolled up vortices move very far from the edge of the disc and even if there is not a radical change of the flow patterns, the rolling up process during half a cycle shows close resemblance to the corresponding steady free stream situation (Section 4.1). This suggests that the flow is not very far from a new regime ($K>K_c$) and that K_c is smaller in the disc case than in the 2-D case ($K_c \sim 20$).

We conclude this section with a comparison in Fig. (4.18) between two calculations where, for the case (a), the vortex rings have not been amalgamated whereas for the case (b) the amalgamation process has been used (M = 3). They are for the same case and the same time step $\delta\tau$=.0875. In general, the gross features of the flow, such as the predicted centres of circulation, are similar in both cases. However, as discussed in section 3.4, amalgamation obliterates some finer features of the flow and eventually could lead to unrealistic representation of the flow.

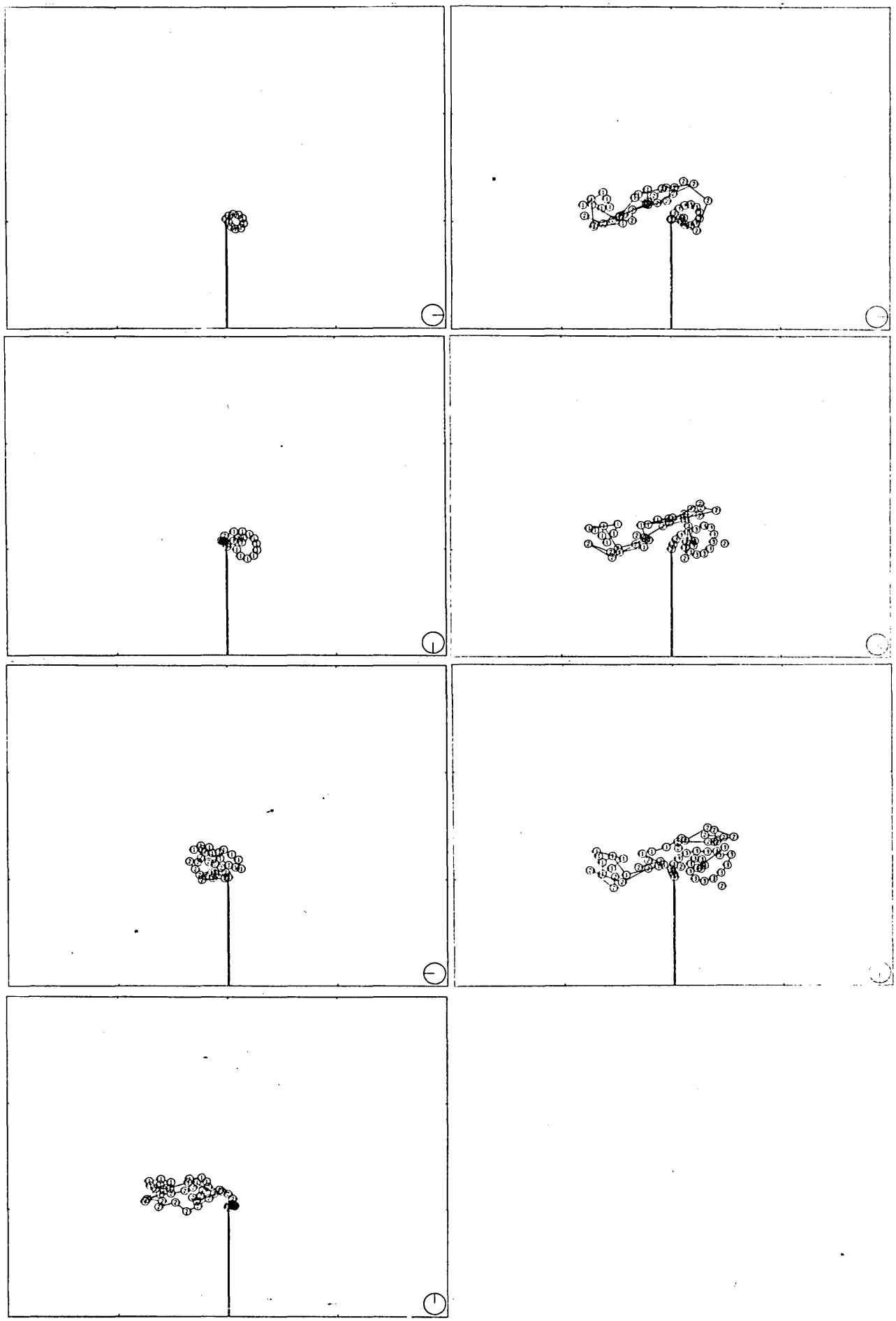

Fig. 4.13

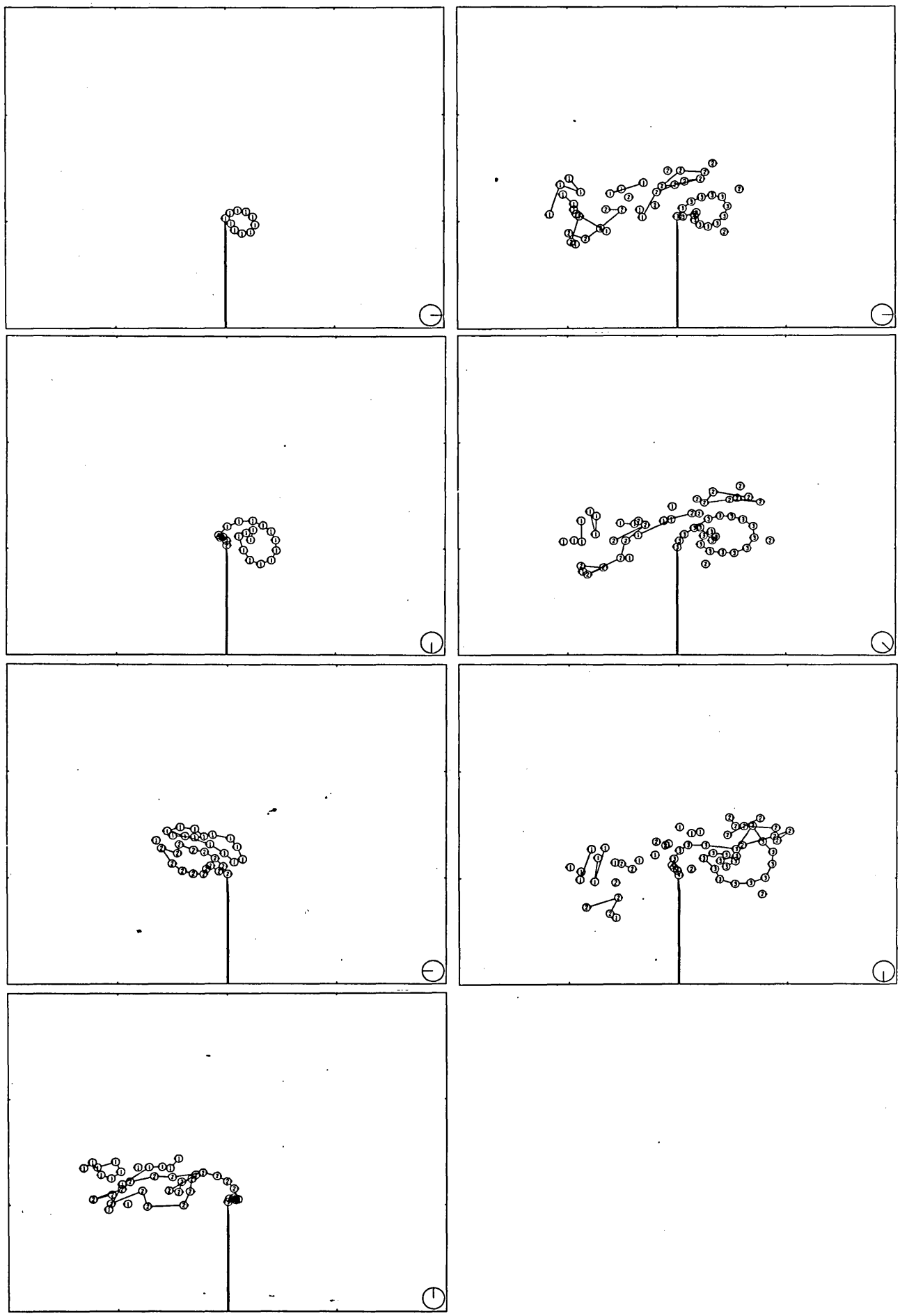

Fig. 4.14

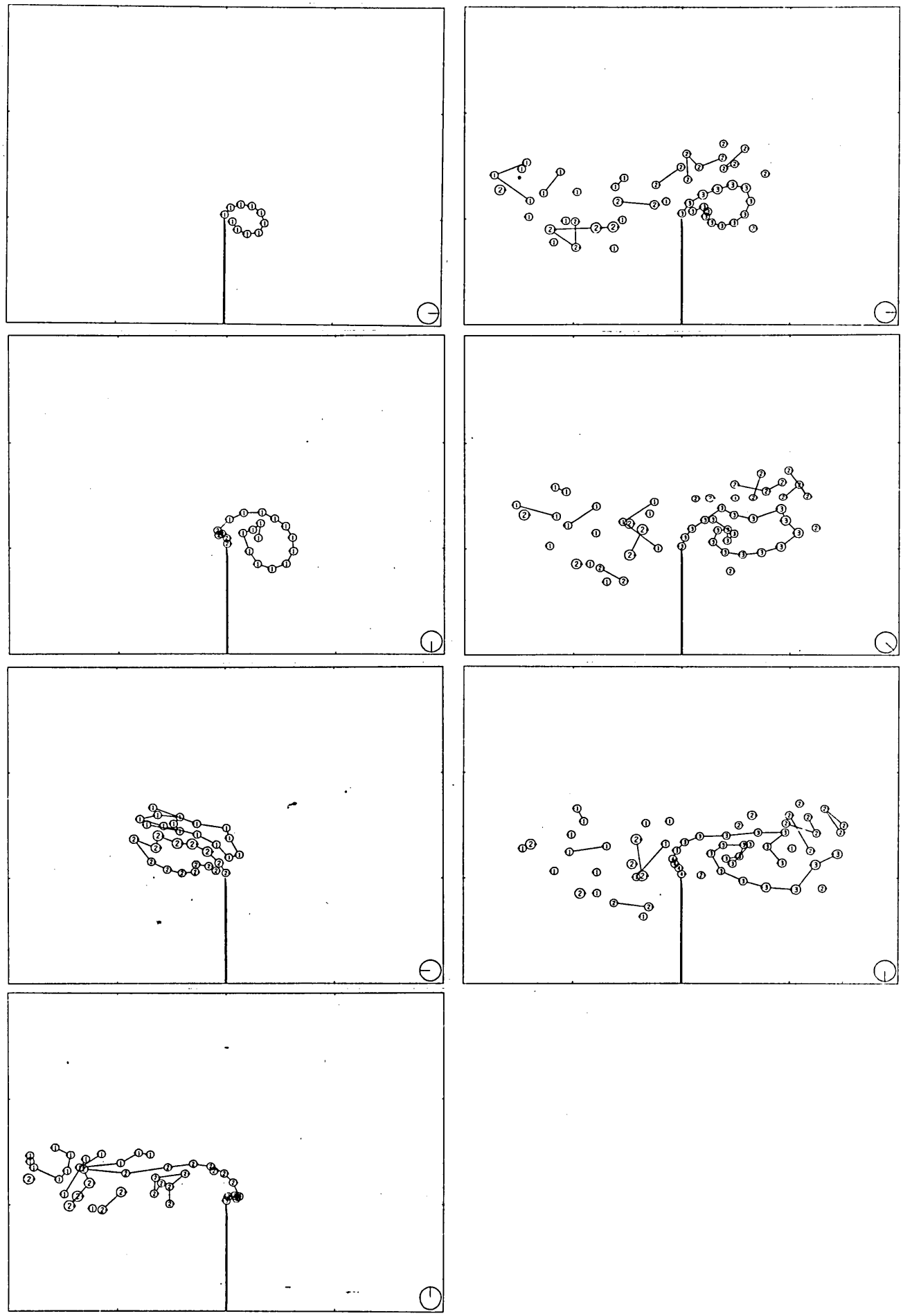

Fig. 4.15

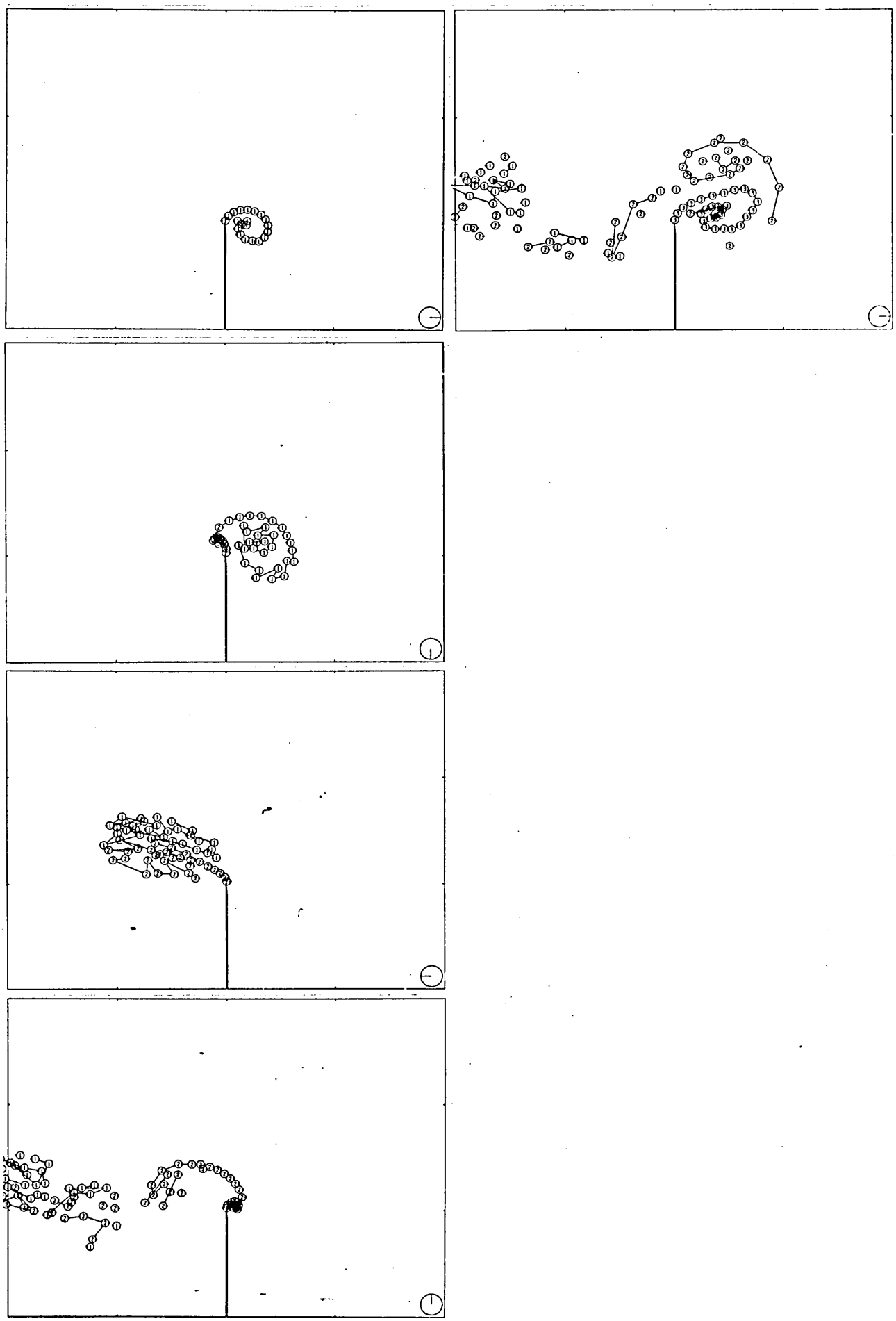

Fig. 4.16'

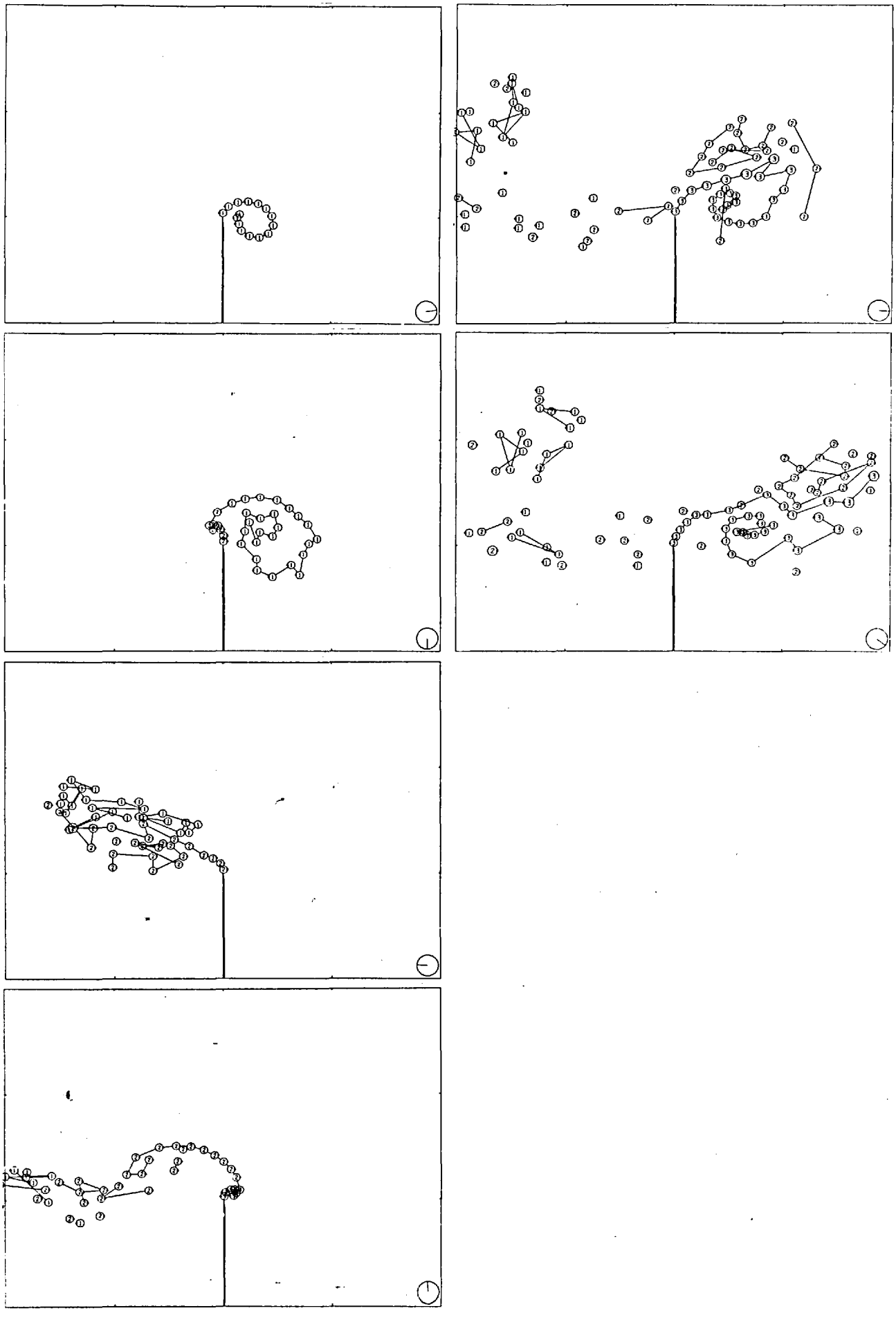

Fig. 4.17

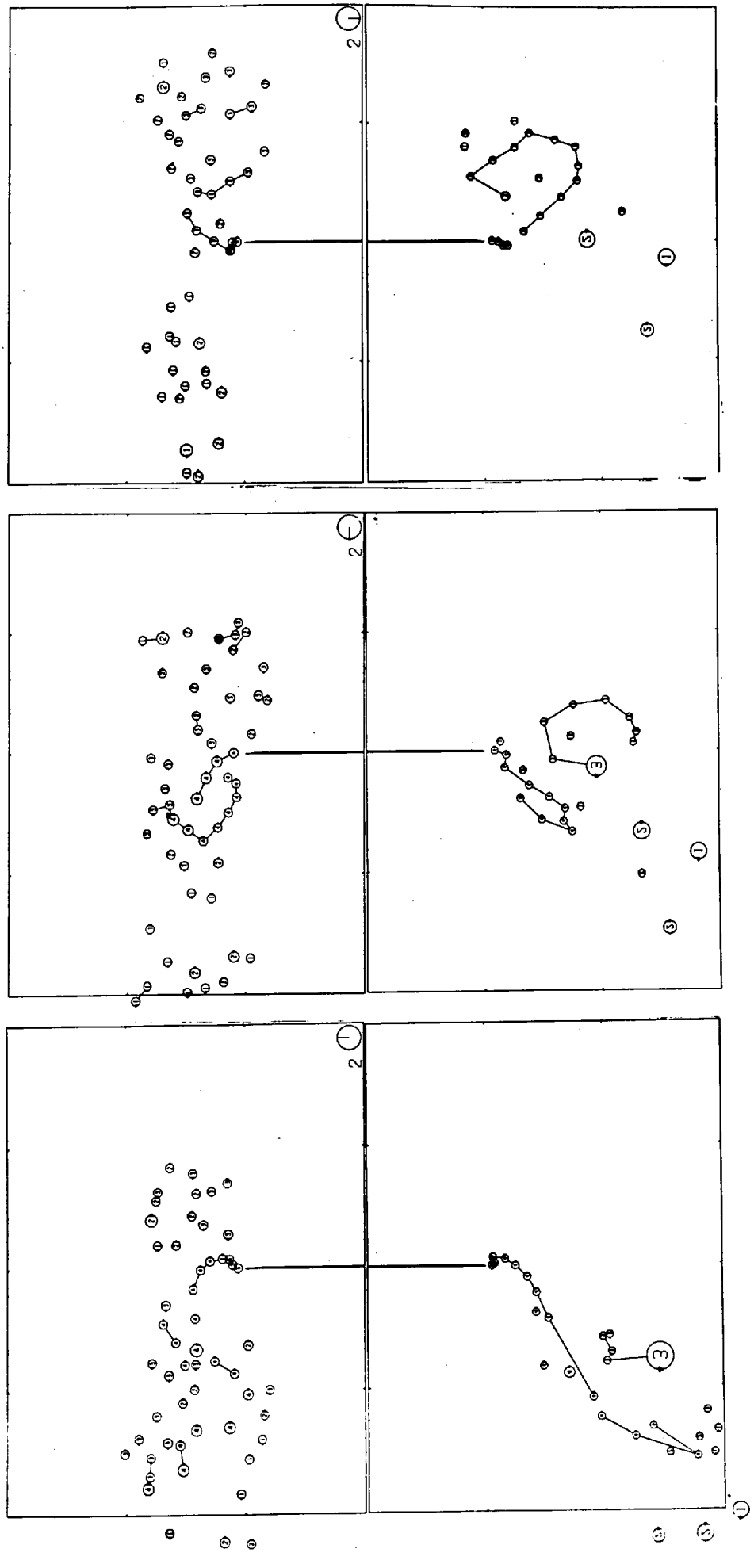

Fig. 4.18

5. UNSTEADY FLOW THROUGH SHARP-EDGED ORIFICES

In this chapter we apply the discrete vortex calculation procedure to a flow which has many similarities with the flow of blood through a constricted section of an artery: the internal, unsteady flow through a circular, rigid pipe of radius R* with a sharp-edged orifice of radius Ro* and length L_s. In general arterial blood flow is highly unsteady and its wave form is different for different arteries. In the large vessels it can be modelled by the pulsatile flow

$$U = U^*/U_o^* = 1 + \gamma \sin 2\pi\tau \qquad (1)$$

where $\tau = t^*/T^*$ and $\gamma = \hat{U}^*/U_o^*$ is the pulsatility index. In these arteries both inertial and viscous effects are important.

FOR OSCILLATING FLOWS

There are at least two governing parameters: the Keulegan-Carpenter number, $K = \hat{U}^* T^*/R^*$, and either the Reynolds number, $R_e = 2R^*\hat{U}^*/\nu$, or the frequency parameter $\alpha = R^*[2\pi/\nu T^*]^{1/2}$. Alternatively, the Strouhal number $S_t = 4\pi R^*/\hat{U}^* T^*$ could be used instead of K. Both Re and α vary over a wide range in the circulatory system with typical values $.001 \leq Re \leq 10000$ and $.01 \leq \alpha \leq 20$. However, in the large arteries $100 \leq Re \leq 2000$ and $1 \leq \alpha \leq 20$.

The geometry of stenoses found in living systems is complicated, variable and difficult to characterise The variables which play the most important role are the size and the length of the stenosis. Following clinical medical practice, the stenosis size is expressed by the

constriction ratio; i.e. the fraction of pipe area blocked by the orifice. For our axisymmetric orifices, $C = 1-(R_o/R)^2$ The general problem is not amenable to an analytical solution and numerical solutions by conventional means can be obtained only for mild constrictions or low Reynolds numbers.

Different flow regimes may develop in blunt, streamlined stenoses. If the Reynolds number is sufficiently small ($\sim Re < 20$) the flow will be laminar throughout and separation will not occur. As the Reynolds number is increased, the mainstream will separate from the boundary and, subsequently, reattach at some point downstream. The separated region will contain a slowly moving mass of fluid, but the overall flow remains laminar. Daly (1977) made numerical calculations of pulsatile flow through a stenosed canine femoral artery. Stenoses that in cross section had the shape of a circular arc were simulated for values of constriction ratio varying from .0 to .61. He found that separation starts during the accelerative phase of systole when the instantaneous Reynolds number reaches a value of about 180 (Re_c). The separated region grows in extent with time and the separation point attains a quasi-steady position slightly downstream from the centre of the obstruction. During the diastolic phase the mean flow is reversed and a separated region develops on the other side of the obstruction. A comparison between the critical Reynolds number Re_c so calculated and the experimental Re_c obtained by Golia and Evans (1973), for steady-flow regime,

and shown in fig. (5.1), suggests that separation may be delayed in an accelerated flow. Therefore comparisons between steady and unsteady flow can be highly misleading.

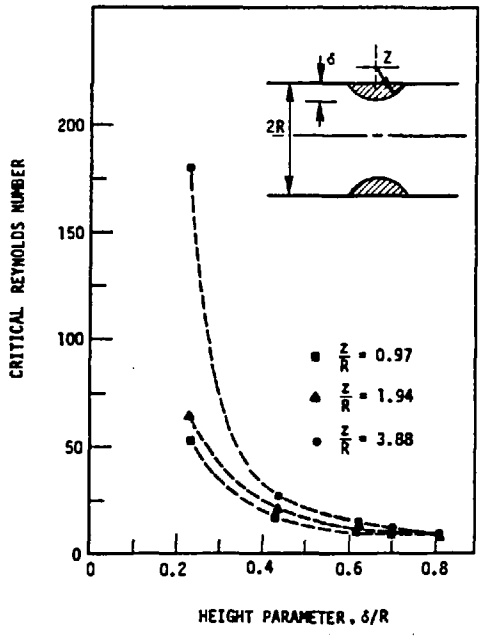

Fig. 5.1

With a still further increase of Re the shear layer separating, the mainstream and the separated bubble becomes stronger and eventually becomes unstable and jet-like large scale coherent structures appears in the flow field. These are usually referred to in the literature as perturbations arising from the instability of the previous flow regime, but in general they present high regularity and this type of flow has been referred to as a disturbed flow intermediate between the laminar and turbulent regimes.

An increase in Reynolds number beyond this condition will lead to turbulence. The turbulence which develops in a stenosis will be transient and no clear demarcation exists between the disturbed and turbulent flow regimes. Khalifa & Giddens (1978) pointed out that, because of the pulsatility of the flow, the mean velocity of interest is usually not the average over a long time, but is rather the basic pulsatile waveform itself. This is such that many harmonics of the fundamental heart rate are present so that flow disturbances may be difficult to distinguish. Furthermore, the basic velocity waveform is not strictly periodic and each heartbeat may be different. This biological disorder

is due to the heart which is not a perfect pump and to the difficulty of maintaining a constant physiological status for a long time. For such flows, they have shown that periodic disturbances exist which are often hidden by the turbulence. This seems to be caused by the presence of a jet-like vortex shedding.

Cassanova & Giddens (1978) in investigating the stenotic flow patterns found strong similarity between free and stenotic jets. The presence of the pipe wall causes the systems of discrete vortex rings to break down at a shorter distance from the constriction than in the free jet case. The influence of the wall on the initial formation of vortex rings and their break-up into turbulence is less pronounced for severe constrictions where the stenotic jet is farther away from the wall. The growth of the shear layer and its instability approaches more and more the behaviour of the free jet. They showed that in the case of steady flows the stenosed jet exhibits a Strouhal number of the vortex shedding frequency which ranged between 1 and .6, which agrees with the free jets values (Beavers & Wilson, 1970). In the case of pulsatile flows, the energy spectrum of the velocity, which measures the kinematic energy distribution over the disturbed flow frequencies, indicates that discrete vortex shedding is occurring over a significant part of the flow pulse. Fig. (5.2) (redrawn from Cassanova & Giddens, 1978) shows a comparison between the energy spectra measured at $x^*/R^*=1$ for a sharp edged stenosis with c = .5 and for different radial

positions, in the case of steady and pulsatile flow. The frequency of the vortex shedding agrees quite well in the two cases. They also observed that more abrupt, sharp-edged stenoses created a much greater flow disturbance at a given Reynolds number than the smoothly contoured configuration, however both present the same qualitative flow features.

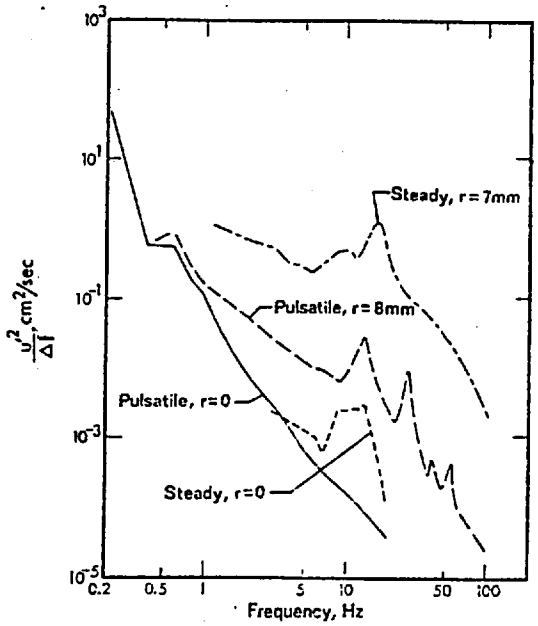

Fig. 5.2

The velocity fluctuations due to the presence of large eddies produce pressure variations at the arterial wall which propagate through the wall and the surrounding tissues and generate sounds, whose auscultation is the oldest and most common means of detection of arterial stenoses. Tomm (1977) IN VITRO showed that such sounds have peak frequencies which correlate with the characteristic vibration modes of the ~~arterial~~ TUBE wall. Only in the case of sharp-edge stenoses did he find frequencies which correlated with the periodic vortex shedding. Even then, the vortex shedding frequency might easily have been "forced" by the wall elastic vibrations. This forcing has been observed in the case of an unbounded subsonic jet by Crow & Champagne (1971) and by Moore (1977). Acton (1980) showed by numerical calculation that this forcing is possible over a wide range of the Strouhal number ($.3 \leq S_t \leq 2.$). However, no experimental evidence exists to support this observation for high Reynolds number flows.

Several experiments have shown that the transition to turbulence is strongly dependent on the constriction ratio C ; that it varies with the frequency parameter, the flow first becoming less stable and then more stable as it is increased; and that it depends on the shape of the obstruction. However, no general conclusions can be made because of the lack of agreement among investigators Only in the case of a pulsatile flow through an orifice plate stenosis can more information be obtained. Sacks et al(1971) found that the dependence on the constriction ratio could be expressed as

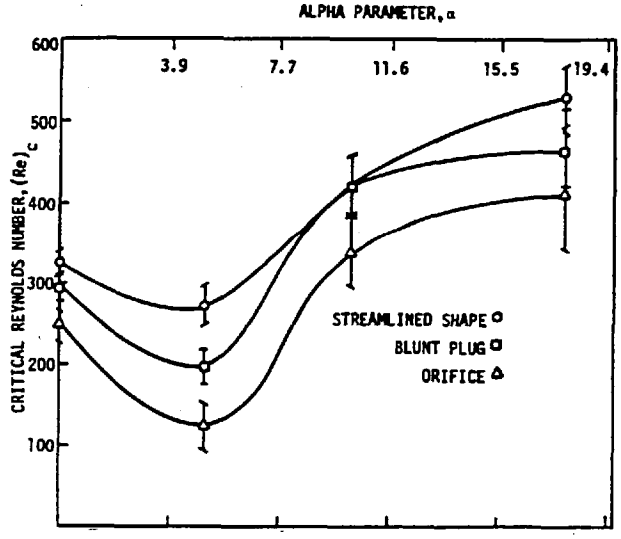

Fig. 5.3

$$R_{e_c} = 2384(1-C) \qquad (2)$$

and Yongchareon (1977) investigated the dependence on the α parameter for severe stenoses (c = .89). His results are shown in fig. (5.3).

The inviscid model of an orifice plate in a pipe previously described is a considerable simplification of the stenosis problem. However, because the geometries chosen are such that the flow separates for all Reynolds numbers and the separation point is fixed, we hope to obtain information about the evolution of the large scale structures and predictions of the gross features of the flow. Perhaps the grossest assumption is the flat incident flow profile. In the case of internal flow, the viscosity strongly effects the flow far from the stenosis. For a sinusoidally

oscillating viscous flow in a straight pipe of length 1 and subjected to the pressure gradient $\Delta p/\rho l = \hat{U}\cos 2\pi\tau$ the analytical solution of the Navier-Stokes' equation was given by Lambrossy (1952). This flow, later studied by Womersley (1955), is a function of distance from the axis ϵ, of the non-dimensional time τ and of α only. The velocity profile shows a phase lead of the outer layers over the inner core of the fluid and a flow reversal occurs at the wall. As α is increased, the point of reversal gets closer to the wall and the central part of the profile is flattened. At higher α a Stokes layer of thickness $\sqrt{\nu T^*}$ appears at the wall. For $\alpha > 5$ the flat flow profiles is a good approximation over most of the cycle.

5.1 Flat plate orifice

The first case investigated was that of oscillatory flow ($U_o^* = 0$) through a flat orifice plate of zero thickness. The pipe and the orifice were simulated by 80 annular elements distributed over a length of 12 pipe radii on either side of the orifice. The elements were concentrated, as discussed in section (2.5), at the edge of the thin walled orifice plate whose junction with the pipe wall was smoothed out to avoid spurious solutions (Craggs & Mangler, 1971). The velocity near the sharp edge was found to behave like the flow through a circular orifice in an infinite plane and the tangential velocity round the edge agreed well with $V_t^* = U^*[2R^*/(R_o^* - 6)]/16$, the attached flow in such a case (Lamb, 1932), for c = .6, .7, .8, .9.

As in the disc case the vortex release and the

integration time steps were assumed to be the same to minimise the self-induced velocity error. Also, the vortices which reached the ends of the simulated pipe were removed from the calculations. Fig. (5.4), (5.5), (5.6), (5.7) show the results of numerical calculations for c = .6, .7, .8, .9 and $K = 4.75$. The non-dimensional time step was $\delta\tau = .0125$.

The primary difference between orifice and disc flow is that the self-induced velocity of the vortex rings, formed by the rolling up of the vortex sheet shed by the orifice, tends to convect them away from the orifice. This effect is opposed by the 'images' in the bounding pipe walls and therefore the ratio of the radius of the vortex to that of the pipe is important. Sheffield (1977) found that in a 2-D channel of unit width the self-induced velocity of a pair was the dominant effect if their separation was less than 1. He also found that a vortex pair which is in close proximity to the wall of an orifice of width R_o will travel back through the orifice opening only if its initial distance from the wall is less than R_o/π . As a result, we see that very little of the vorticity generated during each half cycle is conducted back through the orifice, particularly for large constriction ratios. Most of it remains on the side of the orifice where it was generated. In the real flow the vorticity is dissipated by diffusion. In the calculation it does not dissipate but does disperse due to interaction with other vortices and with the wall. This leads eventually to strong interactions with the bound vortices representing the walls and as the free vortices approaches the end of the simulated pipe instabilities

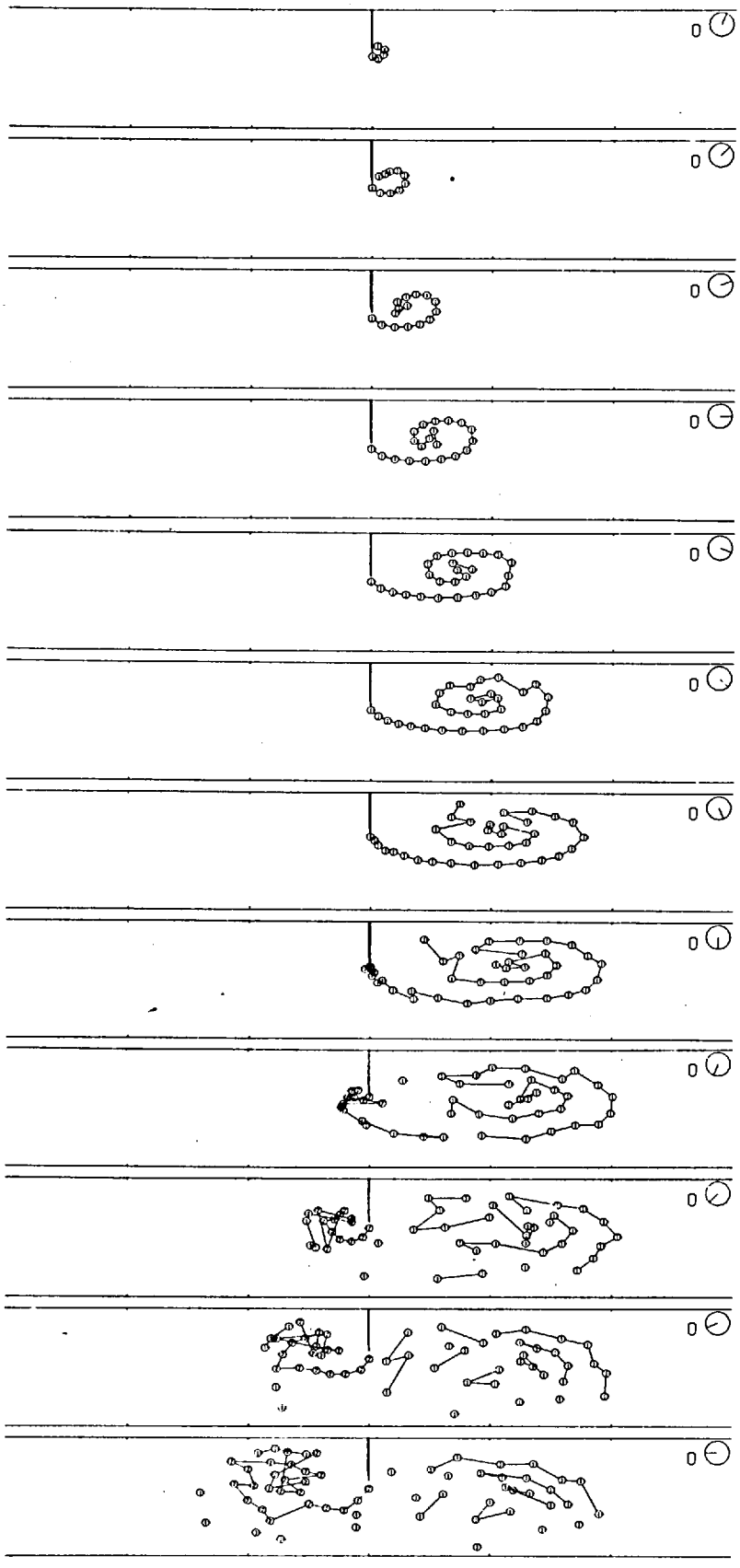

Fig. 5.4 (a)

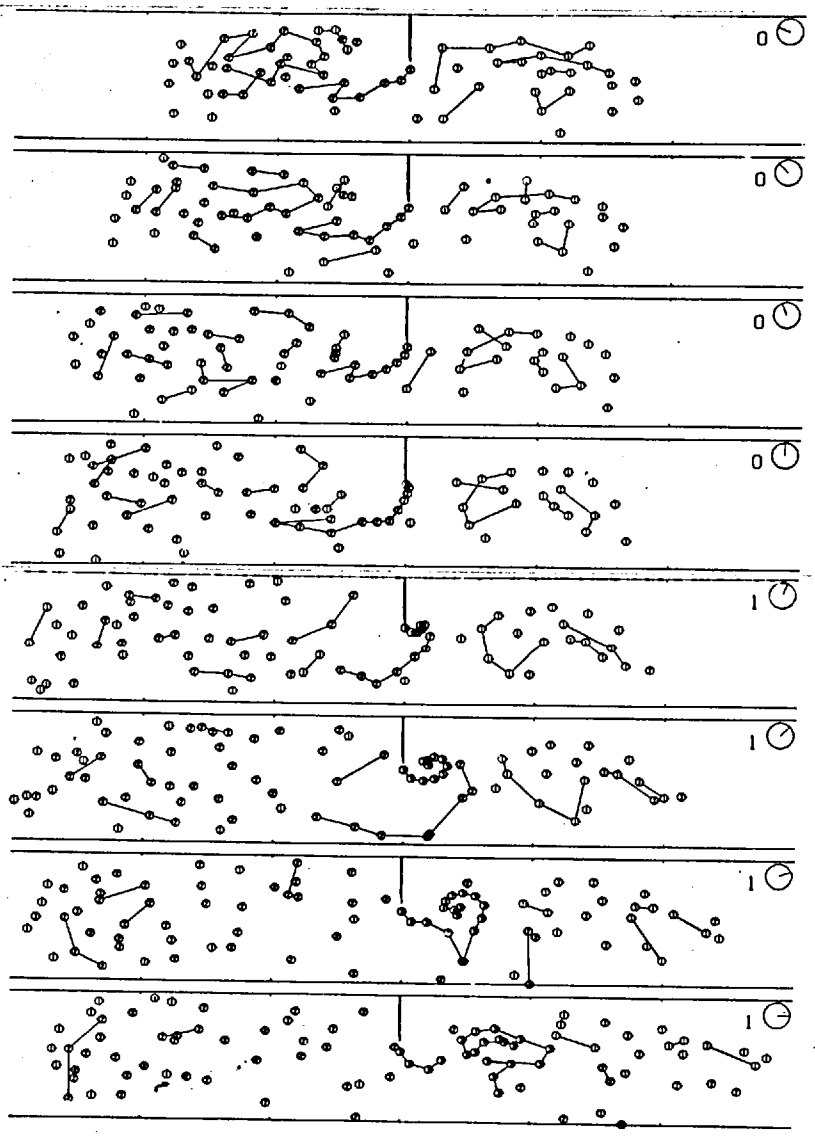

Fig. 5.14 (b)

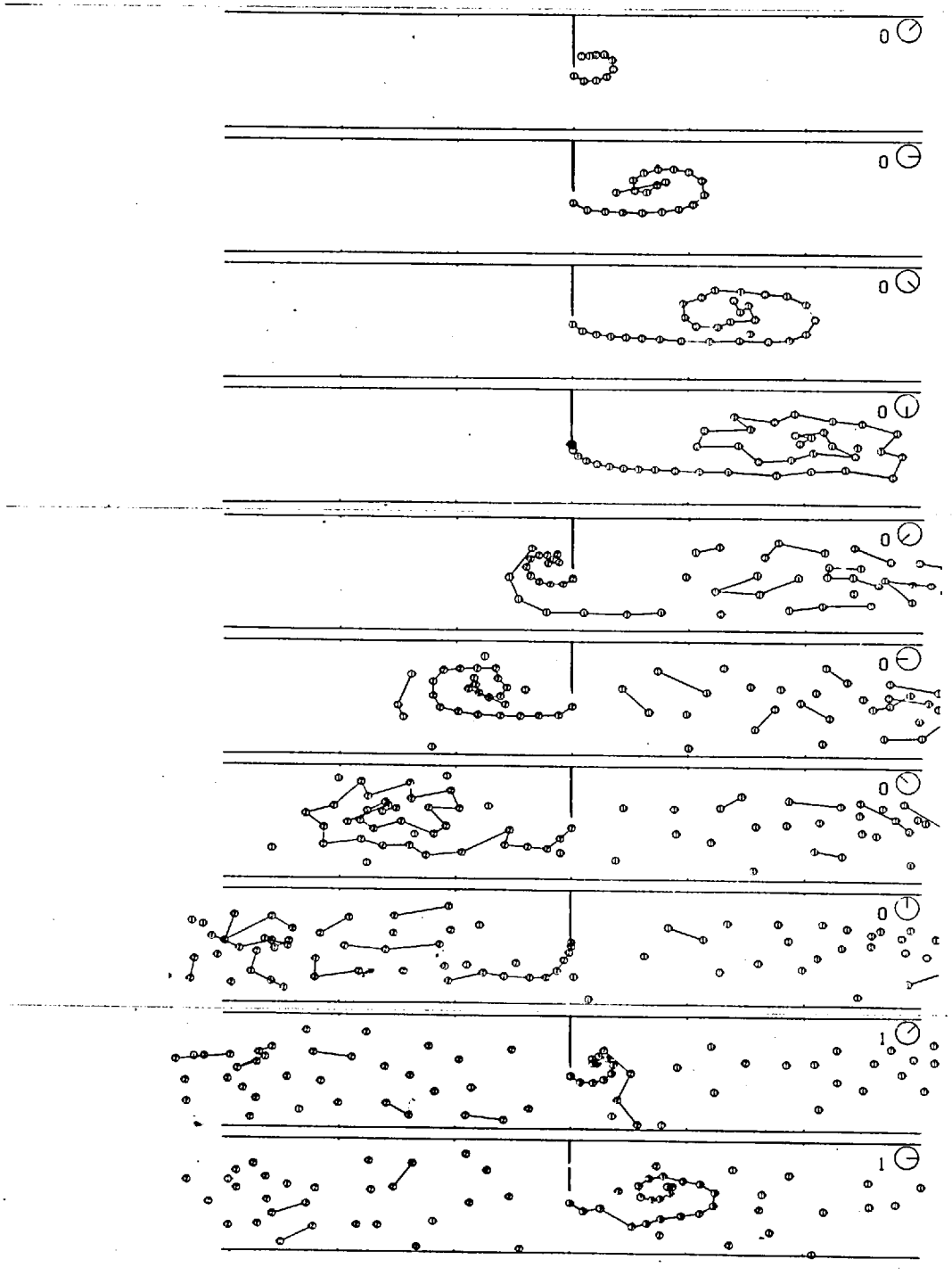

Fig. 5.5

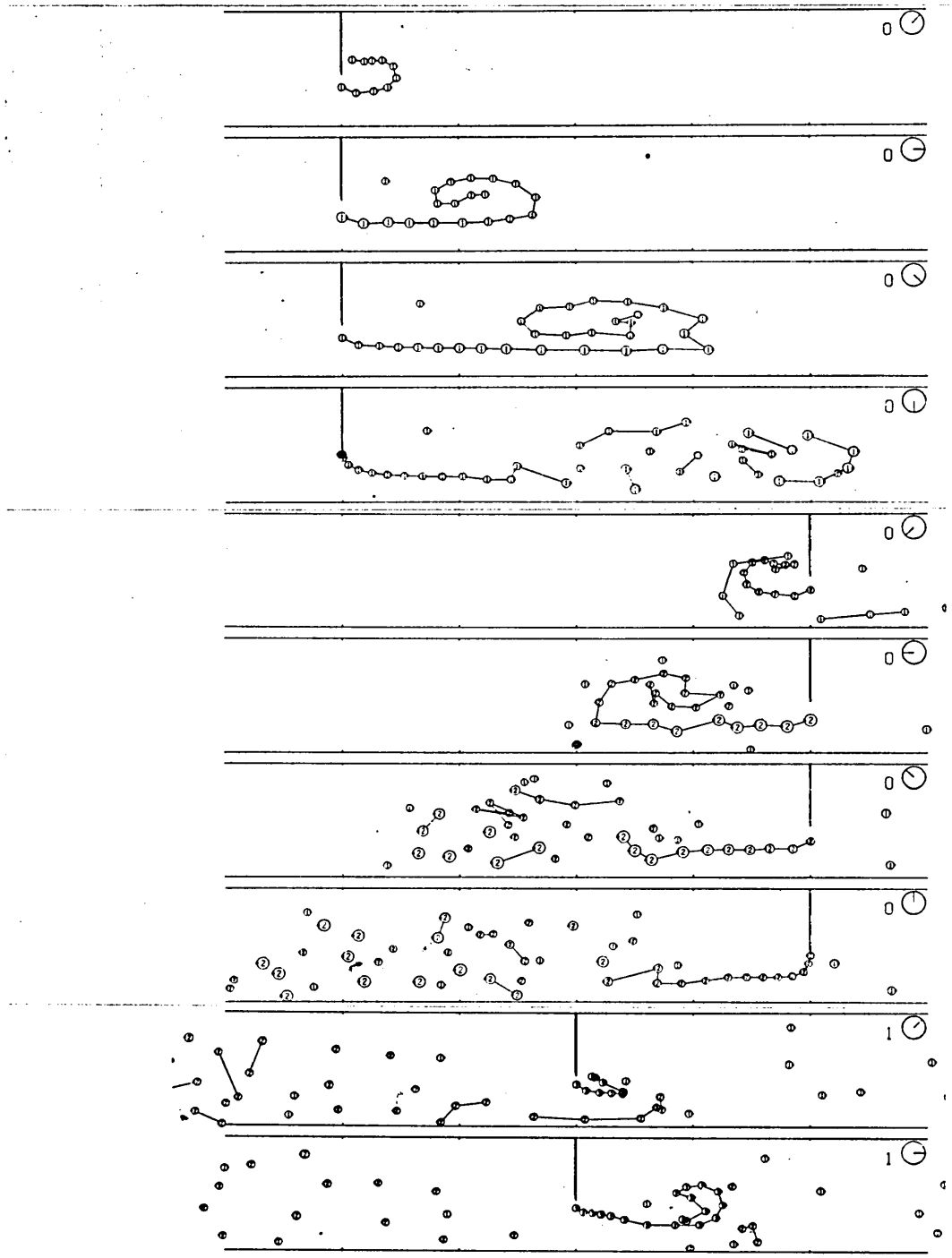

Fig. 5.6

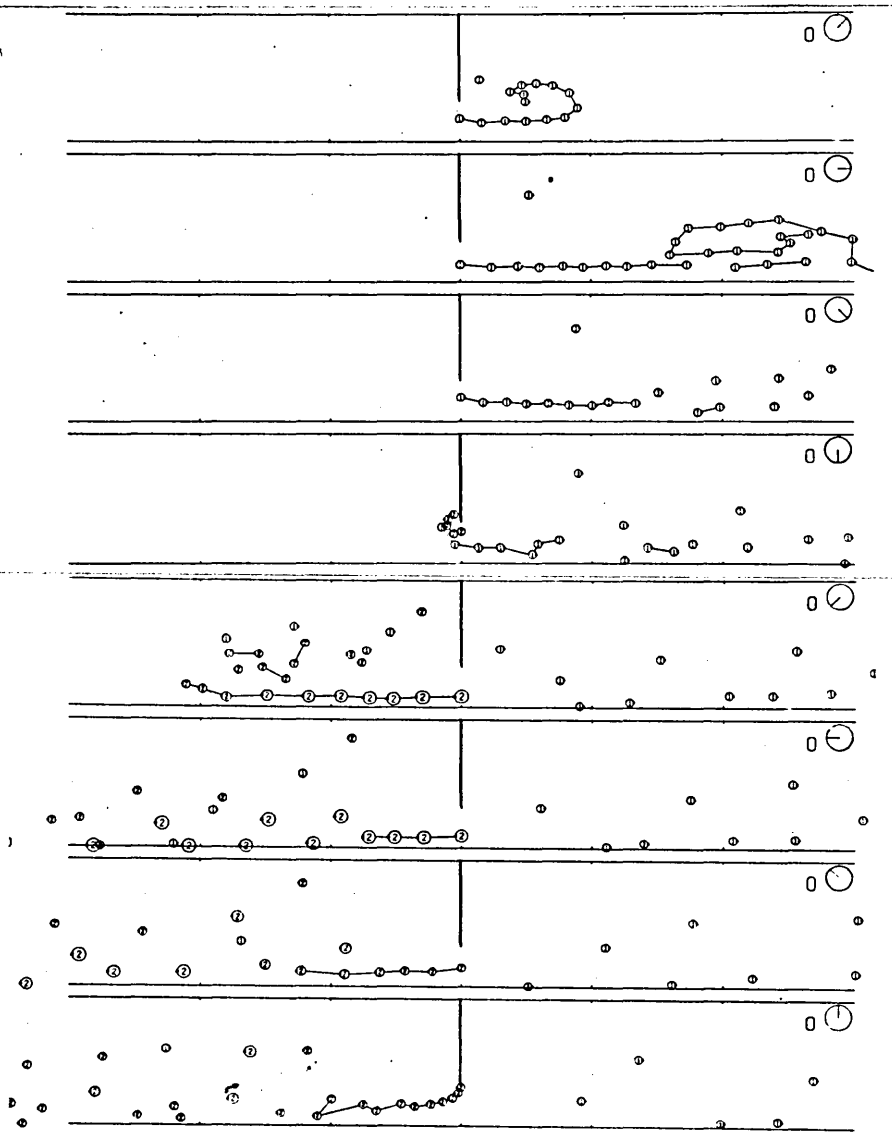

Fig. 5.7

may develop. This effect could have been avoided by removing the vortices too close to the walls (Clements, 1973; Sarpkaya, 1975) but we preferred to stop the calculations and assume that this was a limitation of the inviscid model.

Another difference between orifice and disc flow is how the flow in the neighbourhood of the edge is affected by the evolving vortex sheet. In both cases the velocity at the edge induced by the vortex sheet is opposite to the free stream velocity. As a result, the flow at the edge and hence the shedding tends to reverse before the onset flow reverses. In the orifice, however, this effect is counteracted by the self-induced velocity which acts with the incident velocity and the shedding reverses almost exactly in phase with the onset flow.

A flow visualisation experiment, using the hydrogen bubble technique, was performed to check the calculation. The experimental water rig consisted of a system of 25 mm I.D. perspex tubing. The oscillatory flow was produced by a piston, 44D downstream of the orifice plate, driven by an electric motor. The test section consisted of two 62.5 x 62.5 x 125 mm blocks of perspex with 25 mm I.D. bore. The stainless steel orifice plates of 1 mm thickness were located co-axially at the centre of the block. Five platinum wires ($d = 30 \times 10^{-3}$mm) were mounted .75 and 1.25D upstream of the orifice plate and .5, and 1 and 1.5D downstream. In order to produce hydrogen bubbles the two outer most wires to the plate were the anodes and the innermost ones the cathodes. Electrical pulses then produced either hydrogen or oxygen bubbles which were

convected with the flow. Two lamps illuminated the test section from above. Bubbles photographs of exposure (f 2.8, 1/250) were taken.

The experimental and calculated results for $K = 6.$ and $c = .7$ are compared in fig.(5.8) and fig. (5.9). The period of oscillation in the experiment is 4s which means that the Re = 486 and the ratio between Stokes layer and pipe radius is .16. Again the calculated results cannot be compared directly with the experimental results which record the convection of streak tracks. However, qualitative comparison can be made and, in particular, the centres of primary vorticity can be easily estimated from both and they agree quite well. The experiments as well as the calculations show the regular large scale structure of the flow. One vortex ring was observed to be shed for each half cycle which broke down into a disturbed flow pattern at the end of the accelerating phase. In the calculations this seems to be suggested by the Helmholz instability growing on the wound part of the vortex sheet. For the acceleration phase and a part of the deceleration phase the stretching of the vortex sheet increases at a rate faster than $\tau^{1/2}$. This stabilizes the sheet against a local Helmholz instability as discussed by Saffman (1974) and proved by Moore & Griffith-Jones (1974). At the end of half a cycle, the vortex sheet starts being compressed and then destabilized by the reversed free stream velocity. The same observations were made by Djilali (1978) who did not observe any quasi-steady vortex shedding for $2.4 \leq K \leq 7.2$ with $c = .5, .6, .7, .8, .9$ and by Pellegrin

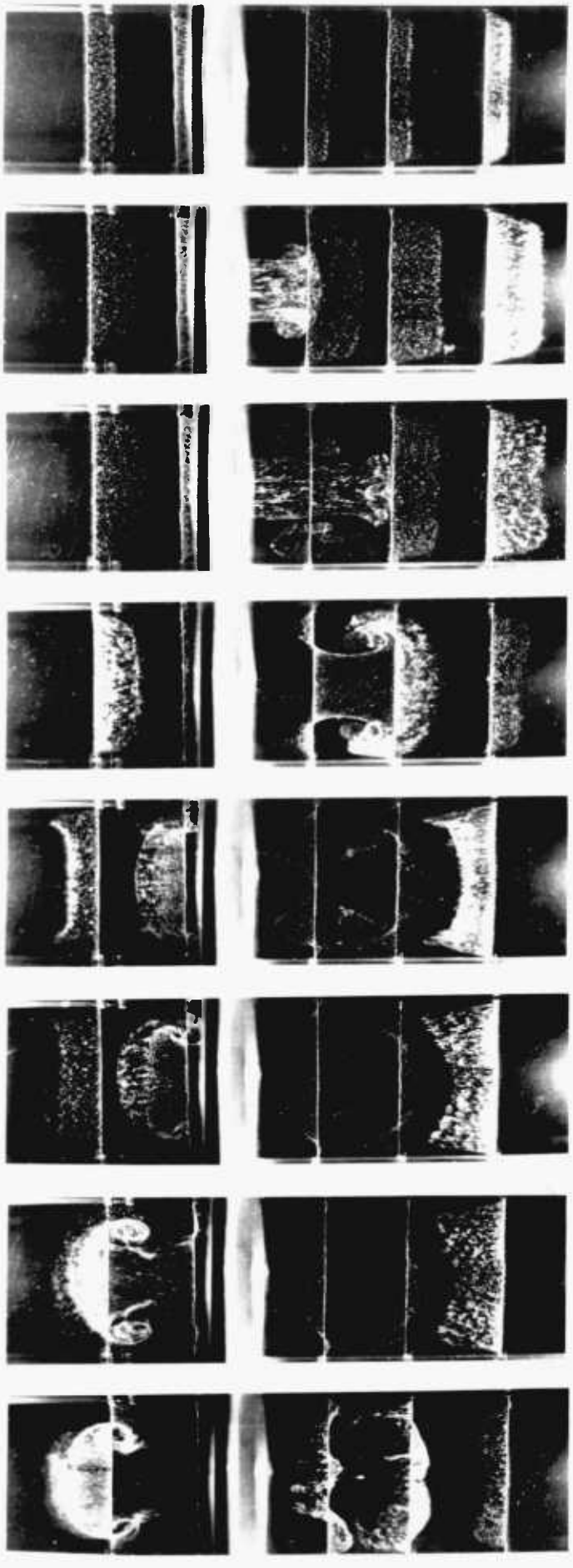

Fig. 5.8

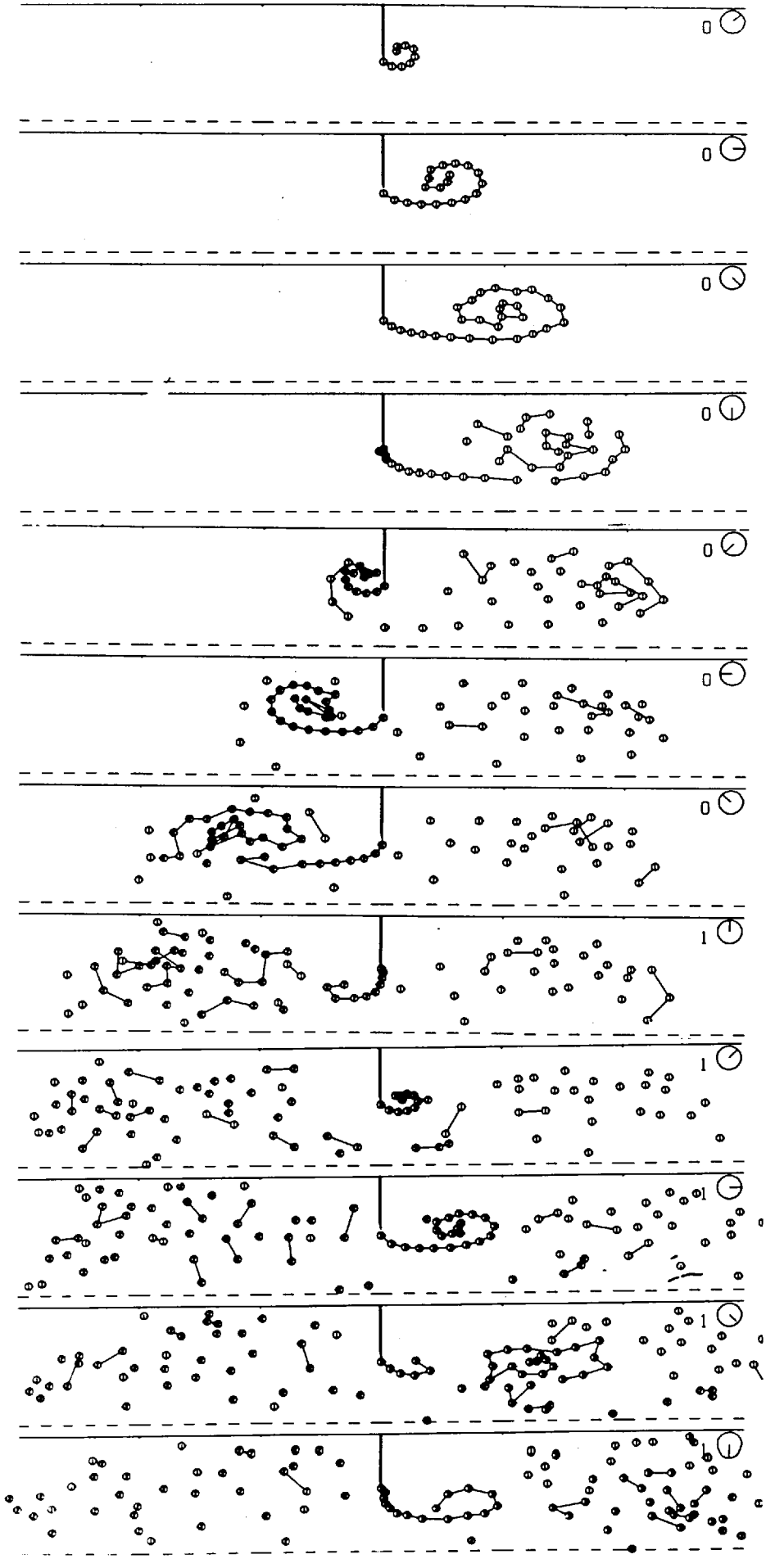

Fig. 5.9

(1976) who detected the vortex shedding only in the case of higher constriction ratios; in the latter case the effective Keulegan-Carpenter number is not given. In the case of a physiological pulsatile flow through an axisymmetric stenosis, Azuma & Fukushima (1976) observed that a few intense large vortices were formed near the constriction and shed downstream in a quasi-steady fashion during the acceleration phase. During the succeeding deceleration phase they were broken down into turbulence The turbulent flow thus formed did not diminish but spread upstream until the start of the next accelerating phase. The parameters were within the physiological range, Re = 1200, $\alpha = 22$ and $\gamma = 1$.

The pressure distribution along the wall is defined as in section (4.1) and the pressure drop coefficient is given by equation (4.1.16). We define the pressure drop coefficient between two points, s_1 and s_2 at the wall as

$$C_{\Delta p}(s_1, s_2, \tau) = C_p(s_1, \tau) - C_p(s_2, \tau) \qquad (3)$$

Fig. (5.10) shows the calculated and the experimentally measured (Djilali, 1978) values of $C_{\Delta p}$ when s_1 and s_2 are three pipe diameters either side of the orifice for $K = 7.4$, Re = 1118 and $\alpha = 22.5$, with c = .6, .7, .8.

In agreement with Young & Tsai (1973) and Clark's (1976) observations the experimental peak pressure drop coefficient $\hat{C}_{\Delta p}$ was found to be relatively independent of c for $c \leq .7$ and then to increase very rapidly with c. $\hat{C}_{\Delta p}$ was also found to be relatively independent of Re

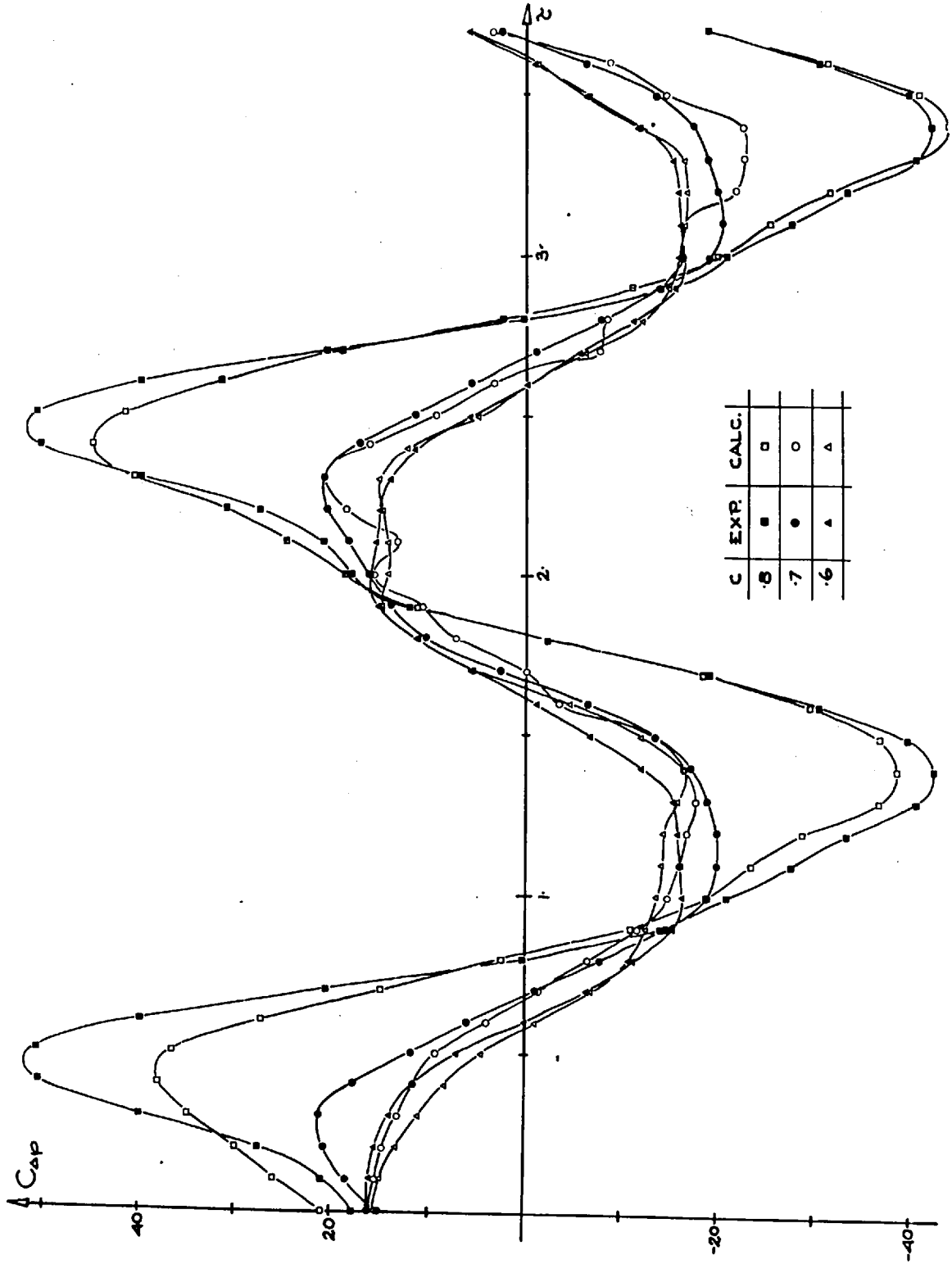

Fig. 5.10

over the range $318 \leq Re \leq 1272$ but did vary with K. These results are shown in fig. (5.11) along with the calculated. The agreement is good, as expected from the previous figures (5.10), for $c < .9$. This disagreement at $c = .9$ is not surprising; first because the flow was observed experimentally to be turbulent over most of the cycle and, secondly, because the assumptions leading to the use of the 2-d shedding theory and of a negligible self-induced velocity are suspect. For such a large construction, $L_v/\bar{s} \sim O(1)$ and equation (3.4.48) shows that $U^* \delta t^*/L_v = .65$

The instantaneous pressure drop can be written by simple momentum considerations

$$\Delta p^* = \rho L^* \dot{U}^* + \Delta^*_v \tag{4}$$

where (see section 4.2) the first term arises from the inertial effect of the unsteady flow in a straight tube over a length L* and the second term from the attached flow round the orifice and the distribution of shed vortices. In a non-dimensional form and using equation (1)

$$C_{\Delta p} = \frac{2\Delta p^*}{\rho \hat{U}^{*2}} = \frac{4\pi L^*}{KR^*} \cos 2\pi\tau + C_{\Delta v} = C_{\Delta o} + C_{\Delta v} \tag{5}$$

The calculated $C_{\Delta p}, C_{\Delta o}, C_{\Delta v}$ and the term $C_T = 2T^*_m/\hat{U}^{*2}\delta t^*$ are plotted in fig. (5.12) with $K = 4.72$ and $c = .7$. Also, $C_{\Delta v}$ and C_T are shown in figures (5.13) and (5.14) with $K = 4.72$ for $c = .6, .7, .8$ and in fig. (5.15) and (5.16) with $c = .7$ for $K = 2.45$, 4.72, 7.4. Fig. (5.17) shows $C_{\Delta v}$ and C_T with $c = .9$ for $K = 4.72$.

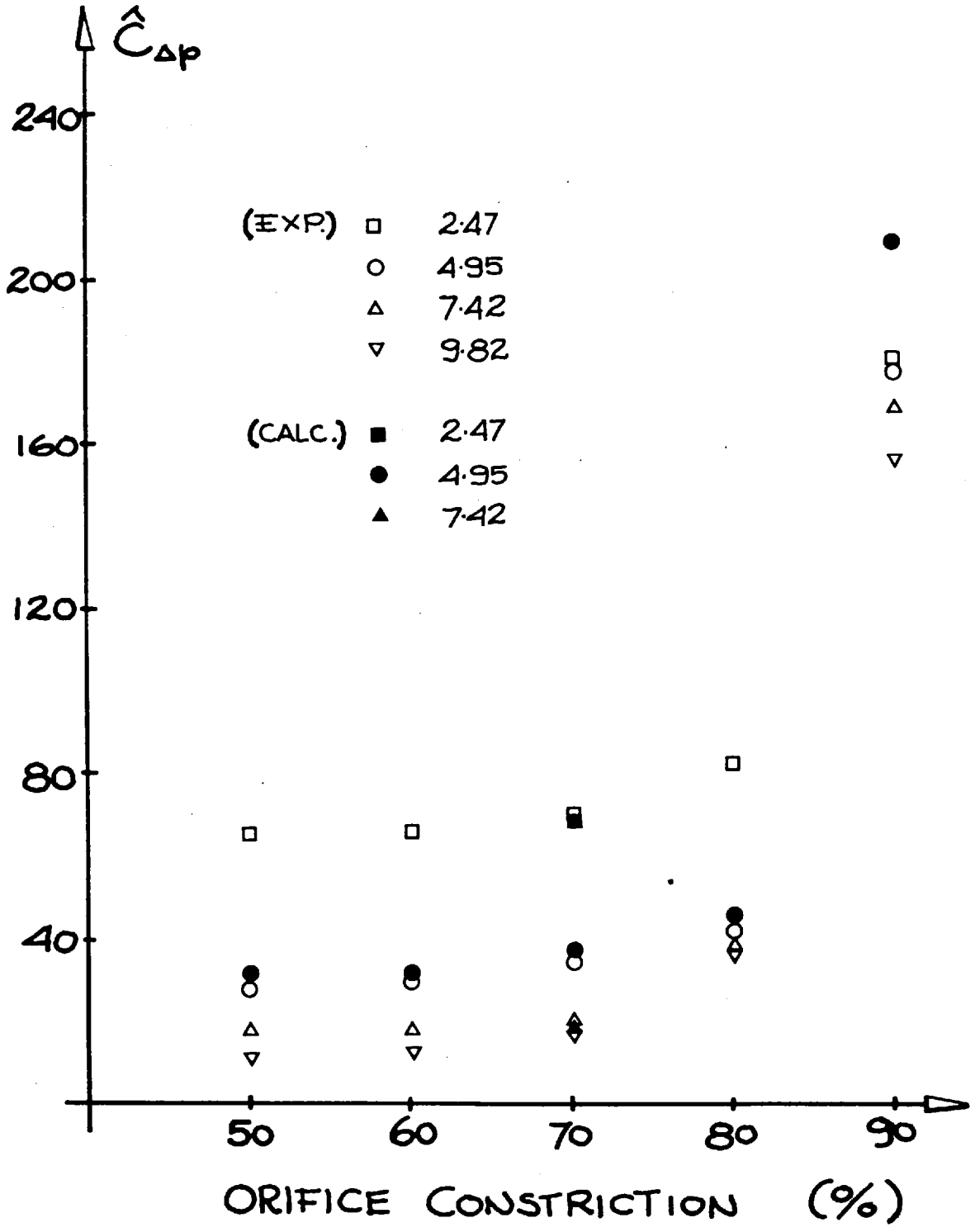
$\hat{C}_{\Delta p}$
240
200
160
120
80
40
(EXP.) 2·47
4·95
7·42
9·82
(CALC.) 2·47
4·95
7·42
50
60
70
80
90
ORIFICE CONSTRICTION (%)

Fig. 5.11

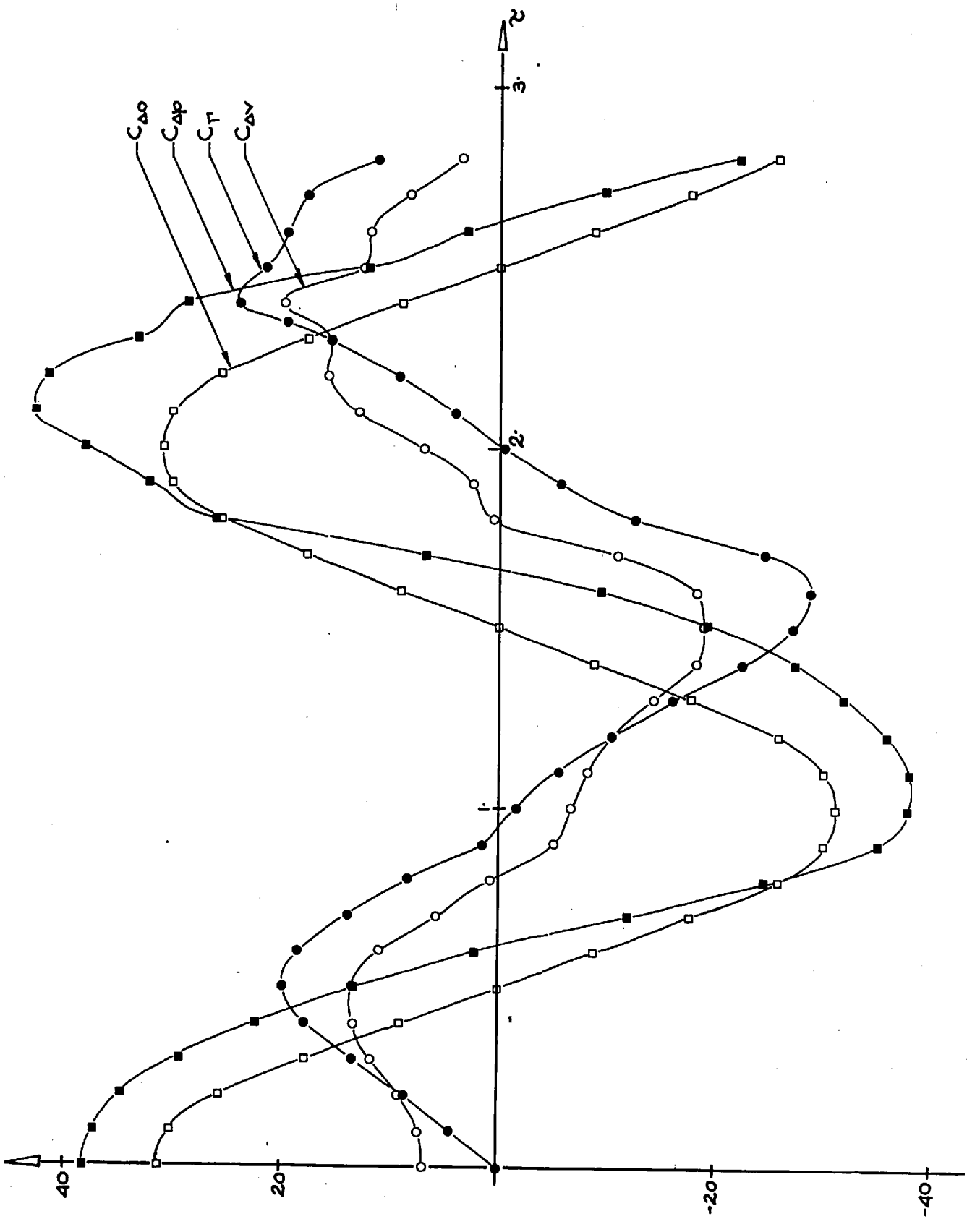

Fig. 5.12

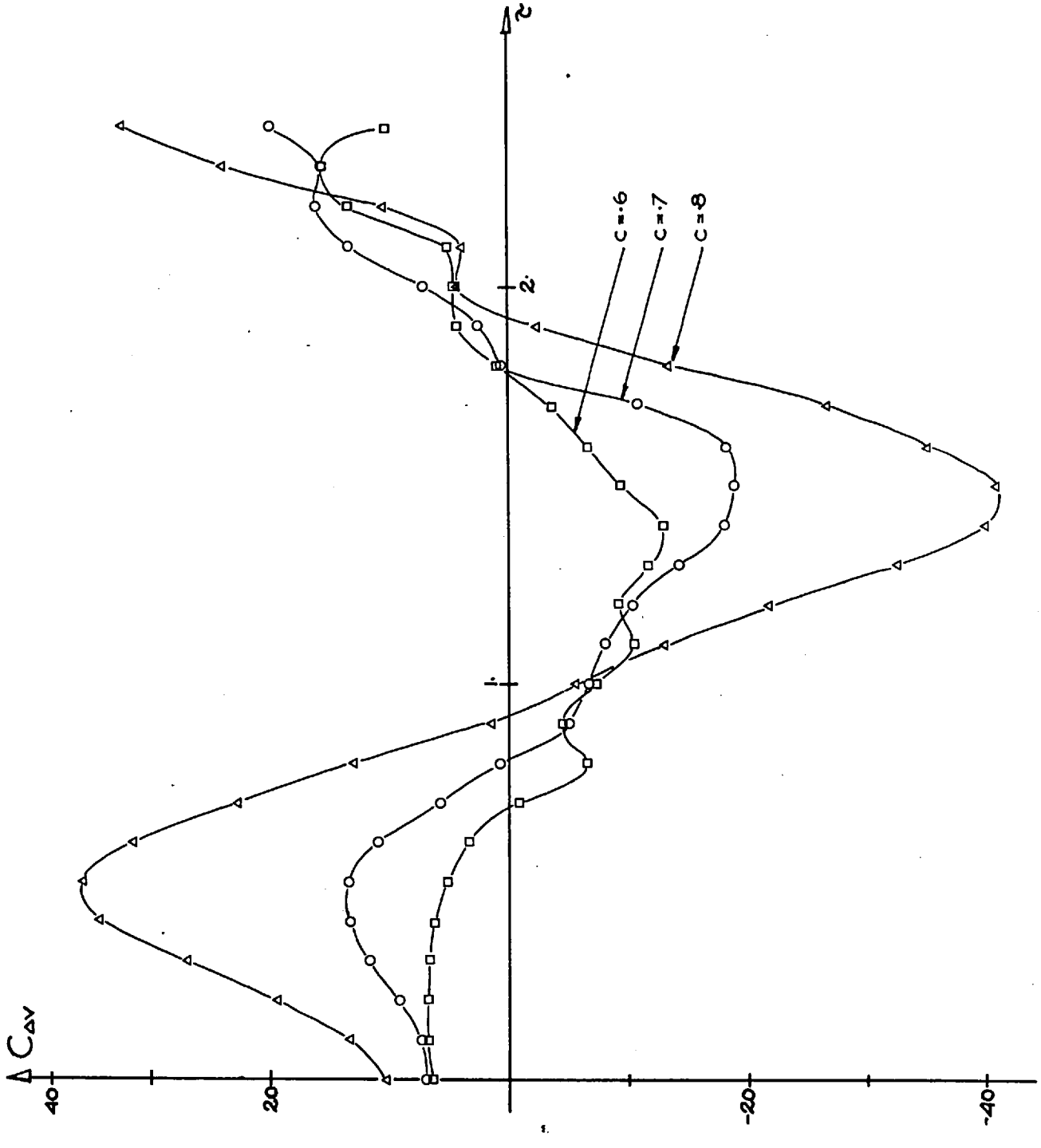

Fig. 5.13

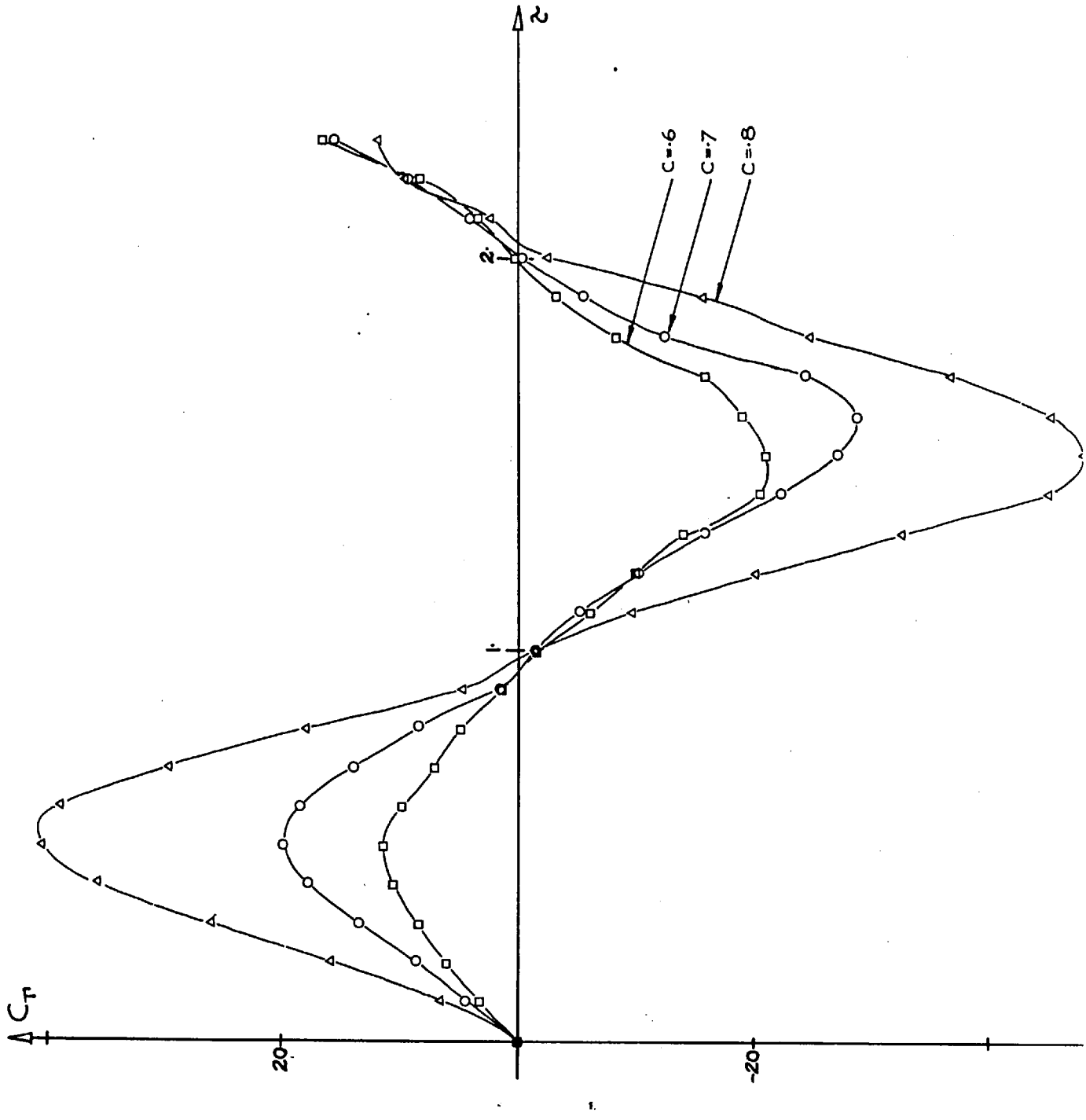

Fig. 5.14

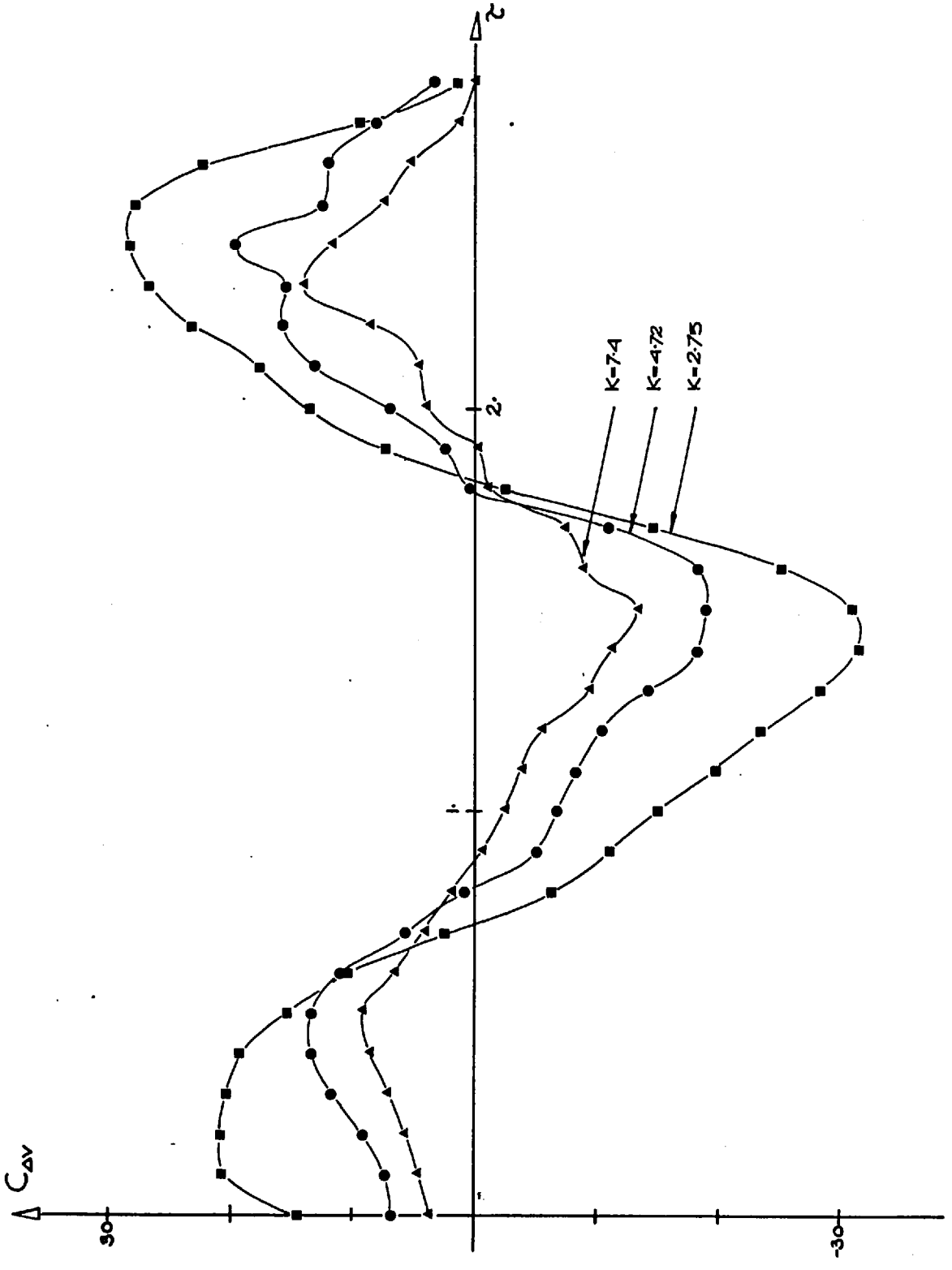

Fig. 5.15

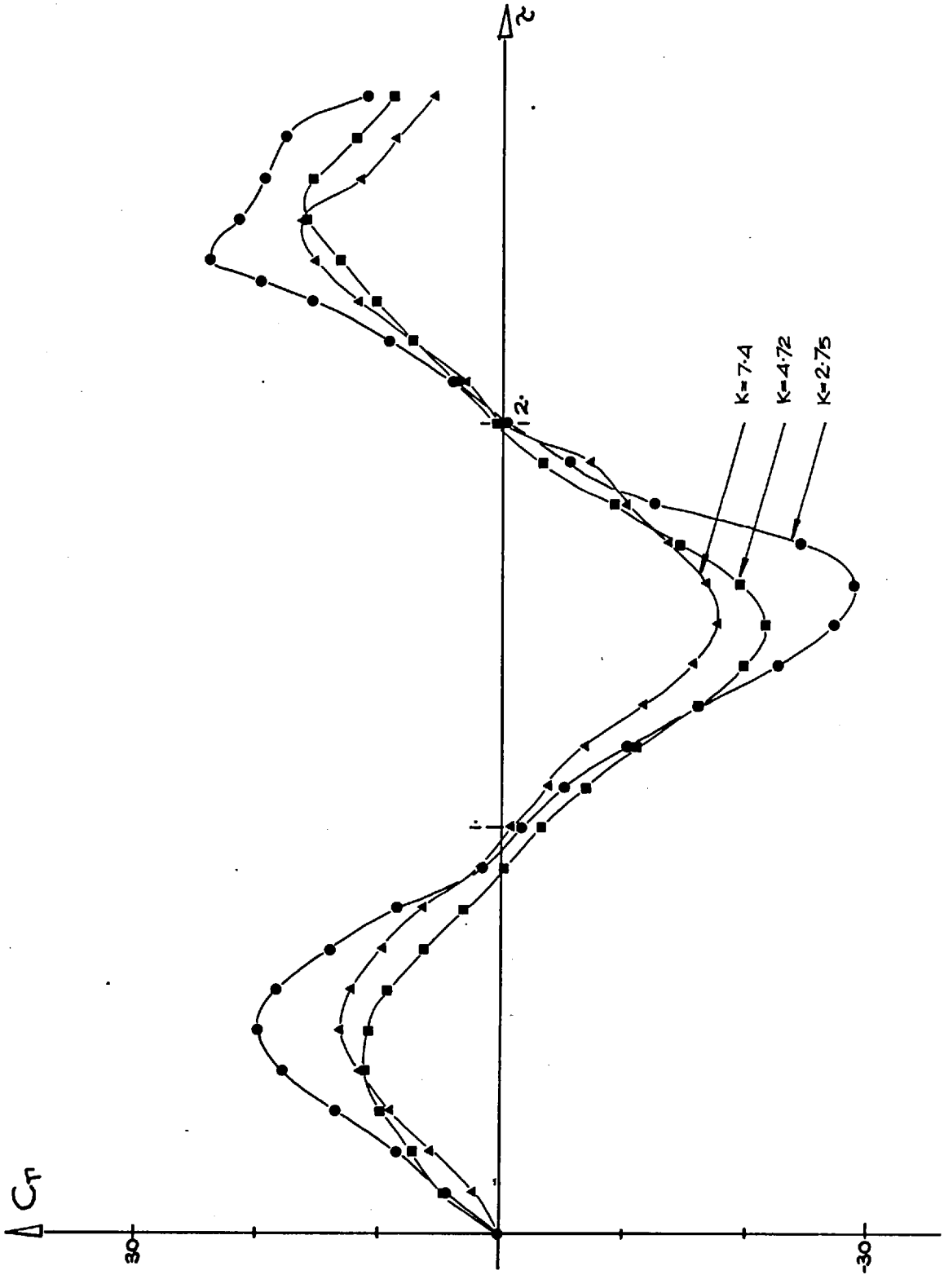

Fig. 5.16

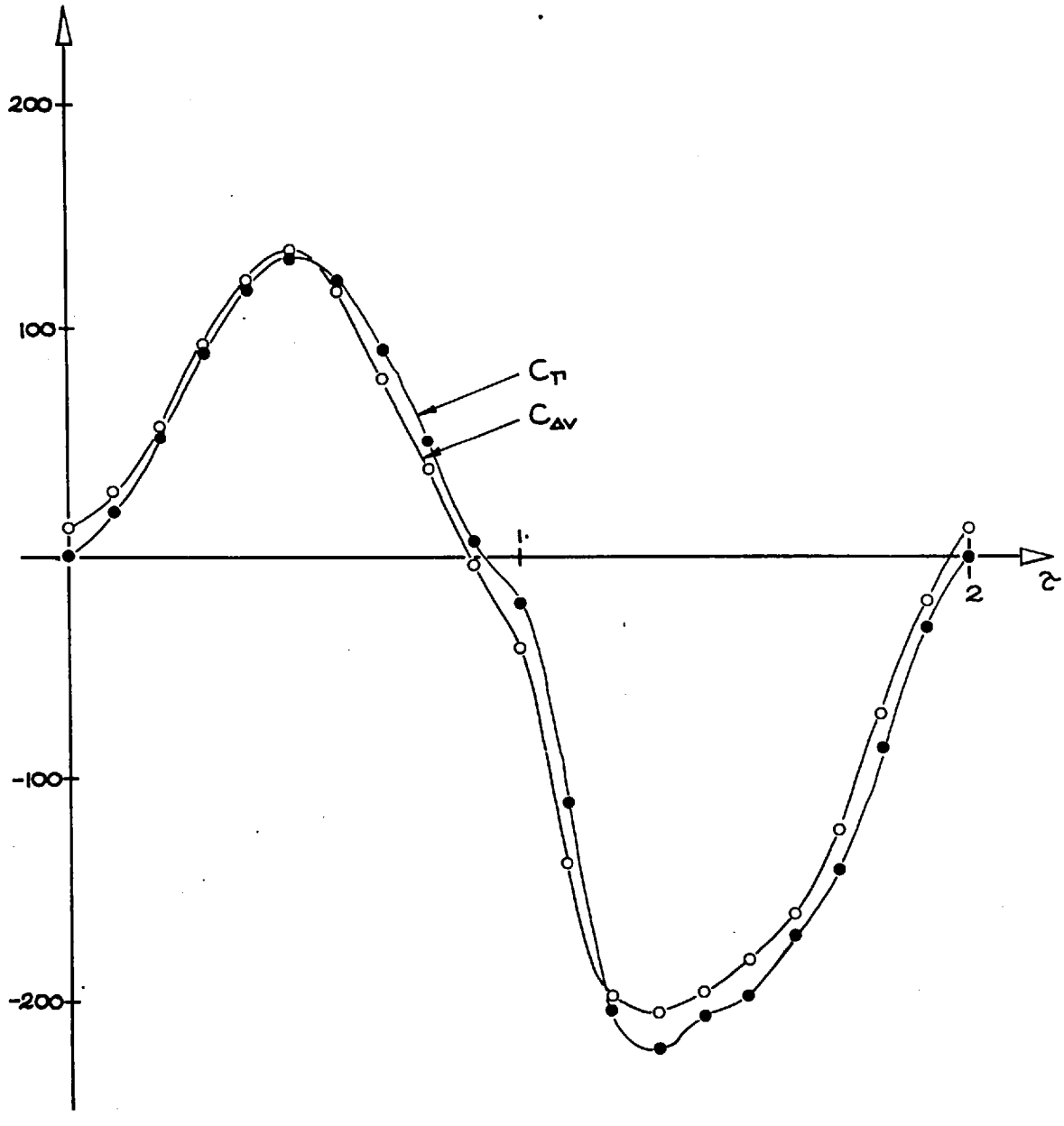

Fig. 5.17

Several studies (Young & Tsai, 1973; Mates et al, 1978; Clark, 1976; Djilali, 1978) have suggested that the instantaneous pressure drop may be expressed in the form of Morison's equation. Equation (5) can be then rewritten as

$$C_{\Delta p}(\tau) = \frac{4\pi}{K} C_M \cos\theta + \left(\frac{c}{1-c}\right)^2 C_D \sin\theta|\sin\theta| \qquad (6)$$

by taking the appropriate Fourier's integral over one cycle. Following the procedure shown in section (4.2), we have

$$C_M = 1 + \frac{K}{2\pi L} \int_0^1 C_{\Delta V}(\tau) \cos 2\pi\tau \, d\tau \qquad (7)$$

and

$$C_D = \frac{3\pi}{4} \left(\frac{1-c}{c}\right)^2 \int_0^1 C_{\Delta V}(\tau) \sin 2\pi\tau \, d\tau \qquad (8)$$

WHERE $(1-c)/c = 1./(R^2/R_o^2 - 1)$

Fig. (5.18) shows the calculated values of C_M and C_D for different constriction ratios c and different K compared with the experimental results for K = 7.4 and α = 22.1. The numerical results shows

$$\frac{2\pi L}{K}(C_M - 1) = K^{\alpha_M} A \qquad (9)$$

and

$$\frac{4c^2}{3\pi(1-c)^2} C_D = K^{\alpha_D} B \qquad (10)$$

where $\alpha_M = 2 \pm .3$, $\alpha_D = 1. \pm .05$ and A and B are constant. The experimental and the calculated C_M show the same qualitative features, even if the calculated values of C_M

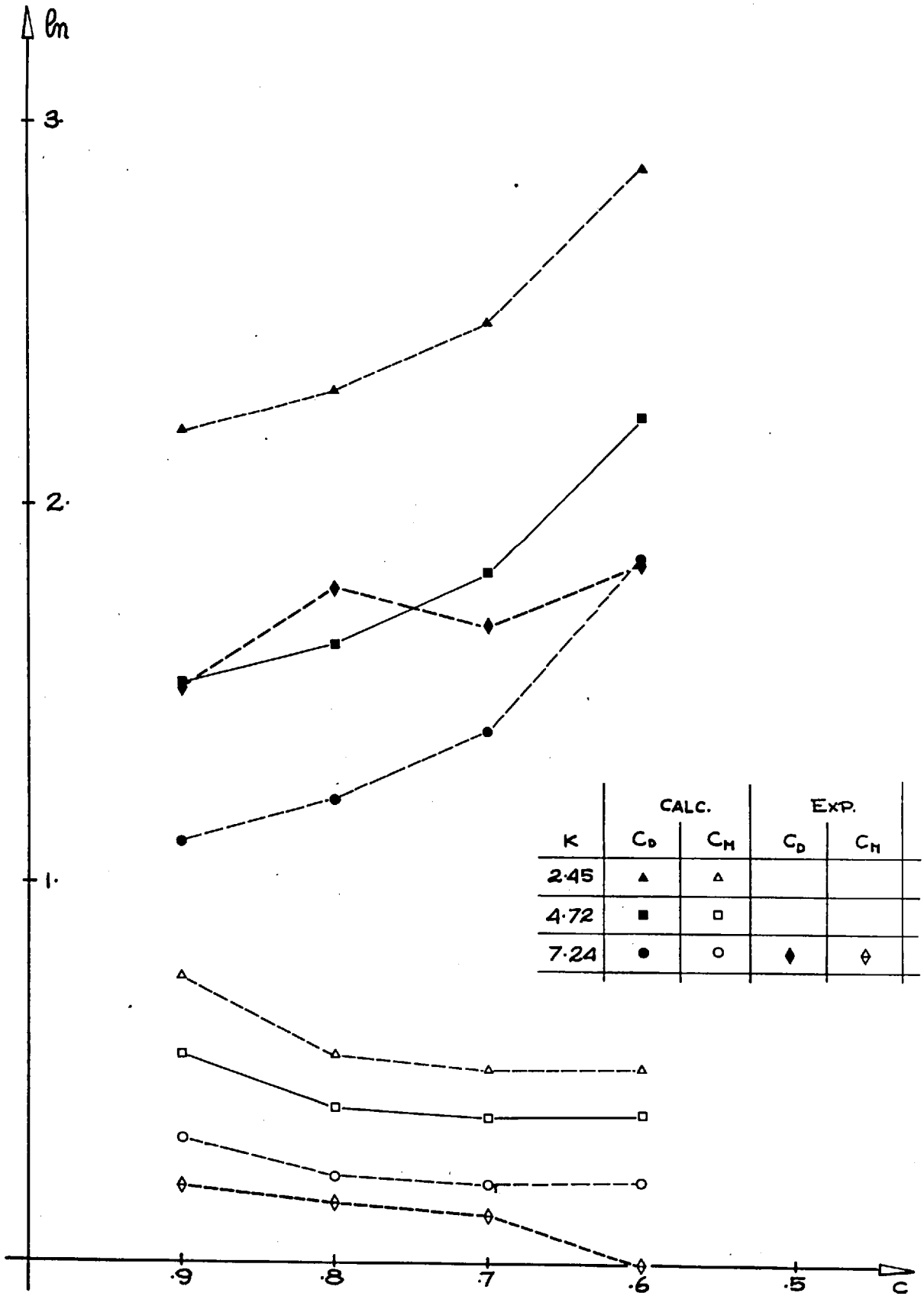

Fig. 5.18

are always higher. However, the calculated C_D exhibits a dependence on c which is absent in the experimental C_D. This may be better represented by substituting $C_d Ro$ for Ro in equation (8), where Cd is an empirical discharge coefficient. Experimentally Cd turns out to be very close to the steady flow value (.6 ÷ .65).

An estimate of the instantaneous pressure drop across "physiological stenoses" is commonly obtained by a quasi-steady approximation of equation (6) (see, for example, the review by Young (1979).

$$C_{\Delta p}^{s}(\tau) = \frac{C_v}{Re} \sin\theta + C_{\Delta p}(\tau) = T_v + T_D + T_M \qquad (11)$$

where the coefficient C_D is not expected to depend upon the geometry and is equal to the steady flow case. Similarly, in the first term of equation (11) which approximates the viscous effects, the coefficient C_v is given by assuming the flow is quasi-steady

$$C_v = .32 \frac{8L_s + 3.3R_o}{2R(1-c)} \qquad (12)$$

In the present case, where $L_s = 0$, $C_v = 1660, \ldots, 207$ for $c = .9, \ldots, .6$. In the experiment, with Re = 1150, the first term of equation (11) ranges from 1.44 to .18 and the ratio between T_v and T_D ranges between .007 and 0.13. Therefore, it is reasonable to assume, as we have done, that the viscous effects are small.

Figure (5.19) shows the calculated $C_{\Delta p}$ in the case of a slightly pulsatile flow for c = .8 with $\gamma = 3.5$ and $K = 3.5$. The non-dimensional time step was $\delta\tau = .025$.

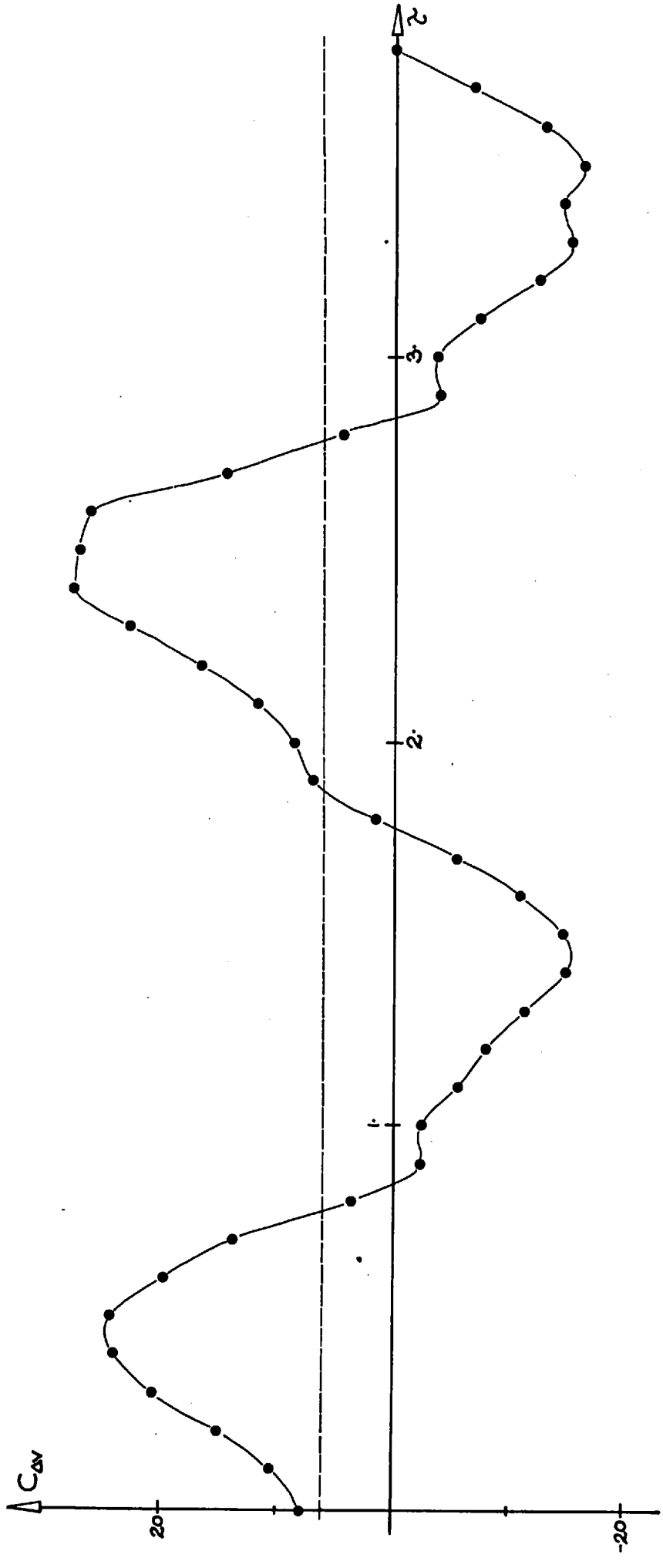

Fig. 5.19

$C_{\Delta V}$ shows clearly an asymmetry in the peak values and the presence of an offset value $\bar{C}_{\Delta V} = 6$. Using the continuity equation across the orifice and using the experimental discharge coefficient which takes into account the presence of the jet, the expected steady pressure drop coefficient is

$$\bar{C}_{\Delta p} = \left[\frac{1}{(1-c)^2 C_d^2} - 1\right](1+\delta)^{-2} \qquad (13)$$

In this case $\bar{C}_{\Delta p} = 3.5$ with $C_d = .6$

5.2 Stepped orifice

Finally, we briefly investigate the influence of the length of the constriction L_s^* on the flow patterns and on the pressure drop The constriction presents two sharp convex corners of internal angle $\delta = \pi/2$ and a cylindrical throat of length $L_s = L_s^*/R^*$. The constriction ratio c was chosen to be .8 and $U_o^* = 0$. The pipe and the constriction were simulated by 80 annular elements distributed as in the case of the flat orifice plate. The attached potential flow near the edge was found to be, as expected, of $O(\eta_o^{-1/3})$ where η_o is the distance from the edge along the edge walls. Two vortices were shed at the two convex corners at every time step forming two shear layers, which eventually appear as a single thick vortex sheet. Figs. (5.20), (5.21), (5.22) and (5.23) show the results of numerical calculations for L_s = .25, .5, 1, 2 with K = 4.75 and $\delta\tau$ = .0125.

The primary feature of the calculations is the formation and the evolution of a thick vortex sheet which rolls up into

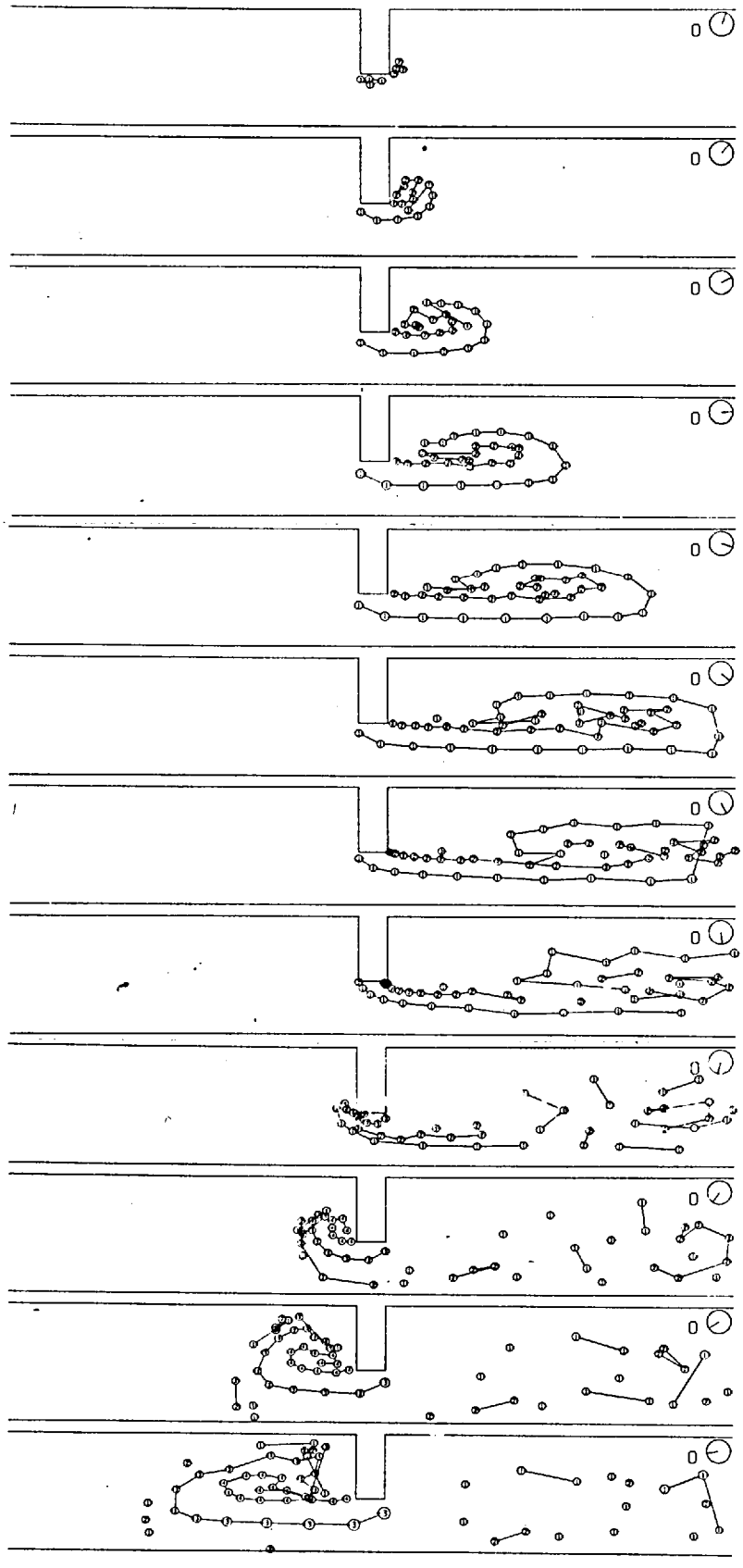

Fig. 5.20 (a)

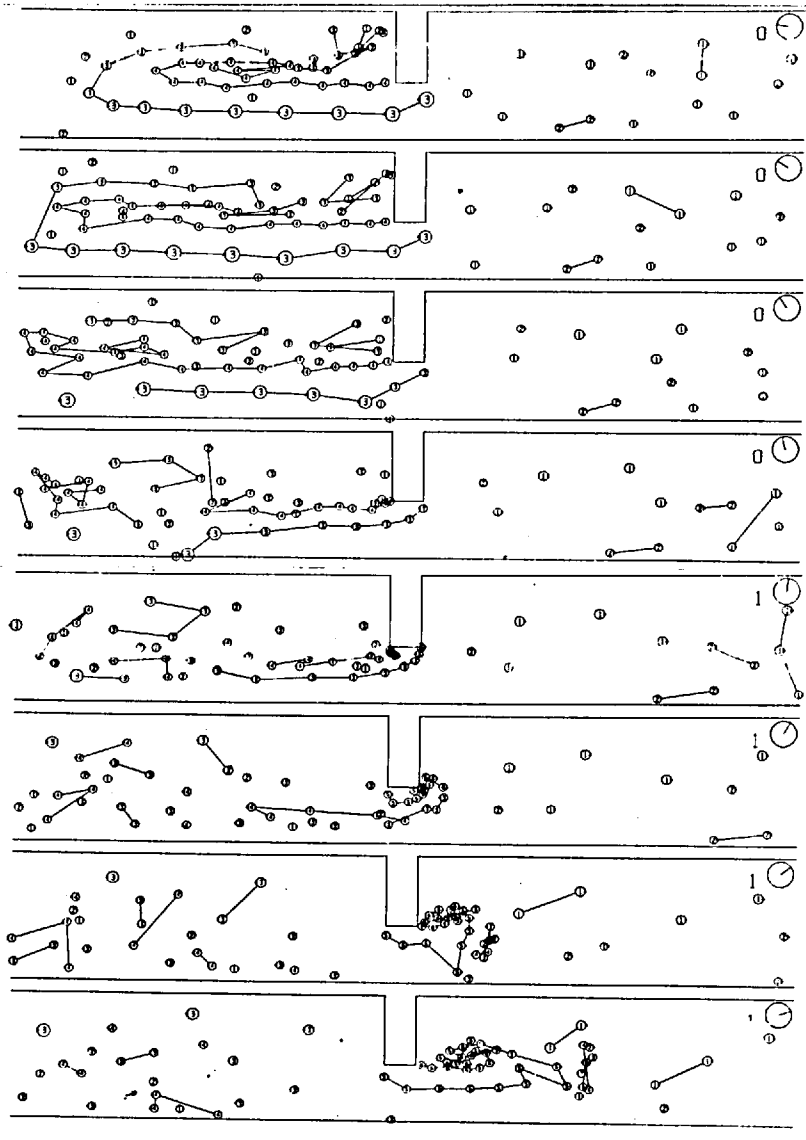

Fig. 5.20 (b)

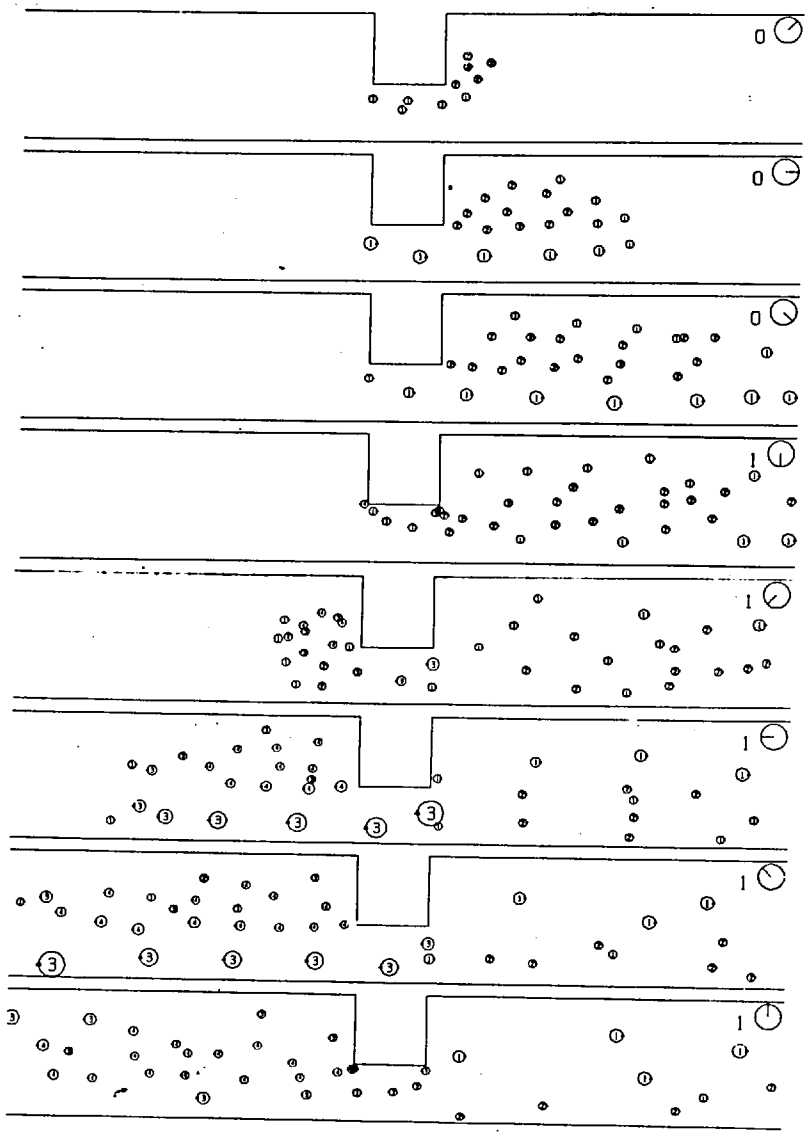

Fig. 5.21

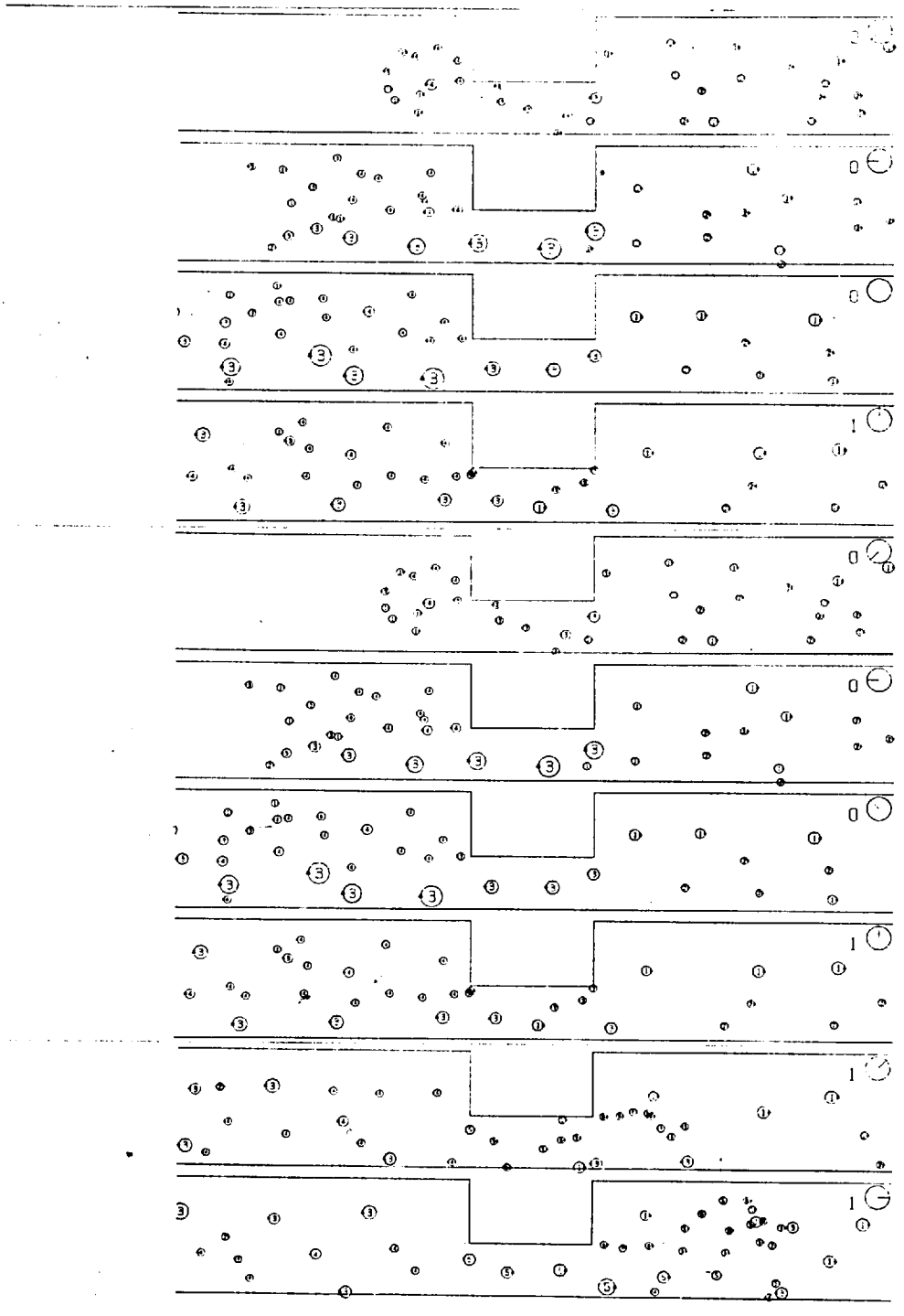

Fig. 5.22

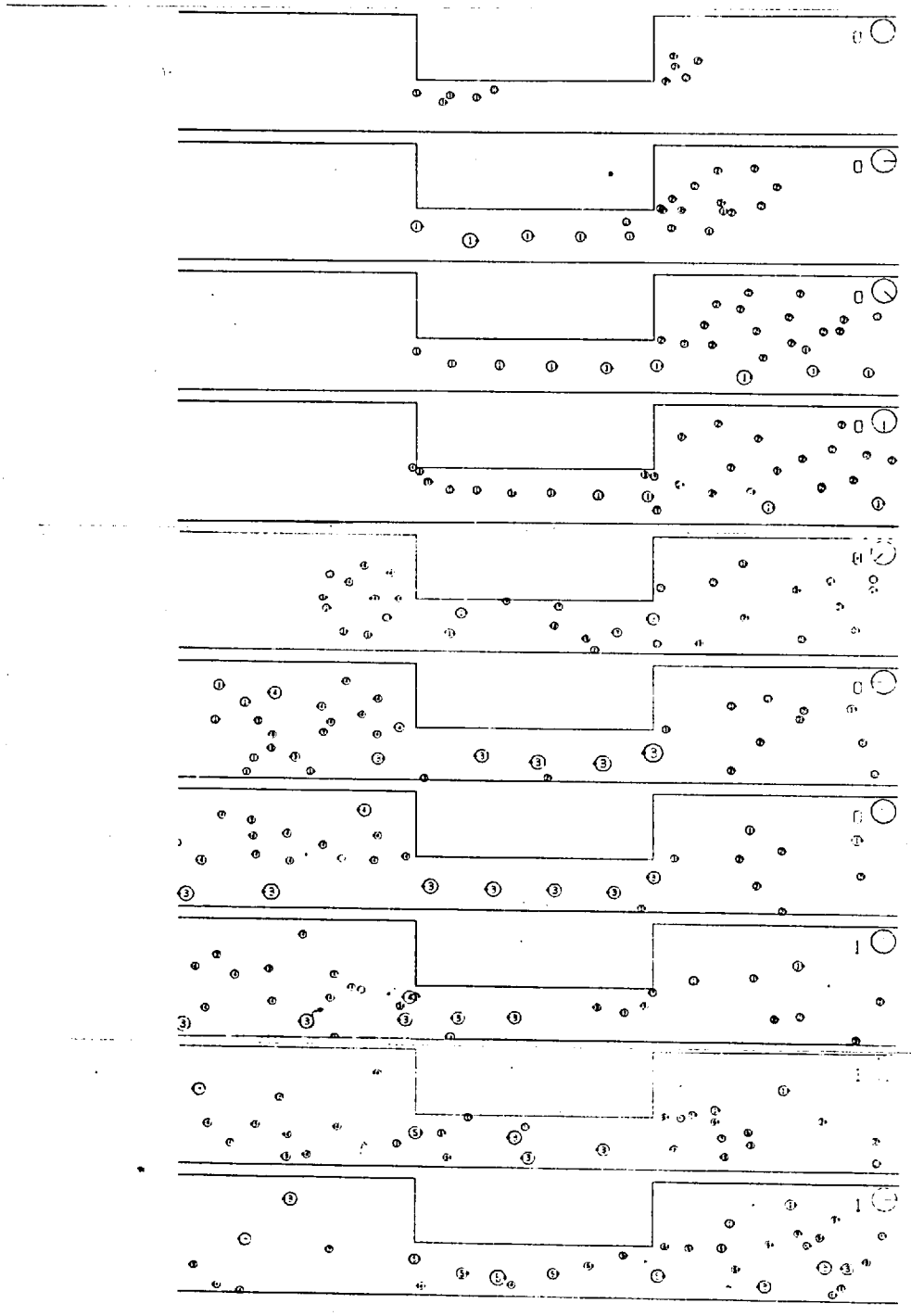

Fig . 5.23

single vortex ring each half cycle. The vortex sheet, generated at the downstream sharp edge, always contributes to the formation of the core of the vortex ring, whereas the other vortex sheet is wound around such a core forming the outer edge of the vortex. Mixing between the two free vortex sheets always seems to happen only when the flow reverses. The thick vortex sheet shows more stable behaviour consistent with Moore's (1978) analysis even if one might doubt, as in the case of Michalke's (1964) calculations, that the development of the pair of free vortex sheets correctly represents the development of a vortex sheet of small thickness. As in the flat plate orifice case, little or no vorticity generated during a half-cycle was observed to be convected back through the throat of the constriction during the subsequent half cycle.

Of particular interest is the reattachment length. This has been extensively studied in the case of steady flow. Back and Roschke (1972) have shown that for a sharp-edged abrupt expansion the reattachment length increases with the jet Reynolds number R_{ej} for $R_{ej} \leq 200$ and it appears to reach a limiting value for high R_{ej} ($R_{ej} > 2000$). Streamlined geometries have shown similar behaviour and it has been observed that the reattachment length depends primarily on the constriction ratio (Deshpand, Giddens & Mabon, 1976). Little or no information is available in the case of unsteady flow.

Fig. (5.24) shows the location of the reattachment point in time for L_s = 0, 1, 2. The separated region grows

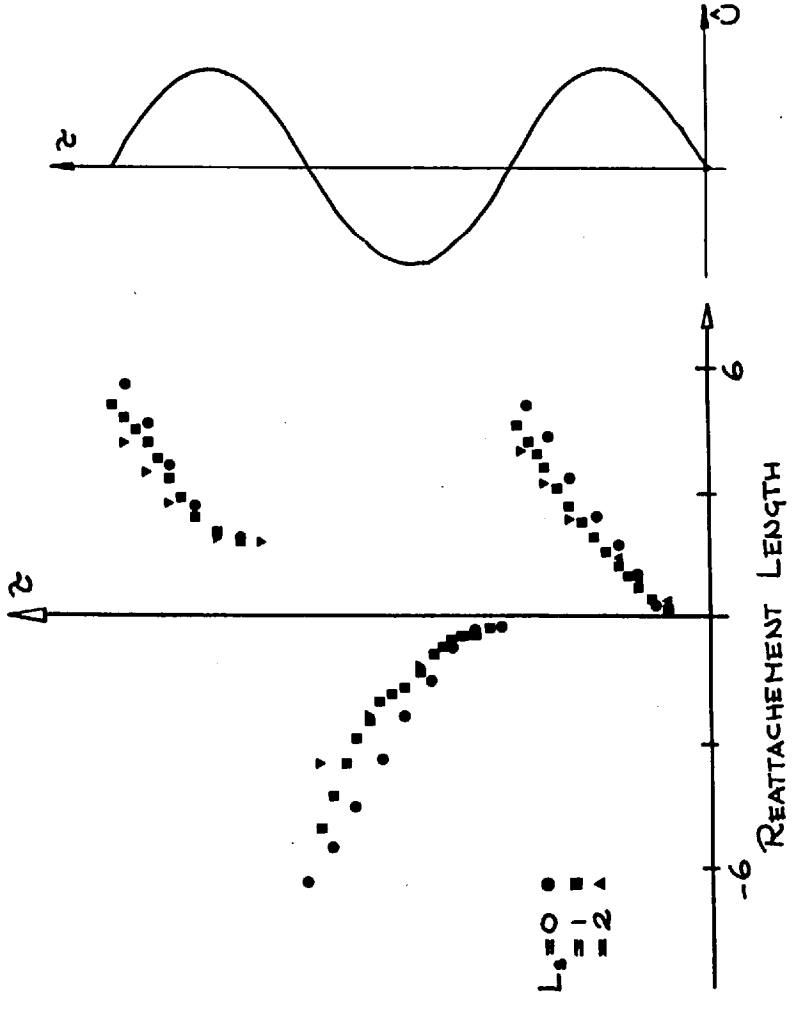

Fig. 5.24

during the systolic phase until the flow reverses and, during the diastolic phase, it develops on the other side of the constriction. The reattachment length is fairly independent of the constriction length and at the ends of the systolic and diastolic phases, it reaches its maximum value ~ 6. Note that for jet Reynolds number equal to the peak value, $Re_j = 1704$, in present case, Back & Roschke (1972) observed a reattachment length between 4 and 5 for the steady case.

The instantaneous pressure drop coefficient between two points s_1 and s_2 is given by equation (3) and again it may be written in the form of equation (5) of the calculated $C_{\Delta v}$ for L_s = 0, .25, .5, 1, 2 are shown in figure (5.25). The values of C_M and C_D calculated by means of the equations (7) and (8) are plotted in fig. (5.26) as functions of the construction length L_s. C_D exhibits an independence of L_S which suggests that the rate of shedding is not strongly affected by the presence of the constriction throat. However, C_M shows a steep linear growth with L_s which is due to the increase of the total apparent mass. The instantaneous dependence of the inertial effects of the attached flow on L_S can be estimated as

$$\Delta C_{\Delta p}(\tau) = \frac{4\pi c}{K(1-c)} L_s \cos 2\pi\tau \qquad (14)$$

Then the effect of separations alone can be represented as the difference between the calculated pressure drop $C_{\Delta p}$ and

$$C^A_{\Delta p}(\tau) = \left[C_{\Delta p}(\tau)\right]_{L_s=0} + \Delta C_{\Delta p}(\tau) \qquad (15)$$

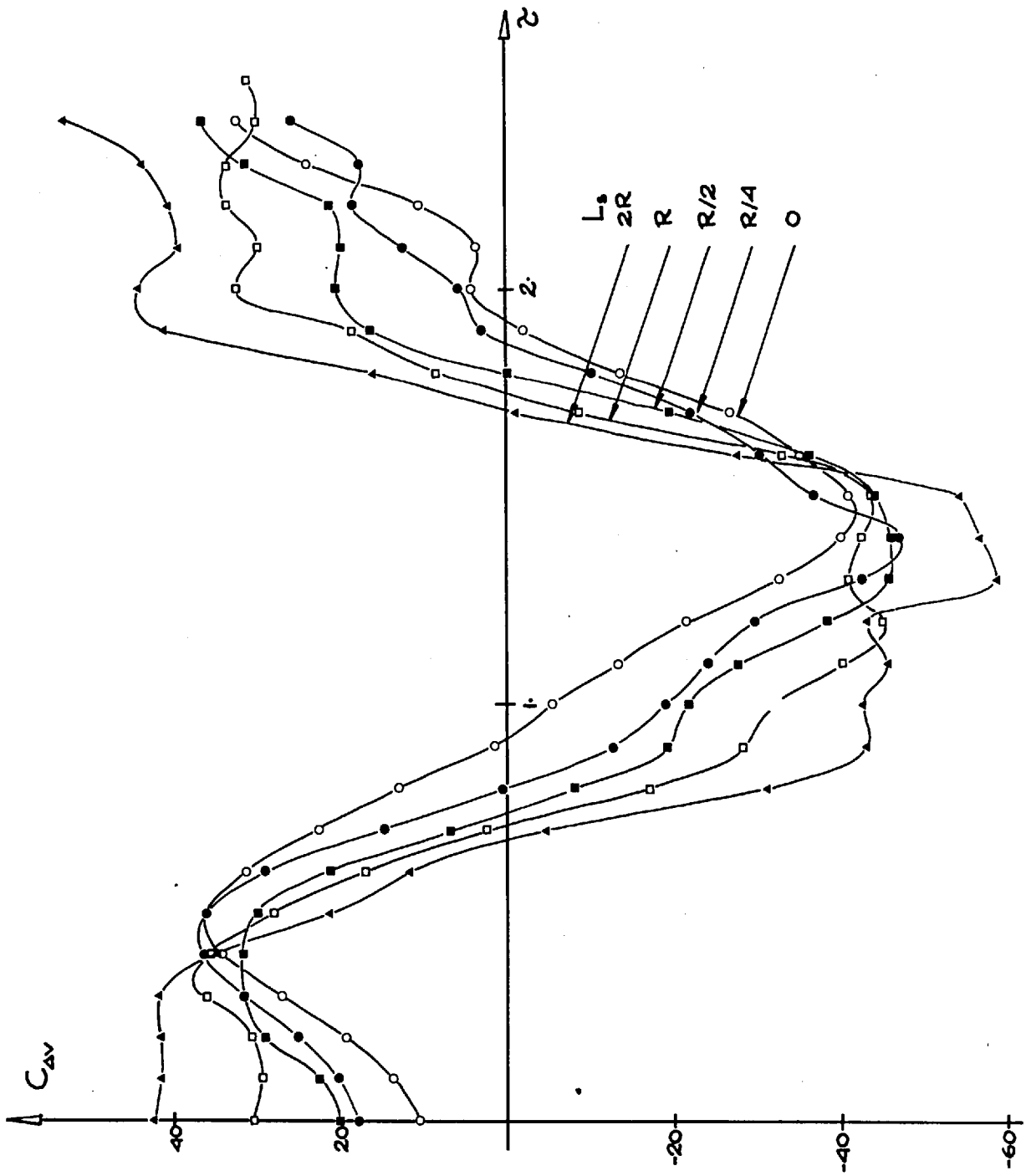

Fig. 5.25

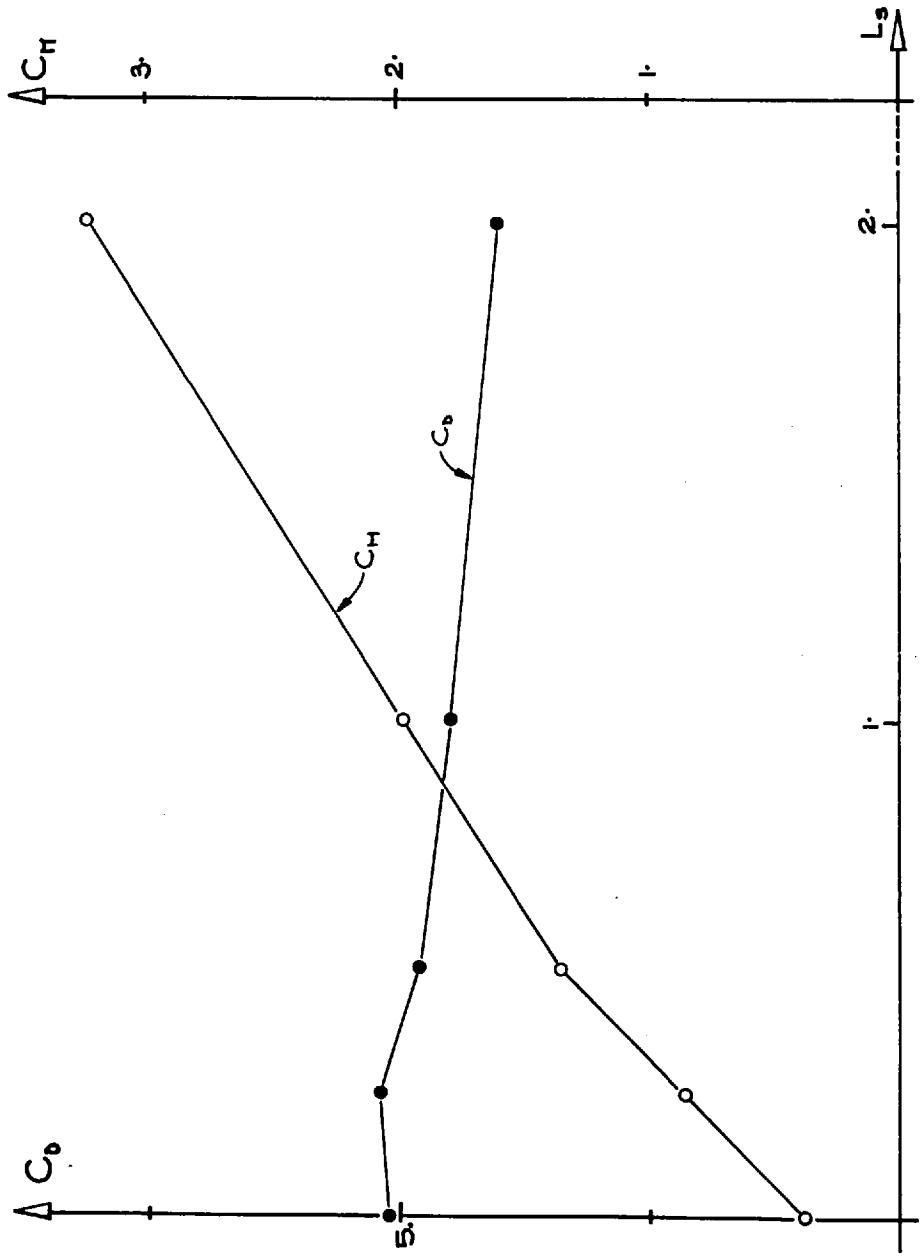

Fig. 5.26

Figure (5.27) shows the difference between the calculated pressure drop $C_{\Delta p}$ and $C^{\wedge}_{\Delta p}$ given by eqn. (15). As L_s increases, the slopes of the two curves converge. This indicates that the contribution of the separation becomes quite constant and the attached flow dominates the inertial component as expected. This is consistent with Mates et al (1978) observations in the asymmetric trapezoidal stenosis that the peak pressure drop increases less steeply as the length of the constriction increases.

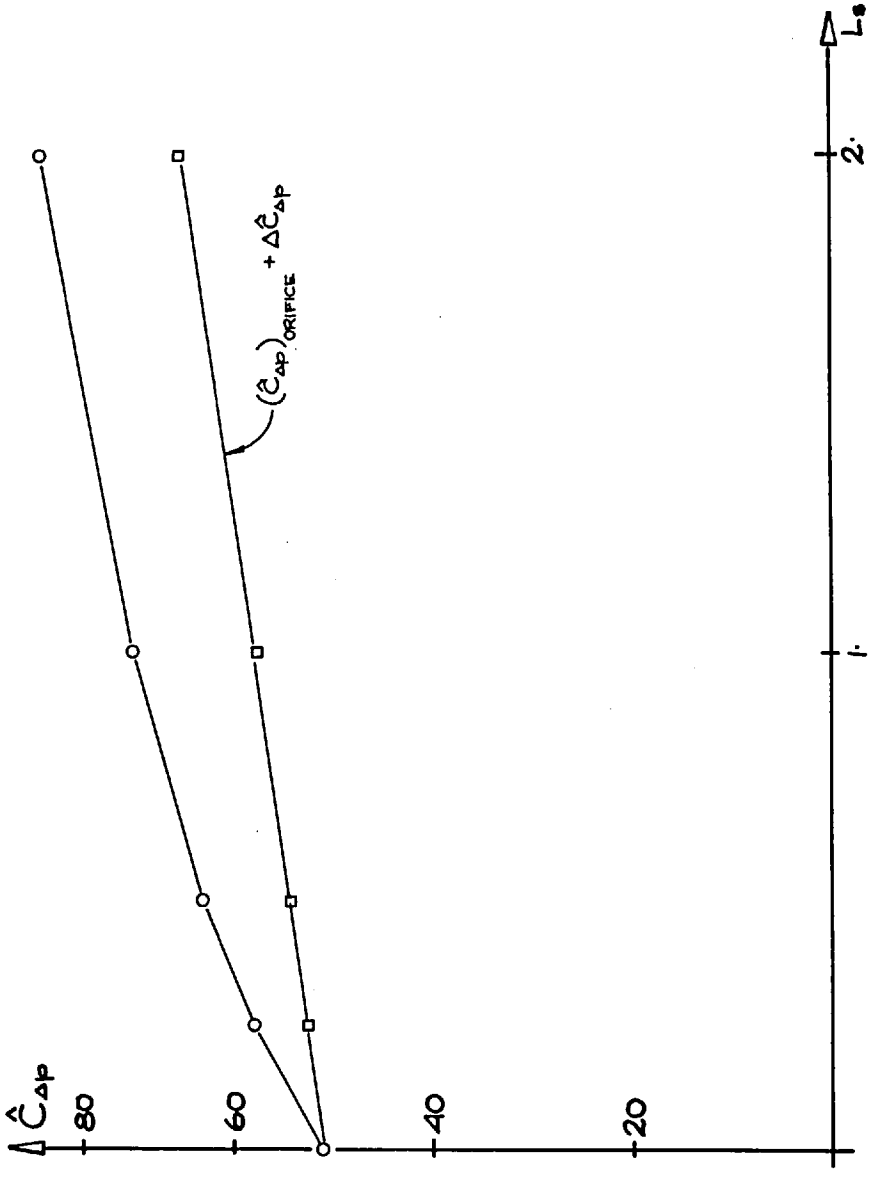
$\hat{C}_{\Delta p}$
80
60
40
20
$(\hat{C}_{\Delta p})_{ORIFICE} + \Delta\hat{C}_{\Delta p}$
L/d
2·
1·

Fig. 5.27

6. CONCLUSION

The "direct summation" method of discrete vorticies extensively used to calculate 2-D flows, has been extended to axisymmetric flows. It is a relatively fast method for calculating unsteady, high Reynolds number, separated flows and predicts the dominant features of the flow accurately.

Calculations of the flow around an impulsively started disc showed a close similarity to the flow around a 2-D plate during the very first stages of the starting vortex evolution. As time increases, the axisymmetric nature of the disc flow becomes important and the vortex sheet rolls up to form a vortex ring. The predicted distribution of pressure on the disc surface and the drag coefficient tend to the experimental values for the steady state, even if the separated bubble behind the disc is forced to be axisymmetric and the wake is unable to develop into 3-D vortex loops which are observed experimentally.

In unbounded oscillatory flow around a disc, the calculations correctly predict the "pairing" and the unidirectional streaming of shed vortex rings which were observed experimentally. The regime conditions are reached in a shorter time (1 ÷ 2 cycles) then in the 2-D calculations and it presents more stable behaviours. It also shows that for small values of the Kuelegan-Carpenter number the calculated inertia and drag coefficient in the Morison's equation for the disc present features very close to those of a single plane infinite edge.

For the bounded unsteady flow through a constricted pipe, the calculations correctly predict the presence and the location of the well defined vortices which are shed during each half cycle and the instantaneous pressure drop coefficient across the constriction. The peak pressure drop coefficient depends on the Kuelegan-Carpenter number and is found to be significantly affected by the constriction ratio only for severe constrictions ($C > .7$). The length of the constriction does not seem to affect the separation and the inertial effects due to the vortex shedding are important only for lengths shorter than one pipe radius after which the peak pressure drop increase is due only to the increase of apparent mass.

We did not attempt to investigate more realistic physiological flows, however, the results presented in this thesis may have relevance to the description of the large scale flow generated by a stenosed vessel. The limitations of the direct summation method do not allow us to relax constraints on the flow such as uniform mainstream velocity the sharp-edged geometry, or the absence of viscosity. Far from the constriction the large scale flow does not persist and the viscosity effects dominate. In this range the vorticity diffusion must be considered. This seems to suggest that a future use of the 'cloud-in-cell' method may lead to a more useful representation of such flows and to a description of their periodic and aperiodic structure on a much smaller length scale than the direct summation method allows.

7.REFERENCES

ABERNATHY, F. H., KRONAUER, R. E. (1962). The Formation of Vortex Streets; J. Fluid Mech., 13, 1-20.

ACTON, E, (1976). The Modelling of Large Eddies in a two-dimensional shear layers; J. Fluid Mech., 76, 561-92.

ACTON, E. (1980). A modelling of large eddies in an axi-symmetric jet; J. Fluid Mech., 98, 1-31.

ANTON, L. (1939). Ausbildung eines wirbels an der kante einer platte; Ing. Arch., 10, 411-27.

ASHURST,W. T. (1977). Numerical-simulation of turbulent mixing layers via vortex dynamics; Sandia Lab. Rep. Sand 77-8612.

ASHURST, W. T. (1978). Calculation of plane sudden expansion flow via vortex dynamics; 2nd Symposium on Turbulent Shear Flows. Imperial College, London.

ASHURST, W. G. (1979). Piston-cylinder fluid motion via vortex dynamics; presented at Euromech 119, 16-18 July, 1978, London.

AZUMA, T., FUKUSHIMA, T. (1976). Flow patterns in stenotic blood vessel models; Biorheology, 13, 337-55.

BACK, L. H., ROSCHKE, E. J. (1972). Shear-layer flow regimes and wave instabilities and reattachment lengths downstream of an abrupt circular channel expansion; ASME J. App. Mech., 39, 677-81.

BAKER, G. R. (1977). Studies of vortex motion; Ph.D. thesis Calif. Institute of Technol., 189.

BAKER, G. R. (1979). The "cloud-in-cell" technique applied to the roll up of vortex sheets; J. Comput. Phys., 31, 76- 95.

BASU, B. C., HANCOCK, G. J. (1977). The unsteady motion of a two-dimensional aerofoil in incompressible inviscid flow. Queen Mary College. QMC-EP1018/R).

BATCHELOR, G. K. (1970). An Introduction to Fluid Dynamics. Cambridge University Press.

BEARMAN, P. W., FACKRELL, J. E. (1975). Calculation of two-dimensional and axisymmetric bluff-body potential flow; J. Fluid Mech., 72, 229-41.

BEARMAN, P. W., GRAHAM, J. M. R., SINGH, S. (1978). Forces on cylinders in harmonically oscillating flow; Symposium on Mechs. of Wave Induced Forces on Cylinders, Bristol.

BEAVERS, G. S., WILSON, T. A. (1970). Vortex growth in jets- J. Fluid Mech., 44, 97-112.

BETZ, A. (1932). Verhalten von wirbelsyestemen; ZAMM, 12, 164-74.

BLENDERMAN, W. (1969). Der spiralwirbel am translatorish bewegung und reaktion; Schiffstechnik, 16, 3-14.

BRADBURY, L. J. S. (1976). Measurements with a pulsed-wire and a hot-wire anemometer in the highly turbulent wake of a normal flat plate; J. Fluid Mech., 77, 473-97.

BROWAND, F. K., WEIDMAN, P. D. (1976). Large scale in the developing mixing layer; J. Fluid Mech., 76, 127-44.

BROWN, C. E., MICHAEL, W. H. (1954). Effect of leading edge separation on the lift of a delta wing; J. Aero. Sci., 21, 690.

CARO, C. G., FITZGERALD, J. M., SCHROTER, R. C. (1971). Atheroma and arterial wall shear stress; Proc. Roy. Soc. (B), 177, 109-59.

CASSANOVA, R. A., GIDDENS, D. P. (1978). Disorder distal to modelled stenoses in steady and pulsatile flow; J. Biomechanics, 11, 441-53.

CHAPLIN, H. R. (1964). A method for numerical calculation of slipstream contraction of a shrouded impulse disc in the static case with application to other axisymmetric potential flow problems; David Taylor Model Basin Report, No. 1857.

CHORIN, A. J. (1973). Numerical study of slightly viscous flow; J. Fluid Mech., 57, 785-96.

CHRISTIANSEN, J. P. (1973). Numerical simulation of hydrodynamics by the method of point vortices. J. Comput. Phys., 13, 363-79.

CHRISTIANSEN, J. P., ZABUSKY, N. J. (1973). Instability, coalescence and fission of finite-area vortex structures. J. Fluid Mech., 61, 219-43.

CLARK, C. (1976). The fluid mechanics of aortic stenosis; J. Biomechanics, 9, 521-28, 567-73.

CLEMENTS, R. R. (1973). An inviscid model of two-dimensional vortex shedding; J. Fluid Mech., 57, 321-36.

CLEMENTS, R. R., MAULL, D. J. (1973). The rolling up of a trailing vortex sheet; Aeronaut. Journal, 77, 46-51.

CLEMENTS, R. R., MAULL, D. J. (1975). The representation of sheets of vorticity by discrete vortices; Prog. Aerospace Sci., 16, 129-46.

CRAGGS, J. W., MANGLER, K. W. (1971). Some remarks on the behaviour of surface source distributions near the edge of a body. Royal Aircraft Test. Tech. Rept. 71085.

CROW, S. C., CHAMPAGNE, F. H. (1971). Orderly structure in jet turbulence; J. Fluid Mech., 48, 547-91.

DALY, B. J. (1977). A numerical study of pulsatile flow through stenosed canine femoral arteries; J. Biomechanics, 9, 465-75.

DAVIES, P. O. A. L., HARDIN, J. C. (1973). Potential flow modelling of unsteady flow; Int. Conf. on Numerical Methods in Fluid Dynamics, Dept of Civil Engng., University of Southampton.

DESHPANDE, M. D., GIDDENS, D. P., MABON, R. F. (1976). Steady laminar flow through modelled vascular stenoses; J. Biomechanics, 9, 165-74.

DIDDEN, N. (1979). On the formation of vortex rings; rolling up and production of circulation; ZAMP, 30, 101-116.

DJILALI,N. (1978). Oscillatory flow through a sharp-edged orifice plate; Imperial College, Dept. of Aeronautics, M.Sc. Thesis.

EVANS, R. A., BLOOR, M. I. G. (1977). The starting mechanism of wave-induced flow through a sharp-edged orifice; J. Fluid Mech., 82, 115-28.

FAGE, A., JOHANSEN, F. C. (1927). The structure of the vortex sheet; Phil. Mag., (7), 5, 417-36.

FAIL, R., LAWFORD, J. A., EYRE, R. C. W. (1957). Low speed experiments on the wake characteristic of flat plates

normal to an air stream; Aero. Res. Counc. R. & M. No. 3120.

FINK, P. T., SOH, W. K. (1974). Calculations of vortex sheets in unsteady flow and applications in ship hydrodynamics; 10th Symp. Naval Hydrydynamics, Cambridge, Mass. 463-89.

FRY, D. L. (1973). Response of the arterial wall to certain physical factors in Atherogenesis. Ciba Foundation Symposium 12, Elsevier, Excerpta Medica, 93-125.

GERRARD, J. H. (1967). Numerical computation of the magnitude and frequency of the lift on a circular cylinder; Phil. Trans. Roy. Soc., A261, 137-62.

GIESING, J. P. (1968). Non linear two-dimensional unsteady potential flow with lift; J. Aircraft, 5, 135-43.

GIESING, J. P. (1969). Vorticity and Kutta condition for unsteady multienergy flows; ASME Trans. J. Appl. Mech., 36, 608-13.

GOLDSTEIN, S. (1965). Modern developments in fluid dynamics. Dover publications, 2, 577-79.

GOLIA, C., EVANS, N. A. (1973). Flow separation through annular constrictions in tubes; Experimental Mechanics, 13, 157-62.

GRAHAM, J. M. R. (1977). Vortex shedding from sharp edges. Imperial College Aero. Rept. 77-06.

GRAHAM, J. M. R. (1980). The forces on sharp-edged cylinders in oscillatory flow at low Keulegan-Carpenter numbers; J. Fluid Mech., 97, 331-46.

GUHLER, M., SELLET, D. W. (1979). The formation of vortex rings and their initial motion; Z. Flugwiss, 3, 109-15.

HESS, J. L., SMITH, A. M. O. (1966). Calculations of potential flow about arbitrary bodies; Prog. in Aero. Sciences, 8, 1-138.

JOHANSEN, F. C. (1929). Flow through pipe orifices at low Reynolds number; Proc. Roh. Soc. A 126,231-45.

KAMEMOTO, K., BEARMAN, P. W. (1978). The importance of time step size and initial vortex position in modelling flows with discrete vortices; Imperial College,Aero Tech. Note 78-108.

KEULEGAN, G. H., CARPENTER, L. H. (1958). Forces on cylinders and plates in an oscillating fluid; J. of Research N.B.S., 60, 423,

KHALIFA, A. M.A., GIDDENS, D. P. (1978). Analysis of disorder in pulsatile flows with application to poststenotic blood velocity measurement in dogs; J. Biomechanics, 11, 129-41.

KIYA, M., ARIE, M. (1977). A contribution to an inviscid vortex shedding model for an inclined flat plate in uniform flow; J. Fluid Mech., 82, 223-40.

KNOTT, G. F., MACKLEY, M. R. (1979). On eddy-motions near plates and ducts, induced by water waves and periodic flows; Proc. Roy. Soc. (to appear).

KRUTZSCH, C. H. (1939). Über eine experimentell beubechtete ersheinung an wirbebungen bei ihrer translatorishen bewegung in wirklichen flüssigkeiten; Ann. Phys., 35, 497-523.

LAMB, H. (1932). Hydrodynamics; 6th ed. Cambridge University Press, 1957.

LAMBROSSY, P. (1952). Oscillations forcees d'un liquide incompressible et visqueux dans un tube rigide et horizontal. Calcul de la force de frottement; Helvetica Physica Acta, 25, 371-86.

LEVY, R. H., HOCKNEY, R. W. (1968). Computer experiments on a low-density crossed-field electron beams. Phys. Fluids, 11, 766.

LIESS, C., DIDDEN, N. (1976). Experimente zum einfluss der anfangsbedingungen auf die instabilitat von ringwirbeln; ZAMM, 56, 206-8.

MATES, R. E., GUPTA, R. L. BELL, A. C., KLOCKE, F. J. (1978) Fluid dynamics of coronary artery stenosis; Circulation Res., 42, 152-62.

MASKEW, B. (1977). Subvortex technique for the close approach to a discretized vortex sheet; J. Aircr. 14, 188-93.

MAULL, D. J., MILLINER, M. G. (1978). Sinusoidal flow past a circulation cylinder. Coastal Engineering, 2, 149.

MAXWORTHY, T. (1977). Some experimental studies of vortex rings; J. Fluid Mech., 81, 465-95.

MICHAEL, W. H. (1955). Flow studies on flat-plate delta wings at supersonic speed; Nat. Adv. Comm. Aero., Washington, Tech. Note, No. 3472.

MICHALKE, A. (1964). Zur instabilität und nichtlinearen entwicklung einer gestorten scherschicht; Ing. Arch., 33, 264-76.

MILINAZZO, F., SAFFMAN, P. G. (1977). The calculation of large Reynolds number two-dimensional flow using discrete vortices with random walk; J. Comput. Phys., 23, 380-92.

MOFFATT, H. K., MOORE, D. W. (1978). The response of Hill's spherical vortex to a small axisymmetric disturbance. J. Fluid Mech., 87, 749-60.

MOORE, C. J. (1977). The role of shear layer instability waves in jet exhaust noise; J. Fluid Mech., 80, 321-67.

MOORE, D. W. (1971). The discrete vortex approximation of a vortex sheet; Calif. Inst. Technol. Rep. AFOSR-1084-69.

MOORE, D. W. (1974). A numerical study of the roll-up of a finite vortex sheet; J. Fluid Mech., 63, 225-35.

MOORE, D. W. (1976). The stability of an evolving two dimensional vortex sheet; Mathematika, 23, 35-44.

MOORE, D. W. (1978). The equation of motion of a vortex layer of small thickness; Stud. App. Math., 58, 119-40.

MOORE, D. W., GRIFFITH-JONES, R. (1974). The stability of an expanding circular vortex sheet; Mathematika, 21, 128-33.

MOORE, D. W., SAFFMAN, P. G. (1971). Structure of a line vortex in an imposed strain; Aircraft Wake Turbulence, ed. Olsen, J. H., Goldburg, A., Rogers, M., 339-54.

MOORE, D. W., SAFFMAN, P. G. (1973). Axial flow in laminar trailing vortices; Proc. Roy. Soc., A333, 491-508.

MOORE, D. W., SAFFMAN, P. G. (1975). The density of organised vortices in a turbulent mixing layer; J. Fluid Mech., 69, 465-73.

ONSAGER, L. (1949). Statistical hydrodynamics; Nuovo Cimento, 6, 279-87.

PARKINSON, G. V., JANDALI, T. (1970). A wake source model for bluff body potential flow; J. Fluid Mech., 40, 577-94.

PELLEGRIN, M. T. (1976). Pulsating flow of an incompressible fluid through a sharp edged orifice meter; Ph.D. thesis West Virginia University.

PULLIN, D. I. (1978). The large scale structure of unsteady self-similar rolled-up vortex sheets; J. Fluid Mech., 88, 401.

PULLIN, D. I. (1979). Vortex ring formation at tube and orifice openings; Phys. Fluids., 22, 401-3.

PULLIN, D. I., PERRY, A. E. (1980). Some flow visualization experiments on the starting vortex; J. Fluid Mech., 97, 239-55.

ROSENHEAD, L. (1931). The formation of vortices from a surface of discontinuity; Proc. Roy. Soc., A134, 170-92.

ROSHKO, A. (1976). Structure of turbulent shear flows: a new look; AIAA Journal, 14, 1349-57.

ROTT, N. (1956). Diffraction of a weak shock with vortex generation; J. Fluid Mech., 1, 111-28.

SACKS, A. H., TICKNER, B. G., MACDONALD, I. B. (1971). Criteria for the onset of vascular murmurs; Circulation Res., 29, 249-56.

SAFFMAN, P. G. (1974). The structure and decay of trailing vortices- Arch. Mech., 26, 423-39.

SAFFMAN, P. G. (1978). The number of waves on unstable vortex rings; J. Fluid Mech., 84, 625-39.

SAFFMAN, P. G., BAKER, G. R. (1979). Vortex interactions; Am. Rev. Fluid Mech., 11, 95-122.

SARPKAYA, T. (1975). An inviscid model of two-dimensional vortex shedding for transient and asymptotically steady separated flow over an inclined flat plate; J. Fluid Mech., 68, 109-28.

SARPKAYA, T. (1975). Comment on "Theoretical study of lift-generated vortex wakes designed to avoid roll-up"; AIAA Journal, 13, 1680-81.

SARPKAYA, T. and SCHOAFF, R. L. (1979). Inviscid model of two-dimensional vortex shedding by a circular cylinder; AIAA Journal, 17, 1193-1200.

SELLET, R. S., WIDMAYER, D. W. (1974). An experimental investigation of laminar and turbulent vortex rings in air; Z. Flugwiss, 22, 207-15.

SHEFFIELD, J. S. (1977). Trajectories of an ideal vortex pair near an orifice; Phys. Fluids, 20, 543-5.

SINGH, S. (1979). Forces on bodies in an oscillatory flow; University of London, Ph.D. Thesis.

SMITH, J. H. B. (1966). Theoretical work on the formation of vortex sheets; Prog. in Aero Sciences, 7, 35-52.

SMITH, J. H. B. (1968). Improved calculations of leading-edge separation from slender thin, delta wings. Proc. Roy. Soc., A306, 67-90.

STEIN, P. D., SABBAH, H. N. (1974). Measured turbulence and its effect on thrombus formation; Circ. Res., 35, 608-14.

SYNGE, J. L.., LIN, C. C. (1943). On a statistical model of isotropic turbulence; Trans. Roy. Soc. Canada, 37, 45-63.

THOMPSON, D. H. (1975). A water tunnel study of vortex breakdown over wings with highly swept edges; Australian Defence Scientific Service Aeronaut. Res. Lab. Aerodyn. Note 356.

TOJO, MIYANAMI, K., MINAMI, I., YANO, T. (1979). Power dissipation in a vibrating disc column; Chem. Eng. Journal, 17, 211--8.

TOMM, D. (1977). Model investigation of sound generation in vessel stenosis; INSERM;Euromech 92, Cardiovascular and pulmonary dynamics, 71, 179-92.

TOWNSEND, A. A. (1951). On the fine scale structure of turbulence; Proc. Roy. Soc., A208, 534-56.

WEDERMAYER, E. (1961). Ausbildung eines wirbelpoores an den kouten einer platte; Ingenieur-Archiv., 30, 187-200.

WESTWATER, F. L. (1935). Rolling up of the surface of discontinuity behind an aerofoil of finite span; Aero Res. Comm. Rep. Memo. No. 1692.

WOMERSLEY, J. R. (1955). Method for the calculation of velocity, rate of flow and viscous drag in arteries when the pressure gradient is known; J. Physiology, 127, 553-563.

YONGCHAREON,W. (1977). Development of turbulence in pulsatile, non iniform flow; Ph.D. thesis, IOWA State University.

YOUNG, D. F., TSAI, F. Y. (1973). Flow characteristics in models of arterial stenoses; J. Biomechanics, 6, 395-410, 547-59.

YOUNG, D. F. (1979). Fluid mechanics of arterial stenoses; J. Biomechanic. Eng. 101, 157-175.

APPENDIX

In order to calculate the integrals in equation (2.3.29), we define (see fig. 2.2)

$$r_1^2=(\sigma-\sigma')^2+(x-x')^2 \tag{1}$$

$$r_2^2=(\sigma+\sigma')^2+(x-x')^2 \tag{2}$$

$$a^2=(r_1^2+r_2^2)/2=(x-x')^2+\sigma^2+\sigma'^2 \tag{3}$$

$$b^2=(r_1^2+r_2^2)/2=2\sigma\sigma' \tag{4}$$

so

$$s^2=(x-x')^2+\sigma^2+\sigma'^2-2\sigma\sigma'\cos\theta=r_2^2\left[1-(r_2^2-r_1^2)/r_2^2\cos^2\frac{\theta}{2}\right] \tag{5}$$

$$m=(r_2^2-r_1^2)/r_2^2=4\sigma\sigma'\left[(\sigma+\sigma')^2+(x-x')^2\right]= \tag{6}$$

hence

$$s^2=r_2^2\left[1-m\cos^2\theta/2\right] \tag{7}$$

Using equation (7) in integral (i) we have

$$\int_0^{\pi}\frac{\cos\theta\,d\theta}{s}=\int_0^{\pi/2}\frac{\cos\theta\,d\theta}{\left[1-m\cos^2\theta/2\right]^{1/2}}=$$

$$=2\int_0^{\pi/2}\frac{(2\sin^2\alpha-1)\,d\alpha}{\left[1-m\sin^2\alpha\right]^{1/2}}$$

$$=\frac{4}{m}\int_0^{\pi/2}\frac{(m\sin^2\alpha-m/2)d\alpha}{\left[1-m\sin^2\alpha\right]^{1/2}}$$

$$=\frac{4}{m}\left\{\int_0^{\pi/2}\frac{(1-m/2)d\alpha}{\left[1-m\sin^2\alpha\right]^{1/2}}-\int_0^{\pi/2}(1-m\sin^2\alpha)^{1/2}d\alpha\right\} \tag{8}$$

remembering that the complete elliptic integrals of the first and second kind are

$$K(m)=\int_0^{\pi/2}\frac{d\alpha}{\left[1-m\sin^2\alpha\right]^{1/2}} \tag{9}$$

$$E(m)=\int_0^{\pi/2}(1-m\sin^2\alpha)^{1/2}d\alpha \tag{10}$$

and substituting these relations into equation (8) we obtain

$$\int_0^{\pi} \frac{\cos\theta\, d\theta}{s} = \frac{4}{m}\left[(1 - m/2)K(m) - E(m)\right] \qquad (11)$$

Similarly we transform integral (ii)

$$\int_0^{\pi/2} \frac{(6 - 6'\cos\theta)\cos\theta\, d\theta}{s^3} = \int_0^{\pi} \frac{(6\cos\theta - 6'\cos^2\theta)\, d\theta}{\left[1 - m\cos^2\theta/2\right]^{3/2}} =$$

$$= 2\left\{ \int_0^{\pi/2} \frac{(26\sin^2\alpha - 6 - 46'\sin^4\alpha + 46'\sin^2\alpha - 6')\, d\alpha}{\left[1 - m\cos^2\theta/2\right]^{3/2}} \right\} =$$

$$= -2\left\{ \int_0^{\pi/2} \frac{\left[46'(1 - m\sin^2\alpha)^2/m^2 + (6 + 6' - 46'/m^2)(1 - m\sin^2\alpha)\right] d\alpha}{\left[1 - m\sin^2\alpha\right]^{3/2}} + \right.$$

$$\left. + \int_0^{\pi/2} \frac{\left[m(6 + 6') - 26 - 46' + 46'/m^2\right]\sin^2\alpha\, d\alpha}{\left[1 - m\sin^2\alpha\right]^{3/2}} \right\} =$$

$$= -2\left\{ \frac{46'}{m^2} \int_0^{\pi/2} (1 - m\sin^2\alpha)^{1/2} d\alpha + (6 + 6' - 46'/m^2) \int_0^{\pi/2} \frac{d\alpha}{(1 - m\sin^2\alpha)^{1/2}} + \right.$$

$$\left. + \left[m(6 + 6') - 26 - 46' + 46'/m^2\right] \int_0^{\pi/2} \frac{\sin^2\alpha\, d\alpha}{\left[1 - m\sin^2\alpha\right]^{3/2}} \right\} =$$

$$= -2\left\{ \frac{46'}{m^2} E(m) + (6 + 6' - 46'/m^2)K(m) + \right.$$

$$\left. + \frac{1}{m}\left(m(6 + 6') - 26 - 46' + 46'/m^2\right)\left[(1 - m)^{-1}E(m) - K(m)\right] \right\} \qquad (12)$$

and integral (iii)

$$\int_0^{\pi/2} \frac{\cos\theta\, d\theta}{s^{3/2}} = \int_0^{\pi} \frac{\cos\theta\, d\theta}{(1-m\cos\theta/2)^{3/2}} =$$

$$= 2\left\{\int_0^{\pi/2} \frac{(2\sin^2\alpha - 1)\, d\alpha}{(1-m\sin^2\alpha)^{3/2}}\right\} =$$

$$= -2\left\{\int_0^{\pi/2} \frac{[(1-m\sin^2\alpha) + (m-2)\sin^2\alpha]\, d\alpha}{(1-m\sin^2\alpha)^{3/2}}\right\} =$$

$$= -2\left\{\int_0^{\pi/2} \frac{d\alpha}{(1-m\sin^2\alpha)^{1/2}} + (m-2)\int_0^{\pi/2} \frac{\sin^2\alpha\, d\alpha}{(1-m\sin^2\alpha)^{3/2}}\right\} =$$

$$= -2\left\{\mathbb{K}(m) + \frac{m-2}{m}\left[\int_0^{\pi/2} \frac{1-(1-m\sin^2\alpha)\, d\alpha}{(1-m\sin^2\alpha)^{3/2}}\right]\right\} =$$

$$= -2\left\{\mathbb{K}(m) + \frac{m-2}{m}\left[\frac{1}{1-m}\mathbb{E}(m) - \mathbb{K}(m)\right]\right\} \qquad (13)$$

The three integrals in terms of geometrical variables are:

$$\int_0^{\pi} \frac{\cos\theta\, d\theta}{s} = \frac{[(\sigma+\sigma')^2 + (x-x')^2]^{1/2}}{\sigma\sigma'}\left[\frac{\sigma^2+\sigma'^2+(x-x')^2}{(\sigma+\sigma')^2+(x-x')^2}\mathbb{K}(m) - \mathbb{E}(m)\right] \qquad (14)$$

$$\int_0^{\pi} \frac{(\sigma-\sigma'\cos\theta)\cos\theta\, d\theta}{s^3} = \frac{-1}{\sigma\sigma'[(\sigma+\sigma')^2+(x-x')^2]^{1/2}}\left\{-\left[(x-x')^2+\sigma'^2\right]\mathbb{K}(m) + \right.$$

$$\left. + \frac{[(x-x')^2+\sigma'^2] + \sigma^2[(x-x')^2 - \sigma'^2]}{(\sigma-\sigma')^2 + (x-x')^2}\mathbb{E}(m)\right\} \qquad (15)$$

$$\int_0^{\pi} \frac{\cos\theta\, d\theta}{s^3} = \frac{-1}{\sigma\sigma'[(\sigma+\sigma')^2+(x-x')^2]^{1/2}}\left[\mathbb{K}(m) - \frac{\sigma^2+\sigma'^2+(x-x')^2}{(\sigma+\sigma')^2+(x-x')^2}\mathbb{E}(m)\right] \qquad (16)$$